

Modeling and simulation of coupled electromagnetic field problems with application to model identification and metal forming

Von der Fakultät Maschinenbau
der Universität Dortmund
zur Erlangung des Grades eines
Doktor-Ingenieurs
(Dr.-Ing.)
genehmigte Dissertation

von

Jaan Alexander Unger

Dortmund 2007

Contents

Summary	iii
1 Algorithmic formulation and numerical implementation of coupled electromagnetic-inelastic continuum models for electromagnetic metal forming	1
1.1 Introduction	1
1.2 Summary of basic model relations	3
1.3 Initial boundary value problem for EMF	8
1.4 Algorithmic formulation of the coupled model	12
1.5 Data transfer and numerical convergence behavior	18
1.6 Fully coupled simulation	22
1.7 Discussion	24
2 On the effect of current pulses on the material behavior during electromagnetic metal forming	27
2.1 Introduction	27
2.2 Thermoelastic, viscoplastic model including Joule heating	29
2.3 Application to metal bars subject to pulsed currents and simple tension	32
2.4 Conclusions	34
3 Inverse error propagation and model identification for coupled dynamic problems with application to electromagnetic metal forming	35
3.1 Introduction	35
3.2 Coupled model and algorithmic formulation	36
3.3 Model identification procedure	43
3.4 Parameter identification, correlation and sensitivity	46
3.5 Identification using synthetic data	49
3.6 Identification using experimental data	52
3.7 Conclusions	56
4 Strategies for 3D simulation of electromagnetic forming processes	57
4.1 Introduction	57
4.2 Synopsis of model formulation and description of forming setup	58
4.3 Study of convergence of the electromagnetic model at fixed sheet metal	61

4.4	Mesh adaption and body force data transfer for solid shell elements	70
4.5	Study of convergence of the mechanical model at fixed electromagnetic loads .	74
4.6	Termination criterion for the computation of the electromagnetic part	79
4.7	Discussion of all model simplifications	82
4.8	Discussion of results for a fully coupled simulation	84
4.9	Conclusions	92
A	Technical realization of automatic pre- and postprocessing of parametric 3D models for electromagnetic forming	95
A.1	Introduction	95
A.2	Python based modeling modules and dataflow	96
A.3	Development of automated parametric EMF models with ABAQUS	101
B	Two test examples to verify the implementation of the 2D and 3D electromagnetic models	111
B.1	Magnetic flux density distribution for a cylindrical rod with constant current flux density	111
B.2	Transient current flux density in a cylindrical rod	112
	References	120
	Acknowledgements	121
	Curriculum Vitae	123

Summary

Electromagnetic sheet metal forming (EMF) is an example of a high-speed forming process driven by the dynamics of a coupled electromagnetic-mechanical system. Although electromagnetic forming is a technology known for a few decades, currently renewed interest is taken in its industrial application. Along with this interest the demand for simulation tools is increasing. However, up to now modeling approaches found for this process in the literature lack a comprehensive approach suitable to simulate complex forming operations.

This motivates the algorithmic formulation and implementation of a coupled electromagnetic-inelastic continuum field model for 2D problems discussed in the first part of the work at hand. Here, on the mechanical side, the coupling due to the Lorentz force is acting as an additional body force in the material. On the other hand, the spatio-temporal development of the magnetic field is very sensitive to changes of the shape of the workpiece, resulting in additional coupling. The algorithmic formulation and numerical implementation of this coupled model is based on a mixed-element discretization of the deformation and electromagnetic fields combined with an implicit, staggered numerical solution scheme on two meshes. In particular, the mechanical degrees of freedom are solved on a Lagrangian mesh and the electromagnetic ones on an Eulerian one. The issues of the convergence behavior of the staggered algorithm and the influence of data transfer between the meshes on the solution are discussed in detail. Finally, the numerical implementation of the model is applied to the modeling and simulation of electromagnetic tube and sheet forming.

In the second part of the work the relevance of a possible interaction between electron- and dislocation movement commonly referred to as the electroplastic effect is investigated. In experiments designed to investigate this effect a reduction of the yield stress of up to 60 % is observed under the influence of electric current pulses. In these investigations the timescales, electric current densities, length scales and materials of interest are those relevant to industrial EMF processes. By means of careful modeling of all relevant conventional effects it could be shown that the observed stress reduction is mainly due to thermoelastic effects and it is concluded here that such an effect is of second-order and may safely be neglected in the modeling and simulation of industrial EMF.

The purpose of the third part of the work is the development and application of strategies to identify material model parameters for metals at high strain-rates relevant to EMF forming processes. In particular in the context of the corresponding inverse problem, the goal here is to identify such parameters using data obtained from electromagnetic forming experiments. On the basis of the aforementioned staggered solution scheme, the parameter determination is carried out together with a sensitivity analysis and an error estimation. Here, the optimization problem of the identification of the viscoplastic material parameters can be simplified. As it turns out, the Lorentz forces are relatively insensitive to the material parameters. It is just this situation that allows for an identification procedure at incrementally fixed electromagnetic loads. After

validation of the proposed methodology using synthetic data sets, the material parameters are identified by means of experimental results from tube forming operations.

The last part is motivated by the increasing demand for the modeling of 3D forming operations. This is indispensable for an effective process design of real industrial applications. On the basis of previous modeling concepts in the work at hand, further approaches particularly suitable to reduce the enormous computational cost inherent to 3D simulations are developed and investigated. These consist of a carefully chosen discretization, a data transfer method for both, the electromagnetic loads and the mechanical deformation to utilize an efficient solid shell formulation and a termination criterion for the electromagnetic part of the model. As a result the simulation time is reduced by about one order of magnitude. Finally a 3D forming setup is modeled and detailed insights with respect to the development of eddy currents, magnetic field and deformation of the sheet metal are provided.

Zusammenfassung

Die elektromagnetische Blechumformung ist ein Hochgeschwindigkeitsumformprozess, der die Kraftwirkung hoher Impulsmagnetfelder zur plastischen Umformung elektrisch leitender Werkstoffe ausnutzt. Obwohl der Prozess seit vielen Jahren bekannt ist, wird in letzter Zeit ein zunehmendes Interesse an seiner Weiterentwicklung und industriellen Nutzung festgestellt. Daraus ergibt sich eine gesteigerte Nachfrage nach Simulationswerkzeugen, die in der Lage sind, solche Prozesse zu berechnen.

Vor diesem Hintergrund erfolgt im ersten Teil der vorliegenden Arbeit die Entwicklung und Implementierung eines Modells zur Lösung eines magneto-mechanisch gekoppelten Mehrfeldproblems auf Basis der Finite-Elemente-Methode für axialsymmetrische Probleme. Die Kopplung des mechanischen Teils zum elektromagnetischen erfolgt hier durch einen zusätzlichen Beitrag zur Volumenkraft, der von der Lorentzkraft herrührt. Umgekehrt findet die Kopplung des elektromagnetischen an den mechanischen Teil durch die Verschiebung des Bleches statt. Dabei hängt die Entwicklung des Magnetfeldes empfindlich von der vertikalen Verschiebung des Bleches ab. Die Modellierung dieses Vorgangs gelingt im Rahmen einer separaten Diskretisierung beider Teilsysteme unter Verwendung eines implizit gestaffelten Algorithmus. Dabei erfolgt die mechanische Finite-Elemente-Formulierung auf einem lagrangeschen Netz und die elektromagnetische auf einem eulerschen Netz. Fragestellungen, die das Konvergenzverhalten einer solchen Formulierung sowie den Datentransfer zwischen beiden Netzen betreffen, werden ausführlich diskutiert. Schließlich werden Simulationsergebnisse mit experimentellen Messungen verglichen.

Im zweiten Teil der Arbeit wird eine mögliche Wechselwirkung zwischen Elektronen- und Versetzungsbewegung untersucht, die unter dem Begriff Elektroplastizität bekannt ist. Dabei zeigen Experimente, die zur Untersuchung dieses Effekts entwickelt wurden, dass unter Einwirkung pulsartiger Stromstöße ein Abfall der Fließspannung von bis zu 60 % beobachtet werden kann. Die auftretenden Stromdichten, Abmessungen, Materialien und Pulslängen entsprechen denen, die bei der elektromagnetischen Blechumformung auftreten. Durch sorgfältige Berücksichtigung aller am Experiment beteiligten Effekte konnte gezeigt werden, dass der in den Experimenten beobachtete Abfall der Fließspannung in erster Linie durch einen thermoelastischen Ausdehnungseffekt hervorgerufen wird und insofern eine untergeordnete Bedeutung für die elektromagnetische Blechumformung hat.

Der dritte Teil der vorliegenden Arbeit bezieht sich auf weiterführende Konzepte zur Bestimmung von Materialparametern für metallische Werkstoffe bei hohen Verzerrungsgeschwindigkeiten, wie sie bei der elektromagnetischen Blechumformung auftreten. Hier erfolgt auf Basis des bestehenden Prozessmodells die Abschätzung der Materialparameter durch Abgleich von Finite-Elemente-Ergebnissen mit experimentellen Daten. Im Rahmen einer statistischen Vorgehensweise erfolgt weiterhin eine Fehler- und Sensitivitätsanalyse für die bestimmten Parameter. Wie sich herausstellt, kann das der Bestimmung zugrunde liegende Optimierungsproblem

vereinfacht werden. Insbesondere die schwache Abhängigkeit der Lorentzkräfte von den zu bestimmenden Materialparametern ermöglicht eine Identifikationsstrategie auf Basis schrittweise entkoppelter Lorentzkräfte. Nach einer erfolgreichen Validierung der vorgeschlagenen Konzepte erfolgt die Bestimmung der Materialparameter durch experimentell ermittelte Daten.

Im letzten Teil der Arbeit wird die dreidimensionale Modellierung von elektromagnetischen Umformvorgängen behandelt. Die Entwicklung eines entsprechenden Simulationswerkzeugs stellt eine wichtige Voraussetzung für die Weiterentwicklung dieses Umformvorgangs in Hinblick auf seine industrielle Einsetzbarkeit dar. In diesem Zusammenhang konnten ausgehend von bestehenden Entwicklungen weitere Konzepte zur Steigerung der Recheneffizienz entwickelt und implementiert werden, welche die Rechenzeit des Prozesses um ein Zehnfaches reduzieren. Die angesprochenen Konzepte basieren auf einer problembezogenen Diskretisierung der Umformanlage, einem Ansatz zum Austausch von Netzinformationen, welcher den Einsatz besonders effizienter Volumen-Schalenelemente ermöglicht, und einem Abbruchkriterium für das elektromagnetische Finite-Elemente-Problem. Schließlich erfolgt die Simulation eines 3D-Umformprozesses, womit tiefgehende Einblicke hinsichtlich der Entwicklung von Stromdichteverteilung, Magnetfeldentwicklung und plastischer Verformung ermöglicht werden.

Chapter 1

Algorithmic formulation and numerical implementation of coupled electromagnetic-inelastic continuum models for electromagnetic metal forming*

Abstract – The purpose of this work is the algorithmic formulation and implementation of a recent coupled electromagnetic-inelastic continuum field model (Svendsen and Chanda, 2005) for a class of engineering materials which can be dynamically formed using strong magnetic fields. Although in general relevant, temperature effects are for the applications of interest here minimal and are neglected for simplicity. In this case, the coupling is due on the one hand to the Lorentz force acting as an additional body force in the material. On the other hand, the spatio-temporal development of the magnetic field is very sensitive to changes in the shape of the workpiece, resulting in additional coupling. The algorithmic formulation and numerical implementation of this coupled model is based on mixed-element discretization of the deformation and electromagnetic fields combined with an implicit, staggered numerical solution scheme on two meshes. In particular, the mechanical degrees of freedom are solved for on an Lagrangian mesh and the electromagnetic ones on an Eulerian one. The issues of the convergence behavior of the staggered algorithm and the influence of data transfer between the meshes on the solution is discussed in detail. Finally, the numerical implementation of the model is applied to the modeling and simulation of electromagnetic tube and sheet forming.

1.1 Introduction

Multifield models, describing a mechanical structure whose evolution is coupled to the evolution of further fields as, *e.g.*, electromagnetic or temperature fields, arise in various practical engineering problems. A typical example is electromagnetic forming (EMF) representing a high-strain-rate forming method in which strain-rates of $\geq 10^3 \text{ s}^{-1}$ are achieved. In this process, deformation of the workpiece is driven by the interaction of a magnetic field generated by a coil adjacent to the workpiece with a current generated in the workpiece by this field. In particular, the interaction of these two fields results in an additional body force, *i.e.*, the Lorentz force, which drives deformation. EMF is but one of a number of high deformation-rate forming methods which offer certain advantages over other forming methods such as increase in formability for certain kinds of materials, reduction in wrinkling, the ability to combine forming and assembly operations, reduced tool making costs, and other benefits.

First attempts at the numerical simulation of electromagnetic metal forming include (Gourdin, 1989; Gourdin et al., 1989; Takatsu et al., 1988). In contrast to the first two, the interaction

*Stiemer et al. (2006a)

between the magnetic field and the shape of the workpiece was taken into account in the third. This is necessary in order to correctly model the influence of the change of shape of the workpiece during the electromagnetic forming process on the magnetic field and the force it exerts on the workpiece. More recently, Fenton and Daehn (1998) used the computer-code CALE to numerically simulate electromagnetic forming with complete electromagneto-mechanical coupling. This code is based on the so-called "arbitrary Lagrangian Eulerian"(ALE) method to solve the coupled system. In this method, the Lagrangian form of the field equations is used where mesh distortion is small, and otherwise the Eulerian form. With this approach, numerical problems can be avoided and the accuracy of the numerical solution is guaranteed. Focusing on the fast solution of three-dimensional fully coupled magnetomechanical problems, Schinnerl *et al.* (Schinnerl *et al.*, 2002) presented a numerical scheme for transient coupled systems based on an implicit multigrid method. Although their modeling of the mechanical system is restricted to the case of linear elasticity, realistic simulation results have been obtained for several experimental arrangements. In the work of El-Azab *et al.* (2003) the current state of modeling of EMF is discussed. As one can gather from such works, emphasis in the literature up to this point has been placed on the modeling and simulation of the field coupling and structure, which has correspondingly reached a high level of sophistication. The same statement, however, cannot be made concerning the material models used in the simulations. Such models are, for example, most often one-dimensional and identified with the help of uniaxial tension-compression tests. Fenton and Daehn (1998), for example, utilized the Steinberg model, which is a one-dimensional, purely mechanical stress-strain relation independent of the strain-rate. It is just such rate-dependence, however, which is characteristic of the behavior of metallic materials at high forming rates such as those achieved during EMF. This is in contrast to other high-speed manufacturing processes like high speed cutting, where such models have been considered (Bil *et al.*, 2004). Further, rate-dependence is accentuated at such high forming rates by the fact that the mechanical dissipation can be significant and the process takes place nearly adiabatically, resulting in a possible significant temperature increase.

The main purpose of the current work is the algorithmic formulation and numerical implementation of the isothermal special case of the continuum thermodynamic model for rate-dependent coupled electromagnetic-thermoelastic material behavior at large deformation developed by Svendsen and Chanda (2005) in order to simulate electromagnetic metal forming processes. Although in general significant for high-speed forming processes, the uniform nature of the electromagnetic forming process leads to a relatively small temperature increase which can be safely neglected for the applications of interest in this work. Consequently, such effects are neglected here. The paper begins (Section 1.2) with a brief summary of the basic mechanical and electromagnetic field relations of the model. This is followed (Section 1.3) by a brief summary of the thermodynamically-consistent constitutive and field relations. For simplicity, these is restricted to electromagnetic, elastic, viscoplastic material behavior with isotropic hardening. Next, attention is focused (Section 1.4) on the algorithmic formulation and finite element implementation of the mechanical part of the coupled field model for a moving body (*e.g.*, workpiece) in the Lagrangian context as based on standard backward-Euler integration and Newton-Raphson-based iterative solution. The algorithmic formulation is completed by that of the Eulerian-based electromagnetic initial boundary value problem. In the last part

of the work, the resulting combined algorithm in staggered form is formulated and investigated further. In particular, the convergence behavior of the resulting element formulations and numerical solution procedures is investigated for the case of a prescribed volume force (Section 1.5) as well as for the fully coupled problem (Section 1.6). Finally, the work ends with a brief summary and conclusions (Section 1.7).

Before we begin, consider first a few mathematical concepts and results to be used in the sequel. Euclidean vectors are represented in this work by lower-case bold italic letters $\mathbf{a}, \mathbf{b}, \dots$, and second-order Euclidean tensors by upper-case bold italic characters $\mathbf{A}, \mathbf{B}, \dots$. In particular, \mathbf{I} represents the second-order identity tensor. The scalar product of two such tensors is defined as usual by $\mathbf{A} \cdot \mathbf{B} := \text{tr}(\mathbf{A}^T \mathbf{B})$, with \mathbf{A}^T the transpose of \mathbf{A} . Let $|\mathbf{A}| := \sqrt{\mathbf{A} \cdot \mathbf{A}}$, $\text{sgn}(\mathbf{A}) := \mathbf{A}/|\mathbf{A}|$, $\text{sym}(\mathbf{A}) := \frac{1}{2}(\mathbf{A} + \mathbf{A}^T)$, $\text{skw}(\mathbf{A}) := \frac{1}{2}(\mathbf{A} - \mathbf{A}^T)$, $\text{sph}(\mathbf{A}) := \frac{1}{3} \text{tr}(\mathbf{A}) \mathbf{I}$, and $\text{dev}(\mathbf{A}) := \mathbf{A} - \text{sph}(\mathbf{A})$ represent the magnitude, sign, symmetric part, skew-symmetric part, spherical part, and deviatoric part, respectively, of any such tensor. For any invertible second-order tensor \mathbf{F} , let $\text{cof}(\mathbf{F}) := \det(\mathbf{F}) \mathbf{F}^{-T}$ represent its cofactor. Fourth-order Euclidean tensors are treated here as linear mappings of second-order tensors into second-order tensors. In particular, the tensor products

$$\begin{aligned} (\mathbf{A} \otimes \mathbf{C})[\mathbf{B}] &:= (\mathbf{B} \cdot \mathbf{C}) \mathbf{A}, \\ (\mathbf{A} \square \mathbf{C})[\mathbf{B}] &:= \mathbf{A} \mathbf{B} \mathbf{C}, \\ (\mathbf{A} \triangle \mathbf{C})[\mathbf{B}] &:= \mathbf{A} \mathbf{B}^T \mathbf{C}, \end{aligned} \tag{1.1}$$

for all $\mathbf{A}, \mathbf{B}, \mathbf{C} \in \text{Lin}(V, V)$ can be interpreted as such. In terms of these, note that $\mathbf{I} \square \mathbf{I}$ represents the fourth-order identity, and $\text{tsp} := \mathbf{I} \triangle \mathbf{I}$ transposition. Further, we have $\text{sym} = \frac{1}{2}(\mathbf{I} \square \mathbf{I} + \mathbf{I} \triangle \mathbf{I})$, $\text{skw} = \frac{1}{2}(\mathbf{I} \square \mathbf{I} - \mathbf{I} \triangle \mathbf{I})$, and $\text{dev} = \mathbf{I} \square \mathbf{I} - \frac{1}{3} \mathbf{I} \otimes \mathbf{I}$.

The tensor (dyadic) product $\mathbf{a} \otimes \mathbf{b}$ of any two Euclidean vectors \mathbf{a}, \mathbf{b} is defined by $(\mathbf{a} \otimes \mathbf{b})\mathbf{c} := (\mathbf{b} \cdot \mathbf{c})\mathbf{a}$. In addition, the axial vector of any skew-symmetric tensor \mathbf{W} is defined by $\text{axv}(\mathbf{W}) \times \mathbf{b} := \mathbf{A}\mathbf{b}$. The curl of any differentiable Euclidean vector field \mathbf{u} is defined by

$$\text{curl } \mathbf{u} := 2 \text{axv}(\text{skw}(\nabla \mathbf{u})) \tag{1.2}$$

as usual. The identities

$$\begin{aligned} \text{curl}(\mathbf{u} \times \mathbf{v}) &= (\text{div } \mathbf{v})\mathbf{u} - (\text{div } \mathbf{u})\mathbf{v} + (\nabla \mathbf{u})\mathbf{v} - (\nabla \mathbf{v})\mathbf{u}, \\ \text{div}(\mathbf{u} \times \mathbf{v}) &= \text{curl } \mathbf{u} \cdot \mathbf{v} - \text{curl } \mathbf{v} \cdot \mathbf{u}, \\ \text{curl}(\text{curl } \mathbf{u}) &= \nabla(\text{div } \mathbf{u}) - \text{div}(\nabla \mathbf{u}), \end{aligned} \tag{1.3}$$

for all differentiable vector fields \mathbf{u}, \mathbf{v} will be useful in the sequel. For notational simplicity, it proves advantageous to denote functions and their values by the same symbol. Other notations and mathematical concepts will be introduced as they arise in what follows.

1.2 Summary of basic model relations

Of principle interest in this work is the modeling of the dynamic interaction of strong electromagnetic fields with metallic solids resulting in their deformation. The system of interest

here consists of a *fixed* region $R \subset E$ of Euclidean point space E containing one or more solid bodies moving through it as well as the surrounding air. In the case of EMF, for example, these bodies include the workpiece (*e.g.*, sheet metal) and tool (see Figure 1.1 below). As such, R contains the reference (*e.g.*, initial) $B_r \subset R$ and current $B_c \subset R$ configurations of any of these bodies. Such bodies are modeled here as electromagnetic, mechanical continua characterized by a time dependent deformation field ξ together with the additional degrees of freedom represented by the electromagnetic fields to be introduced in what follows. Whereas the time dependent electromagnetic fields are defined on the entire region R , *i.e.*, also in the air surrounding stationary or moving material bodies, the deformation field ξ and all kinematic fields derived from it, are logically restricted to the configurations of deforming and moving bodies in what follows.

The following model represents a special case of the general continuum thermodynamic formulation (Svendsen and Chanda, 2005) to the case in which a strong magnetic field induces electric currents in thermoelastic, viscoplastic electric conductors and so a Lorentz force resulting in their deformation. This is the basic idea underlying the method of electromagnetic metal forming. Since the relevant electromagnetic frequencies for the engineering structures of interest here (*i.e.*, less than 10 MHz) correspond to electromagnetic wavelengths which are much larger than these structures, note that the wave character of the electromagnetic fields is insignificant, and can be neglected (*e.g.*, Moon, 1980, §2.2 and §2.8). For simplicity, any thermoelectric effects, as well as any magnetostriction (*i.e.*, the Hall effect), are also neglected here. This is reasonable for conductors such as aluminum or copper at room temperature and “low” magnetic fields. Under these conditions, the inhomogeneous “diffusion” equation

$$\hat{\mathbf{a}} + \kappa_{\text{EM}} \text{curl}_s(\text{curl}_s \mathbf{a}) + \nabla_s \zeta = \mathbf{0} \quad (1.4)$$

may be derived (Svendsen and Chanda, 2005) for the electromagnetic vector potential \mathbf{a} in the context of Ohm’s law

$$\mathbf{j} = \sigma_{\text{EM}} \boldsymbol{\epsilon} \quad (1.5)$$

for the conductive flux \mathbf{j} . Here, κ_{EM} represents the magnetic diffusivity. Further,

$$\hat{\mathbf{a}} := \dot{\mathbf{a}} + \mathbf{L}^T \mathbf{a} = \partial \mathbf{a} + (\nabla_s \mathbf{a}) \mathbf{v} + \mathbf{L}^T \mathbf{a} \quad (1.6)$$

represents an objective time-derivative of \mathbf{a} with respect to a material moving with spatial velocity \mathbf{v} . In this expression, ∂ is the partial time-derivative operator, $\mathbf{L} = \nabla_s \mathbf{v}$ the spatial velocity gradient, ∇_s the spatial gradient operator, and curl_s the spatial curl operator. Further, σ_{EM} represents the electrical conductivity,

$$\zeta := \chi - \mathbf{a} \cdot \mathbf{v} \quad (1.7)$$

a Euclidean frame-indifferent form of the scalar potential χ ,

$$\boldsymbol{\epsilon} = \mathbf{e} + \mathbf{v} \times \mathbf{b} \quad (1.8)$$

the spatial electromotive intensity, \mathbf{e} the spatial electric field, and \mathbf{b} the spatial magnetic flux. Outside of the moving body in R , *i.e.*, in the surrounding air, \mathbf{v} and \mathbf{L} are neglected. As usual,

\mathbf{a} and χ determine \mathbf{b} and \mathbf{e} via the potential relations

$$\begin{aligned}\mathbf{b} &= \operatorname{curl}_s \mathbf{a}, \\ -\mathbf{e} &= \partial \mathbf{a} + \nabla_s \chi,\end{aligned}\tag{1.9}$$

in the context of Maxwell's equations (Jackson, 1975, §6.4). In particular, these result in the form

$$-\boldsymbol{\epsilon} = \partial \mathbf{a} + \nabla_s \chi + \operatorname{curl}_s \mathbf{a} \times \mathbf{v} = \hat{\mathbf{a}} + \nabla_s \zeta\tag{1.10}$$

for $\boldsymbol{\epsilon}$. In addition, Maxwell's equations and (1.9)₂ together with the Coulomb gauge condition

$$\operatorname{div}_s \mathbf{a} = 0\tag{1.11}$$

(Jackson, 1975, §6.5) on \mathbf{a} yield in the alternative form

$$\hat{\mathbf{a}} - \kappa_{\text{EM}} \operatorname{div}_s(\nabla_s \mathbf{a}) + \nabla_s \zeta = \mathbf{0}\tag{1.12}$$

for (1.4) via (1.3)₃ together with the field relation

$$\operatorname{div}_s(\nabla_s \chi) = \nabla_s^2 \chi = 0\tag{1.13}$$

for the scalar potential χ . The weak forms of these last two field relations are then given by¹

$$\begin{aligned}\int_R \hat{\mathbf{a}} \cdot \mathbf{a}_* + \{\zeta \mathbf{I} + \kappa_{\text{EM}} \nabla_s \mathbf{a}\} \cdot \nabla_s \mathbf{a}_* &= \int_{\partial R} \{\zeta \mathbf{I} + \kappa_{\text{EM}} \nabla_s \mathbf{a}\} \mathbf{n} \cdot \mathbf{a}_* \\ \int_R \nabla_s \chi \cdot \nabla_s \chi_* &= \int_{\partial R} (\nabla_s \chi \cdot \mathbf{n}) \chi_*\end{aligned}\tag{1.14}$$

with respect to R via (1.3)₂ for all test fields \mathbf{a}_* and χ_* . As usual, these vanish on those parts of ∂R where \mathbf{a} and χ , respectively, are specified. On the timescale $\tau_{\text{Exp}} \sim 10^{-4}$ s relevant to processes such as electromagnetic metal forming, the typical order of magnitude $\kappa_{\text{EM}} \sim 10^{-1} \text{ m}^2 \text{ s}^{-1}$ for the magnetic diffusivity of metals implies that “significant” magnetic diffusion takes place over lengthscales of $\sqrt{\kappa_{\text{EM}} \tau_{\text{Exp}}} \sim 10$ cm. Since this is significantly larger than the smallest dimension of the engineering structures of interest (e.g., sheet metal thickness ~ 1 mm), magnetic diffusion will be important in the applications to be discussed below.

Turning next to the mechanical part of the coupled model, the weak momentum balance for the deformation field $\boldsymbol{\xi}$ is given by

$$\int_{B_r} (\varrho_r \ddot{\boldsymbol{\xi}} - \mathbf{f}) \cdot \boldsymbol{\xi}_* + \mathbf{P} \cdot \nabla_r \boldsymbol{\xi}_* = \int_{\partial B_r} |\operatorname{cof}(\mathbf{F}) \mathbf{n}_r| \mathbf{t}_c \cdot \boldsymbol{\xi}_*\tag{1.15}$$

with respect to the referential configuration $B_r \subset R$ for all corresponding test fields $\boldsymbol{\xi}_*$ vanishing on those parts of the current boundary ∂B_c where $\boldsymbol{\xi}$ is specified. Here,

$$\mathbf{f} = \det(\mathbf{F}) \mathbf{l} = \det(\mathbf{F}) \mathbf{j} \times \mathbf{b}\tag{1.16}$$

¹The volume dv and surface da elements are dispensed with in the corresponding integrands in this work for notational simplicity.

represents the Lorentz (body) force (density), \mathbf{P} the first Piola-Kirchhoff stress, $\mathbf{F} := \nabla_r \boldsymbol{\xi}$ the deformation gradient, and \mathbf{t}_c the current boundary traction. In the previous work under certain circumstances (*e.g.*, tube forming: Beerwald et al., 1999; Fenton and Daehn, 1998), the Lorentz force has also been represented as a boundary pressure. Indeed, this is based on the alternative form

$$\int_{B_c} \mathbf{j} \times \mathbf{b} = \int_{\partial B_c} [(\mathbf{b} \cdot \mathbf{n}_c)(\mathbf{h} \cdot \mathbf{n}_c) - p_M] \mathbf{n}_c + (\mathbf{b} \cdot \mathbf{n}_c) \mathbf{n}_c \times (\mathbf{h} \times \mathbf{n}_c) \quad (1.17)$$

for the Lorentz force itself as a boundary integral over the current boundary ∂B_c via the divergence theorem, with

$$p_M := \frac{1}{2} (\mathbf{b} \cdot \mathbf{h}) = \frac{1}{2} \mu_{EM} \mathbf{h} \cdot \mathbf{h} \quad (1.18)$$

the so-called magnetic pressure. From this, we see that, if \mathbf{b} is parallel to ∂B_c , *i.e.*, if $\mathbf{b} \cdot \mathbf{n}_c = 0$, then the Lorentz force is equivalent to a pressure at the boundary. Again, this is exactly the type of boundary condition realized in certain types of applications, *e.g.*, certain types of electromagnetic metal forming (*e.g.*, tube forming: Beerwald et al., 1999; Fenton and Daehn, 1998). For other cases, however, this is no longer true, and in general the Lorentz force must be treated as a body force (density).

The mechanical model relations are completed by the specification of the material model. Here, attention is restricted to such a model for the metallic workpiece, which is modeled here as a hyperelastic, viscoplastic material. For simplicity, the (mild) elastic and flow anisotropy of the metals of interest (*e.g.*, Al) is neglected here, as well as any kinematic hardening. More generally, *e.g.*, for the case of deformation-induced anisotropic flow behavior (*e.g.*, Reese and Svendsen, 2003; Svendsen, 2001), this is of course no longer possible. Since the metal forming processes of interest here are predominantly monotonic in nature, however, this last assumption is not unreasonable. In this case, the constitutive model is specified via the form of the referential free energy density $\psi_r(\ln \mathbf{V}_E, \epsilon_P)$ together with the evolution relations for the elastic left logarithmic stretch tensor $\ln \mathbf{V}_E$ and accumulated equivalent inelastic deformation measure ϵ_P . In the context of small elastic strain, the usual Hooke-based form

$$\psi_r(\ln \mathbf{V}_E, \epsilon_P) = \frac{1}{2} \kappa_r (\mathbf{I} \cdot \ln \mathbf{V}_E)^2 + \mu_r \text{dev}(\ln \mathbf{V}_E) \cdot \text{dev}(\ln \mathbf{V}_E) + \psi_P(\epsilon_P) \quad (1.19)$$

is relevant. Another common assumption in the non-isothermal context in the case of metals is that of constant specific heat (*e.g.*, Rosakis et al., 2000). Here, κ_r represents the bulk modulus, μ_r the shear modulus, and $\psi_P(\epsilon_P)$ the contribution from energy storage due to isotropic hardening processes as usual. From (1.19), one obtains in particular the usual hyperelastic form

$$\mathbf{K} = \partial_{\ln \mathbf{V}_E} \psi_r = 3\kappa_r \text{sph}(\ln \mathbf{V}_E) + 2\mu_r \text{dev}(\ln \mathbf{V}_E) \quad (1.20)$$

for the Kirchhoff stress $\mathbf{K} = \mathbf{P}\mathbf{F}^T$. As usual, $\psi_P(\epsilon_P)$ is estimated with the help of fits to the quasi-static yield curve for the materials of interest at room temperature, as discussed in what follows.

Consider next the evolution of the internal variables and the inelastic behavior. In the metallic polycrystalline materials of interest at low-to-moderate homologous temperature, inelastic deformation processes are controlled predominantly by the activation of dislocation glide on glide systems (*e.g.*, Kocks and Mecking, 2003; Teodosiu, 1997). Indeed, this seems to be the

case even at high strain-rates (*e.g.*, Frost and Ashby, 1982). Apparently, higher homologous temperature is required for other mechanics such as dislocation climb or even dynamic recrystallization to begin playing a role. Resistance to dislocation glide arising due to obstacles and other factors is related in the phenomenological context to hardening behavior. Quasi-static processes of this nature contributing to energy storage in the material result in the contribution

$$-\varsigma_{\text{P}} := \psi_{r, \epsilon_{\text{P}}} \quad (1.21)$$

to the effective quasi-static flow stress in the material. Such resistance to dislocation motion can be overcome by thermal fluctuation under the action of the local effective stress, represented in the current phenomenological context by $\sigma_{\text{vM}}(\mathbf{K}) + \varsigma_{\text{P}} - \sigma_{\text{F0}}$, where $\sigma_{\text{vM}}(\mathbf{K})$ represents the von Mises effective stress with respect to \mathbf{K} , and σ_{F0} is the initial flow stress. On this basis,

$$f_{\text{P}}(\mathbf{K}, \varsigma_{\text{P}}) := \sigma_{\text{vM}}(\mathbf{K}) + \varsigma_{\text{P}} - \sigma_{\text{F0}} \quad (1.22)$$

represents an activation measure or overstress in the current rate-dependent context. A power-law approximation of the more exact transition-state-based micromechanical relations for the kinetics of dislocation glide (*e.g.*, Kocks and Mecking, 2003; Teodosiu, 1997) leads to the power-law form

$$\phi(\epsilon_{\text{P}}, \mathbf{D}, \mathbf{K}, \varsigma_{\text{P}}) = \frac{\gamma_{\text{P}}(\epsilon_{\text{P}}, \mathbf{D}) \sigma_{\text{P}}(\epsilon_{\text{P}}, \mathbf{D})}{m(\epsilon_{\text{P}}, \mathbf{D}) + 1} \left\langle \frac{f_{\text{P}}(\mathbf{K}, \varsigma_{\text{P}})}{\sigma_{\text{P}}(\epsilon_{\text{P}}, \mathbf{D})} \right\rangle^{m_{\text{P}}(\epsilon_{\text{P}}, \mathbf{D})+1} \quad (1.23)$$

upon which the evolution of the internal variables is based. Here, σ_{F0} represents the initial flow stress, γ_{P} a characteristic strain-rate, σ_{P} the characteristic or effective activation stress magnitude, and m the strain-rate exponent. Further, $\langle x \rangle := \frac{1}{2}(x + |x|)$ represents the ramp function. As indicated, γ_{P} , σ_{P} and m_{P} are in general functions of accumulated inelastic deformation and deformation rate. For simplicity, however, these material properties will be treated as constants in the algorithmic formulation to follow. To indicate this, we write $\gamma_0 \hat{=} \gamma_{\text{P}}$, $\sigma_0 \hat{=} \sigma_{\text{P}}$, and $m_0 \hat{=} m_{\text{P}}$, in what follows. The form (1.23) determines the evolution relations

$$\begin{aligned} -\ln \mathbf{V}_{\text{E}}^* &= \partial_{\mathbf{K}} \phi = \sqrt{\frac{3}{2}} \operatorname{sgn}(\operatorname{dev}(\mathbf{K})) \dot{\epsilon}_{\text{P}} \quad (\mathbf{K} \neq \mathbf{0}), \\ \dot{\epsilon}_{\text{P}} &= \partial_{\varsigma_{\text{P}}} \phi = \gamma_0 \left\langle \frac{f_{\text{P}}}{\sigma_0} \right\rangle^{m_0} \quad (f_{\text{P}} > 0), \end{aligned} \quad (1.24)$$

for the evolution of the internal variables, with

$$\ln \mathbf{V}_{\text{E}}^* := \frac{1}{2} \ln(\mathbf{F} \dot{\mathbf{C}}_{\text{P}}^{-1} \mathbf{F}^{\text{T}}) \quad (1.25)$$

in terms of the inverse plastic right Cauchy-Green deformation $\mathbf{C}_{\text{P}}^{-1}$. As indicated, ϕ is differentiable in ς_{P} everywhere except at $f_{\text{P}} = 0$, as well as in \mathbf{K} everywhere except at $f_{\text{P}} = 0$ and at $\mathbf{K} = \mathbf{0}$. The corresponding subdifferentials exist everywhere. In the context of these forms for the evolution of the internal variables, the constraint $\gamma_{\text{P}}(\epsilon_{\text{P}}, \mathbf{0}) = 0$ on the constitutive form of γ_{P} follows from the general thermodynamic analysis (Svendsen and Chanda, 2005). In addition, Ohm's law (1.5) together with the assumption that these evolution relations are independent of ϵ implies $\sigma_{\text{EM}} \geq 0$. Lastly, the restriction that $\gamma_{\text{P}, \mathbf{DD}}(\epsilon_{\text{P}}, \mathbf{0})$ be non-negative definite (*i.e.*, for $f_{\text{P}} > 0$) follows from the thermodynamic analysis via the assumption that the non-equilibrium (*i.e.*, dynamic) part of \mathbf{K} is negligible. For more details, the reader is referred to Svendsen and Chanda (2005).

1.3 Initial boundary value problem for EMF

In the rest of this work, attention is focused for simplicity on the application of the general model relations from the last section to the case of the electromagnetic metal forming of axisymmetric structures (see Section 1.5 and Section 1.6). In particular, attention is focused here on the case of the electromagnetic metal forming of circular sheet metal plates as shown in Figure 1.1.

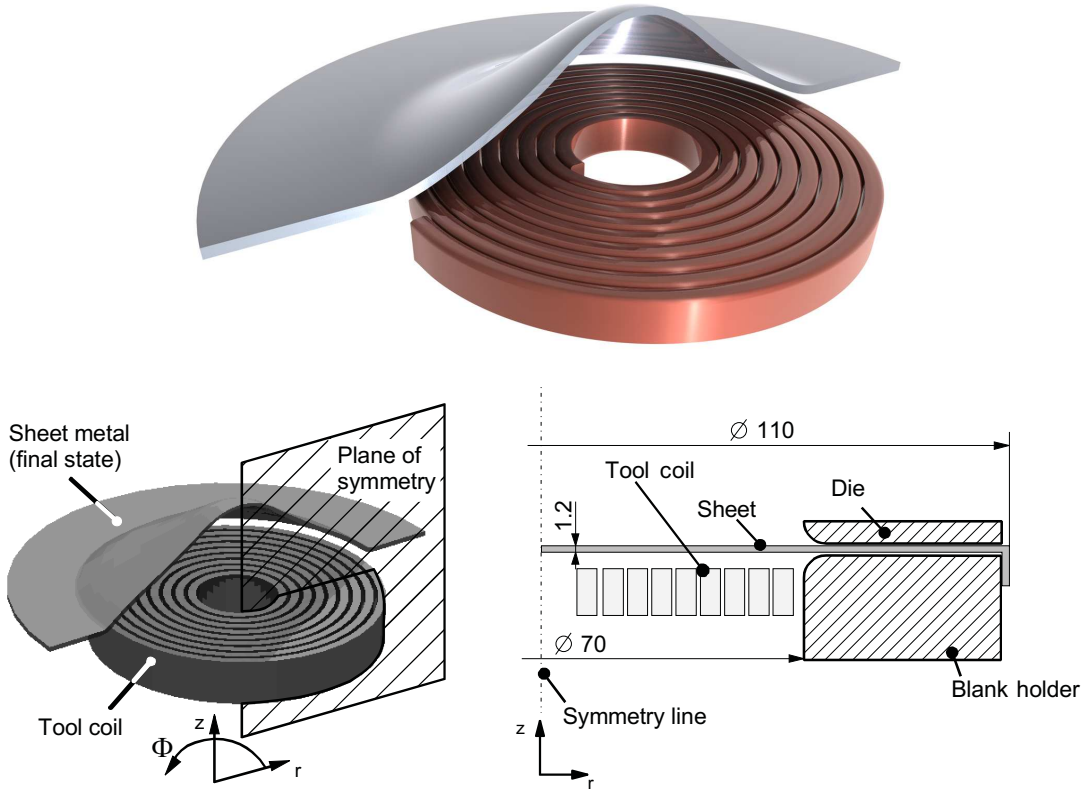


Figure 1.1: Electromagnetic metal forming of circular sheet metal plates. In this method, an electric current in the tool coil induces a magnetic field and electric current in the sheet metal plate, resulting in a Lorentz (body) force (density) driving its deformation. As shown, the sheet metal plate is clamped down radially by a die and blank holder. For simplicity, the structure is approximated in this work as being axisymmetric. See text for details.

For the formulation of the corresponding coupled initial boundary value problem, this structure is idealized as shown in Figure 1.2.

Let C_c represent the current configuration of the tool, S_c that of the workpiece, and R the region containing these as well as the die and surrounding air. For simplicity, attention is restricted in this work to cases in which the tool, die and air are assumed to be stationary. Consequently, only the workpiece is assumed to move. The tool consists of an electrically-conducting ($\sigma_{EM} \neq 0$) copper coil embedded in a non-conducting ($\sigma_{EM} = 0$) resin matrix. Let L_c represent the interface between the copper coil and the resin matrix in the tool. Further, let F_{c1} and F_{c2} represent the surfaces at the beginning and end of the copper coil connecting this coil with the rest of the electrical circuit through which current flows. These have known voltages U_1 and U_2 , respectively, across them. In this case, $R \setminus (C_c \cup S_c)$ represents the region surrounding the tool

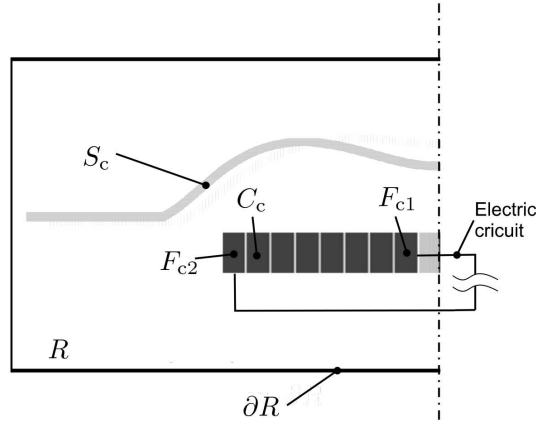


Figure 1.2: Computational domains for the coupled initial boundary value problem. Here, R represents the entire domain with boundary ∂R (at which the magnetic field has effectively decayed to zero), S_c the current configuration of the sheet metal workpiece, and C_c that of the tool. Further, F_{c1} and F_{c2} represent the surfaces of the tool coil connected to the electric circuit.

and workpiece containing air which, like the resin matrix, is assumed to be non-conducting. Under these conditions, the restriction of χ to C_c is determined by the boundary value problem

$$\begin{aligned}
 \nabla_s^2 \chi &= 0 && \text{in } C_c, \\
 \chi &= U_1 && \text{on } F_{c1}, \\
 \chi &= U_2 && \text{on } F_{c2}, \\
 \nabla_s \chi \cdot \mathbf{n}_c &= 0 && \text{on } L_c,
 \end{aligned} \tag{1.26}$$

via (1.13). Here, \mathbf{n}_c denotes the outer unit normal vector on the surface of the tool coil. In particular, the boundary condition on coil-matrix interface L_c insures that the χ -field in the non-conducting resin matrix does not contribute to the current flux \mathbf{j} in the copper coil. Outside $C_c \cup S_c$ in R , *i.e.*, in the surrounding air, χ is determined by

$$\begin{aligned}
 \nabla_s^2 \chi &= 0 && \text{in } R \setminus (C_c \cup S_c), \\
 \chi &= \chi|_{\partial C_c} && \text{on } \partial C_c, \\
 \chi &= 0 && \text{on } \partial R, \\
 \nabla_s \chi \cdot \mathbf{n}_c &= 0 && \text{on } \partial S_c.
 \end{aligned} \tag{1.27}$$

The boundary conditions on ∂C_c are based on the continuity of χ which is a consequence of the existence of its gradient by definition. These boundary values arise from the computation of the scalar potential inside C_c . Analogous to that (1.26₄) on the coil-matrix interface, the boundary condition on ∂S_c insures that the χ -field in the non-conducting air does not contribute to \mathbf{j} in the workpiece. Instead of specifying U on F_{c1} and F_{c2} , one may alternatively specify the total

current $I = I(t)$ flowing through C_c . In this case, the coupled problem

$$\begin{aligned} \partial \mathbf{a} - \kappa_{\text{EM}} \nabla_s^2 \mathbf{a} + \nabla_s \chi &= \mathbf{0} & \text{in } R \setminus S_c, \\ \nabla_s^2 \chi &= 0 & \text{in } R \setminus (C_c \cup S_c), \\ \nabla_s^2 \chi &= 0 & \text{in } C_c, \\ \nabla_s \chi \cdot \mathbf{n}_c &= 0 & \text{on } L_c, \end{aligned} \quad (1.28)$$

is solved for \mathbf{a} and χ subject to boundary conditions for \mathbf{a} on ∂R , for χ on ∂R , ∂C_c and ∂S_c as described above and the constraint condition

$$- \int_{A_c} (\partial \mathbf{a} + \nabla_s \chi) \cdot \mathbf{n}_c = \sigma_{\text{EM}}^{-1} I \quad (1.29)$$

for any cross sectional surface A_c perpendicular to L_c . Note that (1.28)₁ describes a degenerate diffusion process. Degeneration occurs in $R \setminus (C_c \cup S_c)$, where κ_{EM} equals ∞ . In this region the boundary value problem is elliptic. In the special case of axisymmetry under consideration here, note also that the Coulomb gauge condition (1.11) is satisfied identically. Lastly, consider the initial boundary value problem for the deformable workpiece S_c . As this part is electrically-conducting and surrounded by air, we have

$$\begin{aligned} \nabla_s^2 \chi &= 0 & \text{in } S_c, \\ \hat{\mathbf{a}}_c - \kappa_{\text{EM}} \nabla_s^2 \mathbf{a}_c + \nabla_s \zeta &= \mathbf{0} & \text{in } S_c, \\ \nabla_s \chi \cdot \mathbf{n}_c &= 0 & \text{on } \partial S_c, \end{aligned} \quad (1.30)$$

for the restriction \mathbf{a}_c of the vector potential to S_c , as follows from (1.11), (1.12) and (1.13).

Although the spiral-shaped tool coil is not exactly axisymmetric, it is approximated as such here. To this end, assuming that C_c consists of n windings, each winding is approximated by a torus of the same cross section. The resulting n tori are then cut in the (r, z) -plane at $\varphi = 0$. In order to simulate the fact that each torus is in fact the arm of a spiral, the cross sections at $\varphi = 0$ and $\varphi = 2\pi$ are treated electromagnetically as being continuous with respect to χ . Continuity of potential then implies that U at $\varphi = 0$ (*i.e.*, except in the first torus) is determined by that in the preceding torus at $\varphi = 2\pi$. Let W_{ck} denote the current configuration of the k^{th} torus, and U_k the potential of W_{ck} at $\varphi = 0$. Under these assumptions, the restriction χ_k of $\chi = \chi(r, \varphi, z)$ to W_{ck} satisfies

$$\begin{aligned} \nabla_s^2 \chi_k &= 0 & \text{in } W_{ck}, \\ \chi_k &= U_k & \text{at } \varphi = 0, \\ \chi_k &= U_{k+1} & \text{at } \varphi = 2\pi, \\ \nabla_s \chi_k \cdot \mathbf{n}_k &= 0 & \text{on } \partial W_{ck}. \end{aligned} \quad (1.31)$$

The solution of this boundary value problem is given by

$$\chi_k(r, \varphi, z) = U_k + \Delta U_k \frac{\varphi}{2\pi}, \quad (1.32)$$

with $\Delta U_k = U_{k+1} - U_k$. For the determination of

$$\nabla_s \chi_k = \frac{\Delta U_k}{2\pi r} \mathbf{e}_\varphi, \quad (1.33)$$

only the potential differences ΔU_k need to be considered. They can be obtained from the measured total current $I = I(t)$, which is equal in all tori W_{ck} , $k = 1, \dots, n$, since they are connected in series. The sum over all currents flowing through an arbitrary cross section A_{ck} of the k^{th} torus then yields

$$-\sigma_{\text{EM}}^{-1} I = \int_{A_{ck}} (\partial \mathbf{a}_k + \nabla_s \chi_k) \cdot \mathbf{n}_k = \int_{A_{ck}} \left(\partial \mathbf{a}_k + \frac{\Delta U_k}{2\pi r} \mathbf{e}_\varphi \right) \cdot \mathbf{n}_k \quad (1.34)$$

in the context of (1.29), where \mathbf{a}_k denotes the restriction of the vector potential to the k^{th} torus W_{ck} . The last relation yields the result

$$\Delta U_k = - \left\{ \int_{A_{ck}} \frac{1}{2\pi r} \mathbf{e}_\varphi \cdot \mathbf{n}_k \right\}^{-1} \left\{ \sigma_{\text{EM}}^{-1} I + \int_{A_{ck}} \partial \mathbf{a}_k \cdot \mathbf{n}_k \right\} \quad (1.35)$$

for ΔU_k . In particular, for the case of a coil with rectangular cross section,

$$\Delta U_k = -2\pi \left(h \ln \frac{b_k}{a_k} \right)^{-1} \left\{ \sigma_{\text{EM}}^{-1} I + \int_{A_{ck}} \partial \mathbf{a}_k \cdot \mathbf{n}_k \right\}, \quad (1.36)$$

where h is the height (in z -direction) of each winding, a_k the inner, and b_k the outer radius of the k^{th} winding. On this basis of this formulation, then, one obtains the integro-differential equation

$$\partial \mathbf{a}_k - \kappa_{\text{EM}} \nabla_s^2 \mathbf{a}_k + \frac{\Delta U_k}{2\pi r} \mathbf{e}_\varphi = \mathbf{0} \quad (1.37)$$

for the restriction \mathbf{a}_k of \mathbf{a} to W_{ck} , with ΔU_k given by (1.36).

In the current axisymmetric situation, the relations (1.28), (1.30) and (1.37) result in a piecewise-continuous form for \mathbf{a} (in contrast to the three-dimensional case in which \mathbf{a} experiences jumps). In turn, this justifies standard finite element methods. The boundary condition of the scalar potential results from the continuity of the normal component of the current density as well as the tangential component of the electric field, as mentioned in connection with (1.27). Since χ is a harmonic function in S_c fulfilling a homogeneous Neumann boundary condition on the whole boundary according to (1.30), it must be constant there. Hence

$$\hat{\mathbf{a}} + \nabla_s \zeta = \partial \mathbf{a} + \text{curl}_s \mathbf{a} \times \mathbf{v} \quad (1.38)$$

applies there by virtue of (1.6) and (1.7). In summary,

$$\partial \mathbf{a} - \kappa_{\text{EM}} \nabla_s^2 \mathbf{a} = \begin{cases} 0 & \text{in } R \setminus (C_c \cup S_c) \\ -\text{curl}_s \mathbf{a} \times \mathbf{v} & \text{in } S_c \\ c_k \left\{ \sigma_{\text{EM}}^{-1} I + \int_{A_{ck}} \partial \mathbf{a} \cdot \mathbf{n}_k \right\} \mathbf{e}_\varphi & \text{in } W_{ck} \end{cases} \quad (1.39)$$

with piecewise smooth coefficients for \mathbf{a} in the whole region R , and with

$$c_k := \left\{ r \int_{A_{ck}} \frac{1}{r} \mathbf{e}_\varphi \cdot \mathbf{n}_k \right\}^{-1}. \quad (1.40)$$

Since (1.39) is homogeneous in $R \setminus (C_c \cup S_c)$, no problems arise from the degeneration $\kappa_{\text{EM}} = \infty$ there. In particular, note that piecewise smoothness applies since κ_{EM} and the right-hand side of (1.39) exhibits jumps at material interfaces. In general, this is also the case because \mathbf{a} is not continuous in R ; in the axisymmetric case, however, it is. As the flux density of a magnetic dipole decays like $O(|x|^{-3})$ if the norm of the spatial variable x tends to infinity, it is admissible to assume homogeneous Dirichlet boundary conditions on ∂R to good accuracy. After multiplication with suitable test functions \mathbf{a}_* in (1.39) and partial integration, the reduced form

$$\begin{aligned} & \int_R \partial \mathbf{a} \cdot \mathbf{a}_* + \int_R \kappa_{\text{EM}} \nabla_{\text{s}} \mathbf{a} \cdot \nabla_{\text{s}} \mathbf{a}_* + \int_{S_c} \text{curl}_{\text{s}} \mathbf{a} \times \mathbf{v} \cdot \mathbf{a}_* \\ &= \sum_{k=1}^n \int_{W_{ck}} c_k \left\{ \sigma_{\text{EM}}^{-1} I + \int_{A_{ck}} \partial \mathbf{a}_k \cdot \mathbf{n}_k \right\} \mathbf{e}_\varphi \cdot \mathbf{a}_* \end{aligned} \quad (1.41)$$

of the general weak forms (1.14) follows. This is the basis of the finite element solution to be discussed in what follows. Note that the condition $\mathbf{v} = 0$ outside S_c has been taken into account here.

1.4 Algorithmic formulation of the coupled model

We begin with the mechanical part of the model. Its algorithmic formulation is carried out here in the standard context of backward-Euler integration of the local evolution relations (*e.g.*, Simo and Hughes, 1998) and their implicit solution via Newton-Raphson iteration in the context of the implicit function theorem. Consistent linearization of the resulting algebraic system then facilitates the corresponding element formulation of the material model and its incorporation in the finite element solution of the dynamic initial boundary value problem.

To this end, the time interval $[0, d]$ of interest is split into m subintervals $[0, t_1], \dots, [t_{m-1}, t_m]$, such that $[0, d] = \bigcup_{i=0}^{m-1} [t_i, t_{i+1}]$ with $t_0 = 0$, $t_i < t_{i+1}$ and $t_m = d$. As usual, assume that the initial boundary value problem and internal variable evolution relations have been solved up to the discrete time $t = t_n$, such that $\boldsymbol{\xi}_n$, \mathbf{a}_n , and χ_n , together with their spatial and temporal derivatives, as well as the corresponding internal variables, are all known in the corresponding region of Euclidean space at this time. As discussed in the previous section, the difference in electromagnetic and mechanical timescales, together with the distinct nature of the respective fields involved (*i.e.*, Eulerian in the electromagnetic case, Lagrangian in the mechanical large deformation context), suggest that a staggered numerical solution procedure based on separate meshes for the electromagnetic and mechanical field problems will be most efficient. Since we are neglecting temperature effects here, the influence of the electromagnetic fields on the development of the mechanical fields is restricted to the Lorentz force (1.16). Via Ohm's law (1.5) for \mathbf{j} and the expression (1.10) for the electromotive intensity $\boldsymbol{\epsilon}$, we see that the spatial form \mathbf{l} of this force depends in general on both electromagnetic and mechanical fields as well as their spatial and temporal derivatives via (1.5), (1.9) and (1.16). Since the electromagnetic fields vary on a timescale much smaller than that of the mechanical fields, a scaling analysis shows that the convective term $\mathbf{b} \times \mathbf{v} = \text{curl}_{\text{s}} \mathbf{a} \times \mathbf{v}$ is much smaller than the others and can be neglected. In this case, we work with the algorithmic approximation

$$\mathbf{l}_{n+1} \approx \sigma_{\text{EM}} \text{curl}_{\text{s}} \mathbf{a}_{n+1} \times (\partial \mathbf{a}_{n+1} + \nabla_{\text{s}} \chi_{n+1}) \quad (1.42)$$

for the current Lorentz force which is then “purely electromagnetic” in character. In particular, in the context of the staggered approach being pursued here, the purely electromagnetic terms $\text{curl}_s \mathbf{a}_{n+1}$, $\partial \mathbf{a}_{n+1}$ and $\nabla_s \chi_{n+1}$ appearing here are treated in the mechanical part of the staggered algorithm as being known and fixed.

The next global step begins with the update of the boundary conditions to the next discrete time $t = t_{n+1}$ for the time interval $[t_n, t_{n+1}]$ of duration $t_{n+1,n} := t_{n+1} - t_n$. Consider first the local algorithm at the Gauss-point level for the internal variables and the Kirchhoff stress \mathbf{K} . In the backward-Euler context, these are determined as usual as implicit functions of the current (unknown) deformation gradient \mathbf{F}_{n+1} and (in the current rate-dependent context) time step size $t_{n+1,n}$. In particular, the backward-Euler integration of (1.24) over $[t_n, t_{n+1}]$ results in the algorithmic relations

$$\begin{aligned} \text{sph}(\ln \mathbf{V}_{E n+1}) &= \text{sph}(\ln \mathbf{V}_{E n+1,n}^{\text{tr}}), \\ \text{sgn}(\text{dev}(\ln \mathbf{V}_{E n+1})) &= \text{sgn}(\text{dev}(\ln \mathbf{V}_{E n+1,n}^{\text{tr}})), \end{aligned} \quad (1.43)$$

in the context of (1.20) and (1.24)₁, and so in the reduced two-dimensional algorithmic system

$$\begin{aligned} \epsilon_{E n+1} &= \epsilon_{E n+1}^{\text{tr}} - \sqrt{\frac{3}{2}} (\epsilon_{P n+1} - \epsilon_{P n}), \\ \epsilon_{P n+1} &= \epsilon_{P n} + \gamma_0 \langle f_{P n+1,n} / \sigma_0 \rangle^{m_0} t_{n+1,n}, \end{aligned} \quad (1.44)$$

for $\epsilon_{E n+1} := |\text{dev}(\ln \mathbf{V}_{E n+1})|$ and $\epsilon_{P n+1}$, respectively, with $\epsilon_{E n+1}^{\text{tr}} := |\text{dev}(\ln \mathbf{V}_{E n+1,n}^{\text{tr}})|$. Here,

$$\ln \mathbf{V}_{E n+1,n}^{\text{tr}} = \ln \mathbf{V}_{E n}^{\text{tr}}(\mathbf{F}_{n+1}) := \frac{1}{2} \ln(\mathbf{F}_{n+1} \mathbf{C}_{P n}^{-1} \mathbf{F}_{n+1}^{\text{T}}) \quad (1.45)$$

represents as usual the trial value of $\ln \mathbf{V}_{E n+1}$, with $\mathbf{F}_{n+1,n} := \mathbf{F}_{n+1} \mathbf{F}_n^{-1}$ the relative deformation gradient. From (1.44), one obtains the three-dimensional implicit algebraic system

$$\begin{aligned} \mathbf{r}_{\epsilon_{E n+1,n}}(\epsilon_{E n+1}, \epsilon_{P n+1}, \mathbf{F}_{n+1}) &= 0, \\ \mathbf{r}_{\epsilon_{P n+1,n}}(\epsilon_{E n+1}, \epsilon_{P n+1}, \mathbf{F}_{n+1}) &= 0, \end{aligned} \quad (1.46)$$

of non-linear algebraic relations for $\epsilon_{E n+1}$ and $\epsilon_{P n+1}$, where

$$\begin{aligned} \mathbf{r}_{\epsilon_{E n+1,n}}(\epsilon_{E n+1}, \epsilon_{P n+1}, \mathbf{F}_{n+1}) &= \epsilon_{E n+1} + \sqrt{\frac{3}{2}} (\epsilon_{P n+1} - \epsilon_{P n}) - |\text{dev}(\ln \mathbf{V}_{E n+1,n}^{\text{tr}})|, \\ \mathbf{r}_{\epsilon_{P n+1,n}}(\epsilon_{E n+1}, \epsilon_{P n+1}, \mathbf{F}_{n+1}) &= \epsilon_{P n+1} - \epsilon_{P n} - \gamma_0 \left\langle \frac{f_{P n+1,n}}{\sigma_0} \right\rangle^{m_0} t_{n+1,n}. \end{aligned} \quad (1.47)$$

These determine in particular the explicit form

$$\mathbf{K}_n(\boldsymbol{\alpha}_{n+1}, \mathbf{F}_{n+1}) = 3\kappa_0 \text{sph}(\ln \mathbf{V}_{E n}^{\text{tr}}(\mathbf{F}_{n+1})) + 2\mu_0 \epsilon_{E n+1} \text{sgn}(\text{dev}(\ln \mathbf{V}_{E n}^{\text{tr}}(\mathbf{F}_{n+1}))) \quad (1.48)$$

of the algorithmic Kirchhoff stress from (1.20). The system (1.46) can be written in the compact form

$$\mathbf{r}_{\boldsymbol{\alpha}_{n+1,n}}(\boldsymbol{\alpha}_{n+1}, \mathbf{F}_{n+1}) = \mathbf{0}, \quad (1.49)$$

with

$$\boldsymbol{\alpha} := (\epsilon_E, \epsilon_P) \quad (1.50)$$

and

$$r_{\alpha} := (r_{\epsilon_E}, r_{\epsilon_P}). \quad (1.51)$$

For fixed \mathbf{F}_{n+1} and $t_{n+1,n}$, iterative solution of (1.49) yields in the usual fashion α_{n+1} as an implicit function of \mathbf{F}_{n+1} , and so \mathbf{K}_{n+1} as such a function.

The current unknown deformation field ξ_{n+1} satisfying the current boundary conditions and momentum balance is given by solution of

$$m_{n+1,n}(\xi_{n+1}, \alpha_{n+1}, \xi_*) = 0 \quad (1.52)$$

for all ξ_* , with

$$\begin{aligned} m_{n+1,n}(\xi_{n+1}, \alpha_{n+1}, \xi_*) &:= \int_{B_r} \{ \varrho_0 \mathbf{a}_{n+1,n}(\xi_{n+1}) - \det(\nabla_r \xi_{n+1}) \mathbf{l}_{n+1} \} \cdot \xi_* \\ &+ \int_{B_r} \mathbf{K}_n(\alpha_{n+1}, \nabla_r \xi_{n+1}) \cdot \nabla_{n+1} \xi_* \\ &- \int_{\partial B_r} |c_r(\nabla_r \xi_{n+1})| \mathbf{t}_{cn+1} \cdot \xi_* \end{aligned} \quad (1.53)$$

the weak momentum balance functional obtained from the algorithmic form of (1.15). Again, in the context of the current staggered approach, the Lorentz force \mathbf{l}_{n+1} is assumed known and given. Here, the material acceleration² $\mathbf{a}_{n+1,n}(\xi_{n+1}) := \mathbf{a}(\xi_{n+1}, t_{n+1,n}; \xi_n, \dot{\xi}_n, \ddot{\xi}_n)$ is considered algorithmically a function of ξ_{n+1} , $t_{n+1,n}$, and the state at the end $t = t_n$ of the last time step, in the context of, *e.g.*, the Newmark algorithm. In addition, the notations $\nabla_{n+1} \xi_* := (\nabla_r \xi_*) \mathbf{F}_{n+1}^{-1}$ and that $\mathbf{c}_r(\mathbf{F}) := \text{cof}(\mathbf{F}) \mathbf{n}_r$ have been introduced, with \mathbf{n}_r the outward unit normal to the boundary ∂B_r of B_r .

As usual, the finite element approximation to (1.53) in the Lagrangian context is based on the discretization

$$B \approx \bigcup_e B^e \quad (1.54)$$

of B into a finite number of elements B^1, B^2, \dots . In terms of the corresponding finite element approximation

$$\xi_e = \mathbf{H} \mathbf{x}^e \quad (1.55)$$

for the element deformation field ξ_e in terms of the element shape function matrix \mathbf{H} , as well as in terms of the element nodal position vector \mathbf{x}_e , one obtains, as usual, the element representation

$$\mathbf{F}^e(\mathbf{x}^e) := \nabla_r^e \xi_e = (\nabla_r^e \mathbf{H})^s \mathbf{x}^e \quad (1.56)$$

for the deformation gradient, with $(\nabla_r^e \mathbf{H})^s \mathbf{x}_e := \nabla_r^e (\mathbf{H} \mathbf{x}_e)$. In particular, these induce the discretized form

$$m_{n+1,n}(\xi_{n+1}, \alpha_{n+1}, \xi_*) = \sum_e \mathbf{f}_{n+1,n}^e(\mathbf{x}_{n+1}^e, \mathbf{e}_{n+1}^e) \cdot \mathbf{x}_*^e \quad (1.57)$$

²Not to be confused with the vector potential \mathbf{a} .

of the functional in (1.53), with

$$\begin{aligned} & \mathbf{f}_{n+1,n}^e(\mathbf{x}_{n+1}^e, \mathbf{e}_{n+1}^e) \\ & := \int_{B_r^e} \mathbf{H}^T \mathbf{H} \{ \varrho_0 \mathbf{a}_{n+1,n}^e(\mathbf{x}_{n+1}^e) - \det(\mathbf{F}^e(\mathbf{x}_{n+1}^e)) \boldsymbol{\ell}_{n+1}^e \} + (\nabla_{n+1}^e \mathbf{H})^{\text{ST}} \mathbf{K}_{n+1,n}^e(\mathbf{e}_{n+1}^e, \mathbf{F}^e(\mathbf{x}_{n+1}^e)) \\ & - \int_{\partial B_r^e} |\mathbf{c}_r(\mathbf{F}^e(\mathbf{x}_{n+1}^e))| \mathbf{H}^T \mathbf{t}_{cn+1}^e \end{aligned} \quad (1.58)$$

with $\nabla_{n+1}^e \mathbf{H} := (\nabla_r^e \mathbf{H}) \mathbf{F}_{n+1}^{-1}$ and $\boldsymbol{\ell}^e = \mathbf{H} \boldsymbol{\ell}^e$. With the help of the connectivity relations

$$\mathbf{x}^e = \mathbf{I}_x^e \mathbf{x}^s \quad (1.59)$$

between the element and structural nodal positions, (1.57) reduces to

$$m_{n+1,n}(\boldsymbol{\xi}_{n+1}, \boldsymbol{\alpha}_{n+1}, \boldsymbol{\xi}_*) = \mathbf{f}_{n+1,n}^s(\mathbf{x}_{n+1}^s, \mathbf{e}_{n+1}^s) \cdot \mathbf{x}_*^s, \quad (1.60)$$

with

$$\mathbf{f}_{n+1,n}^s(\mathbf{x}_{n+1}^s, \mathbf{e}_{n+1}^s) := \sum_e \mathbf{I}_x^{eT} \mathbf{f}_{n+1,n}^e(\mathbf{I}_x^e \mathbf{x}_{n+1}^s, \mathbf{e}_{n+1}^e). \quad (1.61)$$

Since \mathbf{x}_*^s is arbitrary, (1.52) reduces to the discrete form

$$\mathbf{f}_{n+1,n}^s(\mathbf{x}_{n+1}^s, \mathbf{e}_{n+1}^s) = \mathbf{0} \quad (1.62)$$

in terms of $\mathbf{f}_{n+1,n}^s$. For its iterative solution, we require as usual the algorithmic derivative

$$\partial_{\mathbf{x}_{n+1}^s}^a \mathbf{f}_{n+1,n}^s = \sum_e \mathbf{I}_x^{eT} (\partial_{\mathbf{x}_{n+1}^e}^a \mathbf{f}_{n+1,n}^e) \mathbf{I}_x^e \quad (1.63)$$

of this at fixed $\boldsymbol{\ell}_{n+1}^s$, with

$$\begin{aligned} \partial_{\mathbf{x}_{n+1}^e}^a \mathbf{f}_{n+1,n}^e & := \int_{B_r^e} \mathbf{H}^T \mathbf{H} \{ \varrho_0 (\partial_{\mathbf{x}_{n+1}^e}^a \mathbf{a}_{n+1,n}^e)_{n+1} - \det(\mathbf{F}^e(\mathbf{x}_{n+1}^e)) (\boldsymbol{\ell}_{n+1}^e \otimes \mathbf{I}) (\nabla_{n+1}^e \mathbf{H})^{\text{S}} \} \\ & + \int_{B_r^e} (\nabla_{n+1}^e \mathbf{H})^{\text{ST}} \{ (\partial_{\mathbf{F}_{n+1}}^a \mathbf{K}_n)_{n+1}^e \mathbf{F}_{n+1}^{eT} - \mathbf{K}_{n+1,n}^e \triangle \mathbf{I} \} (\nabla_{n+1}^e \mathbf{H})^{\text{S}} \\ & - \int_{\partial B_r^e} \mathbf{H}^T \mathbf{t}_{cn+1}^e \otimes (\nabla_{n+1}^e \mathbf{H})^{\text{ST}} \{ |\mathbf{c}_r|^{-1} [(\mathbf{c}_r \cdot \mathbf{c}_r) \mathbf{I} - \mathbf{c}_r \otimes \mathbf{c}_r] \}_{n+1}^e \end{aligned} \quad (1.64)$$

via (1.1)₃. Here,

$$(\partial_{\mathbf{F}_{n+1}}^a \mathbf{K}_n) \mathbf{F}_{n+1}^T = (\partial_{\ln \mathbf{V}_{E_{n+1},n}^{\text{tr}}}^a \mathbf{K}_n) (\partial_{\mathbf{F}_{n+1}} \ln \mathbf{V}_{E_n}^{\text{tr}}) \mathbf{F}_{n+1}^T \quad (1.65)$$

represents the ‘‘push-forward’’ to the current algorithmic configuration of the algorithmic derivative of \mathbf{K}_n with respect to \mathbf{F}_{n+1} from (1.48) in terms of the notation

$$\begin{aligned} \partial_{\ln \mathbf{V}_{E_{n+1},n}^{\text{tr}}}^a \mathbf{K}_n & := \partial_{\ln \mathbf{V}_{E_{n+1},n}^{\text{tr}}} \mathbf{K}_n - (\partial_{\boldsymbol{\alpha}_{n+1}} \mathbf{K}_n) (\partial_{\boldsymbol{\alpha}_{n+1}} r_{\boldsymbol{\alpha}_n})^{-1} (\partial_{\ln \mathbf{V}_{E_{n+1},n}^{\text{tr}}} r_{\boldsymbol{\alpha}_n}) \\ & = 3\kappa_0 \text{sph} + 2\mu_0 \frac{\epsilon_{E_{n+1}}}{|\epsilon_{E_{n+1},n}^{\text{tr}}|} (\mathbf{I} \square \mathbf{I} - \mathbf{N}_{E_{n+1},n}^{\text{tr}} \otimes \mathbf{N}_{E_{n+1},n}^{\text{tr}}) \text{dev} \\ & + 2\mu_0 (\partial_{\boldsymbol{\alpha}_{n+1}} r_{\boldsymbol{\alpha}_n})_{\epsilon_E}^{-1} (\mathbf{N}_{E_{n+1},n}^{\text{tr}} \otimes \mathbf{N}_{E_{n+1},n}^{\text{tr}}) \text{dev}. \end{aligned} \quad (1.66)$$

Here, $\partial_{\alpha_{n+1}} r_{\alpha n}$ represents the Jacobian of the system (1.49), $(\partial_{\alpha_{n+1}} r_{\alpha n})_{\epsilon_E \epsilon_E}^{-1}$ the upper left diagonal element of its inverse $(\partial_{\alpha} r_{\alpha n})^{-1}$, $\epsilon_{En+1,n}^{\text{tr}} := |\text{dev}(\ln \mathbf{V}_{En+1,n}^{\text{tr}})|$ and $\mathbf{N}_{En+1,n}^{\text{tr}} := \text{sgn}(\text{dev}(\ln \mathbf{V}_{En+1,n}^{\text{tr}}))$. Note that

$$(\partial_{\mathbf{F}_{n+1}} \ln \mathbf{V}_{En}^{\text{tr}}) \mathbf{F}^{\text{T}} = \frac{1}{2} (D \ln)(\mathbf{V}_{En+1,n}^{\text{tr}}) (\mathbf{I} \square \mathbf{B}_{En+1,n}^{\text{tr}} + \mathbf{B}_{En+1,n}^{\text{tr}} \triangle \mathbf{I}) \quad (1.67)$$

follows from (1.1)_{2,3} and (1.46)₁. As usual, the Fréchet derivative $D \ln$ of the logarithmic mapping \ln on second-order symmetric Euclidean tensors is calculated with the help of the functional calculus (*e.g.*, Šilhavý, 1997, §1.2.5).

In the context of the finite element method, the Eulerian-based implementation of the electromagnetic model is based as usual on the spatial discretization

$$R \approx \bigcup_e Re \quad (1.68)$$

of R into a finite number of elements. The corresponding approximation

$$\mathbf{a}_e = \mathbf{N} \mathbf{a}^e \quad (1.69)$$

for the vector potential field at the element level \mathbf{a}_e in terms of the element shape function matrix \mathbf{N} analogous to (1.55) in the mechanical case results in the axisymmetric case in element representation

$$\nabla_s^e \mathbf{a}_e = (\nabla_s^e \mathbf{N})^s \mathbf{a}^e \quad (1.70)$$

for the corresponding gradient analogous to (1.56). In the more general 3-dimensional case in which \mathbf{a} experiences jump discontinuities, the element formulation would have to be generalized, *e.g.*, to Nédélec elements (Nédélec, 1980, 1986) or least-squares-based approaches (Jiang et al., 1996). On this basis, one obtains the spatially-discretized form

$$\sum_e (\mathbf{A}^e \mathbf{a}^e + \mathbf{B}^e \dot{\mathbf{a}}^e) \cdot \mathbf{a}_*^e = \sum_e \mathbf{c}^e \cdot \mathbf{a}_*^e \quad (1.71)$$

of (1.41), with

$$\begin{aligned} \mathbf{A}^e &:= \int_{Re} (\nabla_s^e \mathbf{N})^{\text{ST}} (\nabla_s^e \mathbf{N})^s, \\ \mathbf{B}^e &:= \kappa_{\text{EM}}^{-1} \int_{Re} \mathbf{N}^{\text{T}} \mathbf{N} + \kappa_{\text{EM}}^{-1} \int_{W_{ck} \cap Re} c_k \left(\mathbf{N}^{\text{T}} \mathbf{e}_\varphi \otimes \int_{A_{ck}} \mathbf{N}^{\text{T}} \mathbf{n}_k \right), \end{aligned} \quad (1.72)$$

as well as

$$\mathbf{c}^e := \int_{W_{ck} \cap Re} c_k \kappa_{\text{EM}}^{-1} \sigma_{\text{EM}}^{-1} I \mathbf{N}^{\text{T}} \mathbf{e}_\varphi. \quad (1.73)$$

Using the connectivity relation

$$\mathbf{a}^e = \mathbf{I}_a^e \mathbf{a}^s \quad (1.74)$$

between the element and structural nodal vector potential values, the arbitrariness of \mathbf{a}_*^e leads to the structural form

$$\mathbf{A}^s \mathbf{a}^s + \mathbf{B}^s \dot{\mathbf{a}}^s = \mathbf{c}^s \quad (1.75)$$

of (1.71), with

$$\mathbf{A}^s = \sum_e \mathbf{I}_a^{eT} \mathbf{A}^e \mathbf{I}_a^e, \quad \mathbf{B}^s = \sum_e \mathbf{I}_a^{eT} \mathbf{B}^e \mathbf{I}_a^e, \quad \mathbf{c}^s = \sum_e \mathbf{I}_a^{eT} \mathbf{c}^e, \quad (1.76)$$

formally analogous to (1.61). Integration of (1.75) via the generalized trapezoidal rule over the interval $[t_n, t_{n+1}]$ yields the system

$$\begin{bmatrix} \mathbf{A}^s & \mathbf{B}_{n+1}^s \\ \mathbf{I} & -\alpha t_{n+1,n} \mathbf{I} \end{bmatrix} \begin{bmatrix} \mathbf{a}_{n+1}^s \\ \dot{\mathbf{a}}_{n+1}^s \end{bmatrix} = \begin{bmatrix} \mathbf{c}_{n+1}^s \\ \mathbf{a}_n^s + (1 - \alpha) t_{n+1,n} \dot{\mathbf{a}}_n^s \end{bmatrix} \quad (1.77)$$

to solve for \mathbf{a}_{n+1}^s and $\dot{\mathbf{a}}_{n+1}^s$, in the context of the current staggered approach with fixed \mathbf{x}_{n+1}^s . In contrast to (1.62) for \mathbf{x}_{n+1}^s , note that this last relation can be solved *explicitly* for these quantities. Here, the parameter $0 \leq \alpha \leq 1$ controls the amount of artificial damping exerted on the discrete system. For $\alpha = 1$ (maximal damping), the method coincides with backward-Euler integration, while $\alpha = 1/2$ (no damping) yields the more accurate trapezoidal rule exhibiting an accuracy of $O(\Delta t^2)$ for a maximal time step size $\Delta t \rightarrow 0$ (Hughes, 1987). Nevertheless, to switch from the most accurate value $\alpha = 1/2$ to a value $\alpha > 1/2$ at the beginning of the simulation and after a specified computation time may filter out non-physical oscillations entering by the coupling mechanism.

Note that (1.75) reduces to a time independent linear equation for those degrees of freedom that lie outside the tool coil or the workpiece due to $\kappa_{EM}^{-1} = 0$ there. These degrees of freedom depend only indirectly on the time by their coupling to those degrees of freedom lying in areas with $\kappa_{EM}^{-1} > 0$ (*i.e.*, the tool coil or the workpiece). As in the mechanical case, all spatially-discretized integrals are evaluated in the standard fashion via Gauss quadrature. Particularly, in the axisymmetric situation, the computation of the integrals reduces to a two dimensional quadrature, after cylindrical coordinates have been introduced and the (trivial) azimuthal integration has been performed. In terms of efficiency, the non-local relations, expressed in the integral over A_{ck} in (1.72), linking all degrees of freedom within the same coil winding, should be handled with some care. It is recommended to start with a standard assembly of a sparse mass matrix and to incorporate the additional couplings afterwards. One possibility is to introduce an additional degree of freedom for each coil winding and to assign the total current I_{n+1} flowing through this winding at time t_{n+1} to it. The resulting matrix deviates from a standard sparse matrix only by N columns and rows, where N denotes the number of coil windings. In the numerical examples reported on below, another technique has been applied: After the application of a standard mass matrix in $(1.77)_2$, a second matrix is applied, projecting on the subspace defined by the additional couplings. Such a factorization of the matrix \mathbf{B}_{n+1}^s can easily be realized by a modification of the matrix vector multiplication in the employed iterative solvers (see below). Consequently, the sparse structure of the matrix need not to be distorted. Whether this method is more effective has yet to be established.

In summary, since we are neglecting temperature effects here, and since $\text{curl}_s \mathbf{a} \times \mathbf{v}$ is negligible and has been neglected in the above algorithmic formulation, the simplified form (1.42) of the Lorentz force represents the only coupling between the electromagnetic and mechanical fields in the mechanical part of the model. Likewise, because $\text{curl}_s \mathbf{a} \times \mathbf{v}$ is negligible, the current (deformed) shape of the workpiece in R , which determines the spatial distribution of σ_{EM}

in R appearing in (1.77) via (1.72), represents the only coupling between the mechanical and electromagnetic fields in the electromagnetic part of the model. In this framework, the combined model is solved in an iterative staggered fashion using a two-mesh Lagrangian-Eulerian approach. To discuss this iterative staggered scheme, assume again that the initial boundary value problem and internal variable evolution relations have been solved up to the discrete time $t = t_n$, such that \mathbf{x}_n^s and \mathbf{a}_n^s , together with their temporal derivatives, as well as the corresponding internal variables, are all known. On this basis, we have the following algorithm:

1. Initialize the iteration by setting $\mathbf{x}_{n+1}^{s(k)} = \mathbf{x}_n^s$, $\dot{\mathbf{x}}_{n+1}^{s(k)} = \dot{\mathbf{x}}_n^s$ and $\ddot{\mathbf{x}}_{n+1}^{s(k)} = \ddot{\mathbf{x}}_n^s$ for $k = 1$.
2. Given I_{n+1} in the tool coil, compute $\mathbf{a}_{n+1}^{s(k)}$ and $\dot{\mathbf{a}}_{n+1}^{s(k)}$ on the Eulerian mesh via (1.77). As indicated, this depends on where one is in the system, *i.e.*, whether or not the point in question is in the workpiece, tool coil, or air. To this end, the assembly routine determines whether the nodal points of the Eulerian mesh lie in air, in the tool coil, or in the workpiece, and so the current spatial distribution of σ_{EM} .
3. Having then $\mathbf{x}_{n+1}^{s(k)}$, $\mathbf{a}_{n+1}^{s(k)}$ and $\dot{\mathbf{a}}_{n+1}^{s(k)}$, the corresponding Lorentz force $\mathbf{l}_{n+1}^{(k)}$ is obtained on the basis of (1.42) via data transfer and projection from the Eulerian to the embedded Lagrangian mesh for the workpiece. Then, the system consisting of (1.49) and (1.62) is solved iteratively at fixed $\mathbf{l}_{n+1}^{(k)}$ to obtain $\mathbf{x}_{n+1}^{s(k+1)}$, $\dot{\mathbf{x}}_{n+1}^{s(k+1)}$, $\ddot{\mathbf{x}}_{n+1}^{s(k+1)}$, and the corresponding internal variables.
4. Steps 1.-3. are repeated for $k = 2, \dots$ until convergence is obtained, yielding \mathbf{x}_{n+1}^s , \mathbf{a}_{n+1}^s , and the internal variables in the entire structure.

In all simulations, k rarely exceeded 3 (*e.g.*, if both the velocity of the structure is quite high and the flux density of the decaying electromagnetic field inside the structure is still significant; see Section 1.6) and in any case was less than 8. The algorithms for the electromagnetic and mechanical parts of the current coupled-field model have been implemented at the element level into the finite element program SOFAR³. In particular, this has been done for the current 4-node axisymmetric case as well as for the 8-node three-dimensional case. Elsewhere, a stabilized 8-node shell-element formulation (Reese et al., 2005) for the current model has also been developed and is currently being implemented.

1.5 Data transfer and numerical convergence behavior

In order to investigate the effect of data transfer between the mechanical and electromagnetic parts of the staggered algorithm on the numerical solution, consider the electromagnetic forming of a round sheet metal workpiece with the thickness of 1.2 mm and radius of 52 mm consisting of the aluminum alloy AC120. As shown in Figure 1.1, the work piece and tool coil are idealized as being axisymmetric, with the tool coil lying 0.6 mm below the workpiece. The sheet metal is clamped down at a radius of 34.75 mm by the die holder. For simplicity, the corresponding contact is idealized here by simply fixing the upper and lower surface nodes of the plate mesh in the region of the die holder.

³Small Object-oriented Finite-element library for Application and Research

Application of the model from Section 1.3 and its algorithmic form in Section 1.4 requires the specification of the isotropic hardening behavior of AC120. As a first approximation, the quasi-static uniaxial test data of Badelt et al. (2003) were used for this purpose. Identification of the semi-empirical form

$$\psi_p(\epsilon_p) = c_1 (\epsilon_p + c_2)^{c_3} + c_4 \ln(1 + c_5 \epsilon_p) \quad (1.78)$$

of the dependence of the inelastic part ψ_p of the free energy density on ϵ_p related to energy storage in the material due to isotropic hardening based on these data yields $\sigma_{F0} = 116.0$ MPa, $c_1 = -12.39$ MPa, $c_2 = 0.001$, $c_3 = 0.0697$, $c_4 = 80.31$ MPa and $c_5 = 36.59$ for AC120. In particular, this form determines the quasi-static contribution $\sigma_Y = -\zeta_p$ to the flow stress from (1.21). Further, values of $\sigma_0 = 90$ MPa, $\gamma_0 = 10^4$ s⁻¹ and $m_0 = 5$ for aluminum relevant for strain-rates of $\geq 10^3$ s⁻¹ were taken from the literature (Jones, 1997). Lastly, the elastic behavior of AC120 is characterized by the values $\lambda = 39404$ MPa and $\mu = 26269$ MPa for the Lamé constants at room temperature.

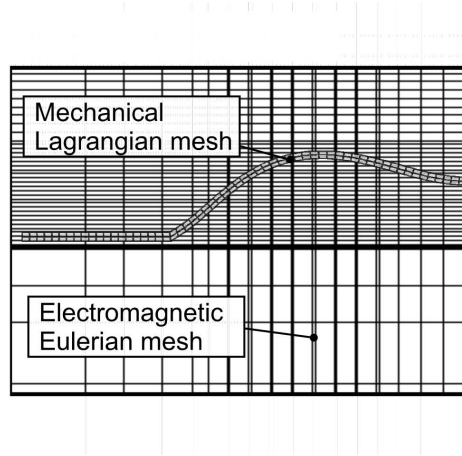


Figure 1.3: Finite element discretization of the coupled problem consisting of a fixed Eulerian mesh for the electromagnetic system and deforming Lagrangian mesh for the sheet metal workpiece.

The finite element meshes used for the mechanical part of the simulation (see Figure 1.3) are based on four-node bilinear elements. The discretization of the electromagnetic part of the coupled problem is also based on such elements with edges parallel and perpendicular to the z axis. As mentioned above, this is in contrast to the three-dimensional case in which discontinuities arise in the electromagnetic fields, requiring more sophisticated numerical methods. In order to improve efficiency, the design of both meshes are adapted from the start to the expected deformation and electromagnetic field development. In particular, the element density in the mechanical mesh is larger near the contact point with the die holder as well as at the center of symmetry where bending and deformation are most extreme. Analogously, in the electromagnetic case, the region traversed by the moving mechanical mesh as well as the gap between the tool and work piece are more finely discretized than the remaining regions (see Figure 1.3). This is not only necessary due to the large gradients in the vector potential arising here, but also to minimize additional errors due to inaccurate local approximation in elements with internal diffusivity jumps and inaccurate transfer of the Lorentz forces. More on this in what follows.

Consider in particular the transfer of Lorentz forces from the electromagnetic to the mechanical mesh of the workpiece. In particular, this is based on (1.42). To begin, this involves identifying the current positions of element nodes from the mechanical mesh in the electromagnetic mesh. As implied in Figure 1.4, using these, the value of \mathbf{l} is calculated at these positions from the nodal values of \mathbf{a}^e and $\dot{\mathbf{a}}^e$ in the electromagnetic mesh (note that $\nabla_s \chi = 0$ in the workpiece) via interpolation using the element shape functions. These interpolated values are then passed to the mechanical mesh for use in the solution of (1.58).

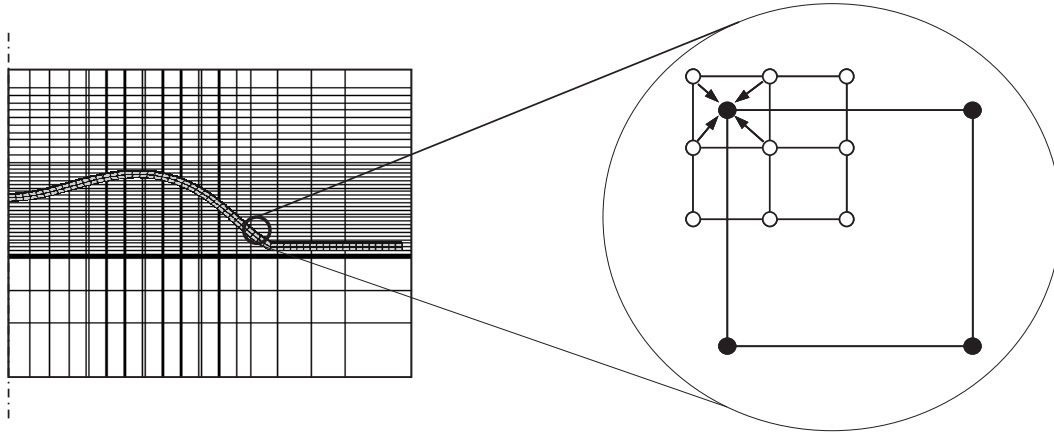


Figure 1.4: Data transfer from the (white-node) electromagnetic mesh to the (black-node) mechanical mesh at the element level.

Going in the other direction, the distribution of κ_{EM} (or in the numerical case of κ_{EM}^{-1}) has to be transferred from the mechanical to the electromagnetic mesh. This is done directly by determining whether the Gauss points of the current electromagnetic mesh lie in the workpiece, tool, die or air and setting the value of κ_{EM} accordingly. The simplicity of both of these is that they require no remeshing. The question of whether or not such an approach is really more effective than remeshing (in particular the electromagnetic mesh) is a matter of current research. A clear disadvantage of current approach is that jumps of the diffusivity within elements in electromagnetic mesh reduce the local approximation order (consistency) of the finite element discretization. Nevertheless, the resulting loss of accuracy is limited due to the fact that only a small percentage of small elements is affected.

To get a better understanding of the simulation results of the fully coupled simulation as described in the proceeding section, consider first the purely mechanical case. In particular, attention is focused on idealized body-force-based loading analogous to the Lorentz force such as those shown in Figure 1.10.

Here, in the time interval from 0 to 20 μs , a body force density \mathbf{f} with non-trivial z -component f_z is imposed on all points of the structure between $r = 9$ mm and $r = 35$ mm. After 20 μs , this force is turned off. Spatially, this force is assumed to be constant in the radial direction and to vary in the axial direction as depicted in Figure 1.10. In both the linear and exponential cases, the mean value of f_z is 10 N mm^{-3} over the workpiece thickness. Since they both have the same mean value, we should obtain the same mechanical simulation results. On this basis,

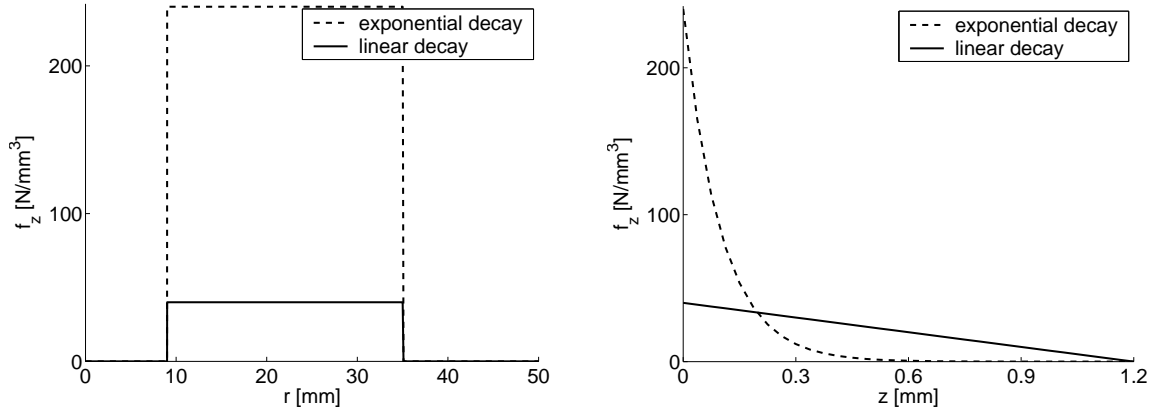


Figure 1.5: Exponential and linear idealized Lorentz body force density distributions (z -component) in the circular sheet metal plate used in the investigation of convergence behavior and the data transfer approach used in the current work (see text for details). Left: Distributions in the radial direction at $z = 0$. Right: Distributions in the vertical direction at $r = 0$.

a series of finite element simulations with different meshes were performed for both volume force distributions. All meshes employed were of the type described above (see also Figure 1.3) and hierarchically refined. Figure 1.6 shows the forming stages of the plate at various instances for the linear volume force distribution and a mesh with 480 elements in four layers.

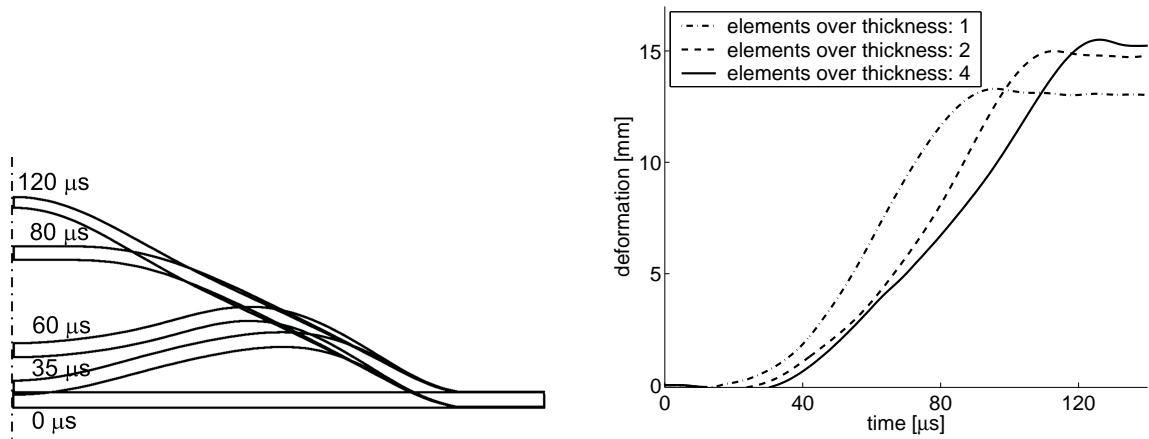


Figure 1.6: Forming stages (left) and solution convergence behavior (right) as a function of the number of elements over the thickness for the case of the linear body force density distribution shown in Figure 1.5. Initially, the displacement due to acceleration is large in the coarse meshes due to their higher rigidity; as time proceeds, however, this tendency reverses as deformation begins to dominate, at which point typical convergence behavior (*i.e.*, increased deformation with number of elements) is observed. See text for details.

As shown on the left in this figure, such body force distributions lead to an initial acceleration of the middle of the plate. In later stages, the plate center is dragged along and accelerated by the induced inertial force, resulting in the cap-like form at the end of the forming process after approximately 120 μ s. The convergence behavior of the solution as a function of time for the linear distribution is shown on the right in Figure 1.6. Here, the vertical displacement of the workpiece at its center ($r = 0$) for three different meshes is depicted. Initially, coarser

meshes exhibit more (rigid-body-like) displacement since finer meshes accelerate less rigidly under dynamic loading. With time, however, deformation in the structure begins to dominate and this trend reverses, resulting in the usual convergence behavior at the end of the process, *i.e.*, finer meshes are “softer.”

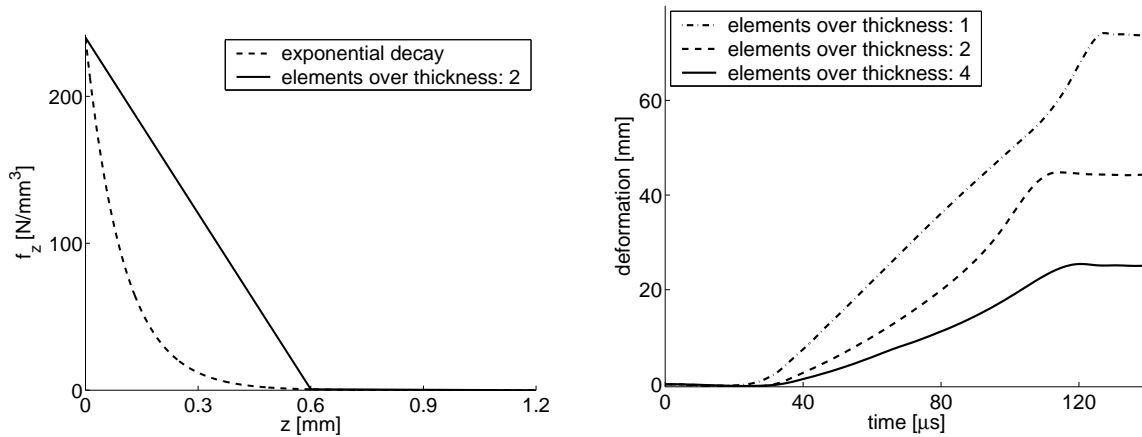


Figure 1.7: Overestimation of exponential body force density distribution (left) due to bilinear interpolation for the case of two elements over the thickness of the plate. Because of this, the convergence behavior (right) is counterintuitive and contrary to the previous example with a linear distribution.

As shown in Figure 1.7, in the case of the exponential distribution (using the same bilinear interpolation scheme) and two elements over the thickness, the reverse tendency in the convergence behavior is observed, *i.e.*, mesh refinement results in decreased deformation. This results from the data transfer process as based on bilinear interpolation. Indeed, in this case, two elements over the thickness are insufficient to represent the exponential form and lead to an overestimate of the Lorentz force in the Gauss points of the mechanical mesh, and hence more deformation. This overestimation of the force in coarse meshes can be reduced mapping the values of the Lorentz force from the electromagnetic mesh directly onto the Gauss points of the mechanical mesh. In any case, using a sufficient number of elements over the thickness alleviates the problem.

1.6 Fully coupled simulation

Now, the fully coupled elastoviscoplastic electromagnetic multifield algorithm developed in Section 1.2 - Section 1.3 is applied to the case of electromagnetic sheet metal forming. Initial results of coupled simulations of electromagnetic sheet metal forming using an elastoplastic version of the model (neglecting the rate dependency) have been presented by Kleiner et al. (2004). The forming of aluminum tubes with an elastoviscoplastic mechanical model is considered by Svendsen and Chanda (2003). As described in Section 1.5, the experimental configuration consists of a tool, a workpiece and a die holder as depicted in Figure 1.1. The workpiece consists of the aluminum alloy AC120, while the tool coil consists of copper. The tool coil has a height of 11.5 mm and consists of 9 windings, each of which is 2.5 mm wide with 0.3 mm distance to the neighbored windings. The radius of the inner area, which is free of windings, amounts

to 9 mm. As mentioned before, the coefficients in the semi-empirical form (1.78) have been fitted by experimental data to model the dependence of the inelastic part ψ_p of the free energy density on ϵ_p related to energy storage in the material due to isotropic hardening, yielding the coefficients stated in Section 1.5. The same values for the elastic and viscoplastic parameters as in Section 1.5 have been employed. Simulation results to be discussed in what follows have been carried out for converged solutions involving mechanical meshes of 360 elements and 4 elements over the thickness.

Deformation of the workpiece is driven here by a pulsed current (see Figure 1.8) that induces a magnetic field around the tool coil which is strongly influenced by the movement of the workpiece.

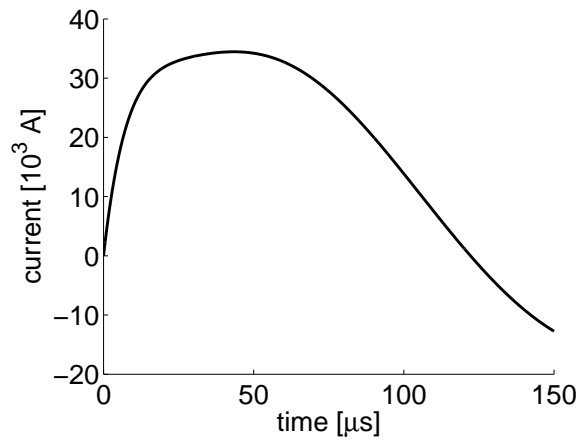


Figure 1.8: Measured input current used in the electromagnetic forming simulation.

The corresponding simulated magnetic field is shown in Figure 1.9. In particular, the distribution of the radial component of the magnetic flux density at 20 μs (left) and 80 μs (right) during forming is shown. Note that by virtue of (1.42), this component generates the dominating axial component of the force vector acting on the structure. In the dark areas, flux densities of about 11 Tesla are achieved, decreasing down to about 1 Tesla in the surrounding area. As can be seen, after 80 μs , the magnetic flux density and so the Lorentz force have decayed away, such that further plate deformation is solely driven by inertial forces.

Figure 1.10 shows the volume force density distribution in vertical direction at $t = 10\mu s$ computed from the field computation (the radial component of the volume force density is in general several orders smaller than the vertical one and is therefore not examined here).

The diagram on the left hand side of Figure 1.10 shows the Lorentz force (density) distribution in the radial direction at intervals of $\Delta z = 0.2$ mm, and that on the right-hand side shows the vertical force distribution at $\Delta r = 5$ mm. The location of the tool coil and its windings is clearly mirrored in the radial force distribution. On the basis of the non-linear parabolic character of the electromagnetic part of the coupled-field model (*i.e.*, (1.4) and (1.42)₁), the expected exponential decay of the body force in the direction of the thickness of the workpiece is evident.

Forming stages of the plate at various instances and the corresponding accumulated inelastic strain are shown in Figure 1.11.

Initially, the part of the sheet metal lying directly over the tool coil is subject to large induced

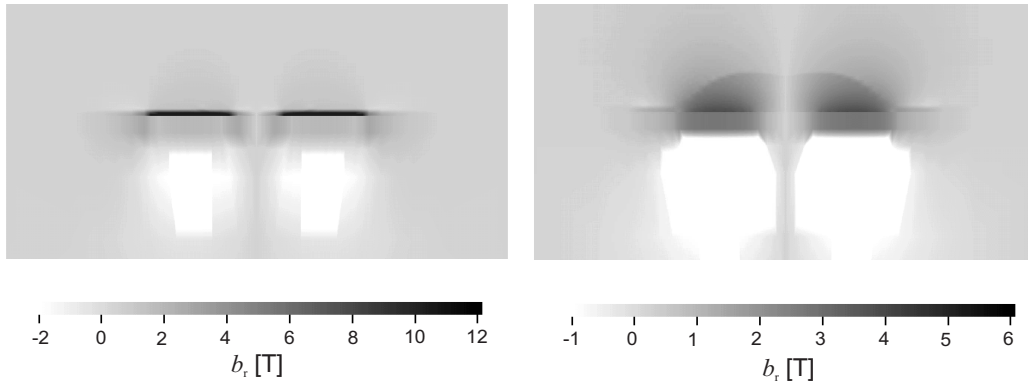


Figure 1.9: Radial component of the magnetic flux density at $20 \mu\text{s}$ (left) and at $80 \mu\text{s}$ (right) inducing the Lorentz force driving the forming. As the sheet metal moves away from the tool coil, the magnetic field diffuses into the region left vacant by the sheet-metal plate, resulting in a decrease in the intensity of the magnetic flux and thus of the Lorentz force.

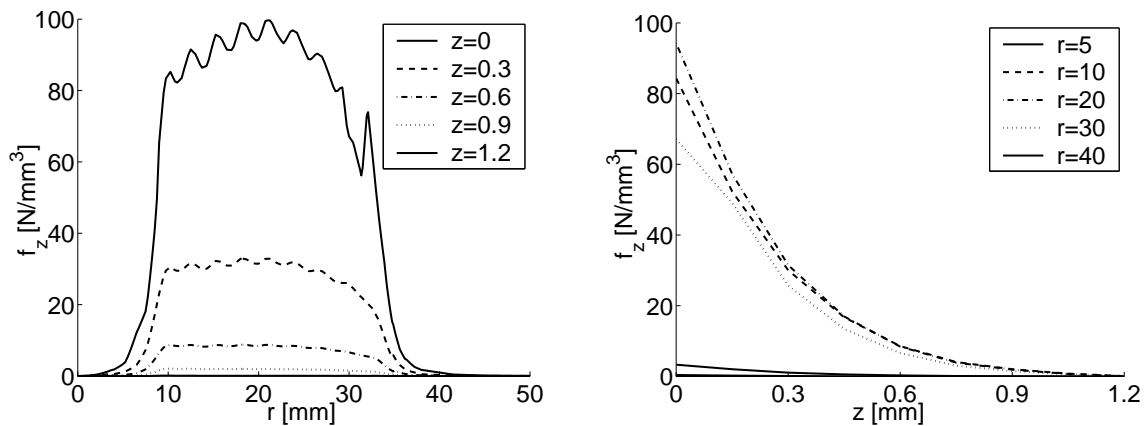


Figure 1.10: Simulated z -component of the Lorentz force density distribution at $10 \mu\text{s}$. Left: Distribution in radial direction depicted at different heights z . Right: Distribution in vertical direction depicted for different radial positions r .

Lorentz forces and begins to accelerate. As forming proceeds, this part pulls the center of the plate along with it. Forming in this part of the plate is then due to the corresponding inertial forces. These induce the maximum accumulated inelastic strain in the structure at the top of the cap as shown. A detailed investigation of the development of strain and stress in the structure is the subject of work in progress.

1.7 Discussion

To begin, consider the influence of numerical errors as well as modeling simplifications on the simulation results. In addition to the usual finite element discretization errors, there are several additional sources for numerical errors in the described coupled algorithm, which, however, tend to zero with increasing mesh refinement. As discussed above, for example, the data transfer process is a source of such error, in particular with respect to the Lorentz force. Secondly, since

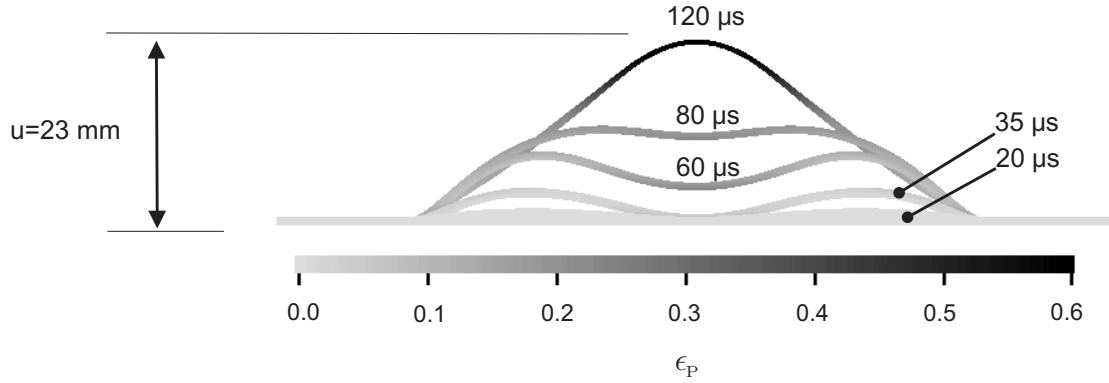


Figure 1.11: Forming stages of the sheet metal plate as a function of time. The shading represents the development of the accumulated inelastic deformation ϵ_p . See text for details.

no matching of elements of the mechanical and of the electromagnetic meshes is enforced, the local finite element approximation (consistency) becomes worse in those elements of the electromagnetic mesh, that are partially covered by the structure. Consequently, the Lorentz forces computed in these elements are less accurate. Of course, this error is reduced by an increasing level of mesh refinement. The resulting loss of accuracy is compensated by a gain of efficiency, since the chosen arrangement allows for simple mesh generation in both subsystems. Particularly, no remeshing or mesh deformation on the electromagnetic side is necessary, despite the movement of the structure. To judge whether the decreased numerical expenses justify the accompanying loss of accuracy, a further implementation is currently being developed in which the mechanical and the electromagnetic simulation are still carried out in different meshes, but all elements of the mechanical mesh have an identical counterpart in the electromagnetic mesh. This allows a direct element-to-element transfer of Lorentz forces without the need of searching the active element in the electromagnetic mesh and without an additional error due to reduced consistency. However, such an implementation requires either remeshing or deformation of the electromagnetic mesh in every step of the Newton iteration of the mechanical structure due to its movement. In this vein, the method of Liao (*e.g.*, Cai et al., 2004, and references therein cited) is an effective way to redistribute mesh points of a given grid preserving its topology. Such methods allow to adapt the electromagnetic mesh to the moving structure without remeshing and thus seem to be a good choice for the type of coupled problems discussed here.

Compared to the numerical errors reported on above, the physical model simplifications seem to be less significant, at least at those stages of mesh refinement that have been examined, although a final verification of this assumption has not been performed. To estimate the influence of the convective terms which have been neglected, test simulations accounting for $\text{curl}_s \mathbf{a} \times \mathbf{v}$ in the simulation of the electromagnetic field have been carried out. The computed axial deformation of the structure during the first 60 μs did not deviate from the results neglecting this term more than 1%. This is less than the influence of the numerical errors described above at the levels of mesh refinement considered here. Thus, neglecting $\text{curl}_s \mathbf{a} \times \mathbf{v}$ is justified, and useful also from the point of view that it destroys the symmetry of the equation system to be solved. In particular, this would mean that the iterative preconditioned conjugate gradient solver used to solve (1.77) could no longer be used. For the test computations, a BICGSTAB solver has been employed (*e.g.*, Meister, 1999). Beyond convection, the solution seems to be

quite insensitive with respect to changes in the shape and position of the outer boundary, where homogeneous Dirichlet boundary conditions are assumed. The influence of the approximation of the tool coil by axisymmetric tori as described in Section 1.5 on the simulation results has not yet been investigated and represents work in progress. Similar, the influence of approximating the die holder simply by fixing the relevant degrees of freedom is currently being investigated.

In further work in progress, methods for rigorous a posteriori error estimation are being implemented. The size of the numerical errors can be estimated and minimized by a higher level of discretization if necessary. Moreover, a posteriori error estimators localize areas with a high contribution to the overall error. The information obtained can be used to design optimal meshes which maximize the accuracy for given computational resources. A rigorous control of the numerical error is particularly important with regard to model identification.

Chapter 2

On the effect of current pulses on the material behavior during electromagnetic metal forming*

Abstract – Electromagnetic sheet metal forming (EMF) is an example of a high-speed forming process driven by the dynamics of a coupled electromagnetic-mechanical system. Basic physical processes involved in EMF such as, e.g., inelastic and hardening behavior, or inertia, have been considered in previous works (Stiemer et al., 2006a; Svendsen and Chanda, 2005). The purpose of the current work is the investigation of temperature development during EMF and a possible reduction in the yield stress due to electric currents. While thermoelastic and viscoplastic effects are well understood (Lemaitre and Chaboche, 1990), the possible influence of electric currents on dislocation motion, generally referred to as the electro-plastic effect (Conrad and Sprecher, 1989; Varma and Cornwell, 1979), is still an unresolved issue. It is shown here that such an effect is at most of second-order and can most likely be safely neglected in the modeling and simulation of industrial EMF.

2.1 Introduction

In electromagnetic metal forming (EMF), a strong pulsed magnetic field generated in the tool coil adjacent to an electrically conducting work piece induces eddy currents in the work piece which interact with the magnetic field, inducing in turn a Lorentz force in the workpiece which drives the forming process. The entire forming process lasts in the order of 100-300 μs and achieves strain-rates of up to 10^4 s^{-1} . Compared to other forming methods, it offers increased formability for certain kinds of materials, reduction in wrinkling, the possibility of combining forming and assembly operations, reduced tool-making costs *etc.*. An example of the basic experimental setup for the case of sheet metal forming is shown in Figure 2.1. The time-dependent current in the tool coil shown on the right depicts the pulsed nature of this current and so that of the resulting magnetic field.

The further development of EMF as an industrial forming process depends in particular on the availability and use of reliable simulation tools for the corresponding coupled multifield problem. In particular, these must be able to deal with high strain rates $\dot{\epsilon} \geq 10^3 \text{ s}^{-1}$, large current densities $|\mathbf{j}| \geq 10^4 \text{ A/mm}^2$, and strong magnetic fields $|\mathbf{b}| \geq 10^0 \text{ T}$. In this context we examine possible effects in the material such as a reduction in yield stress due to temperature and strong electrical currents.

In the literature, the electroplastic (EP) effect has been postulated to contribute to the behavior of metals under combined mechanical and electromagnetic loading (Molotskii, 2000; Troitskii, 1969). The idea here is that an interaction between the electric current and dislocations may affect the hardening behavior and in particular the yield stress. There has been a consid-

*Unger et al. (2006b)

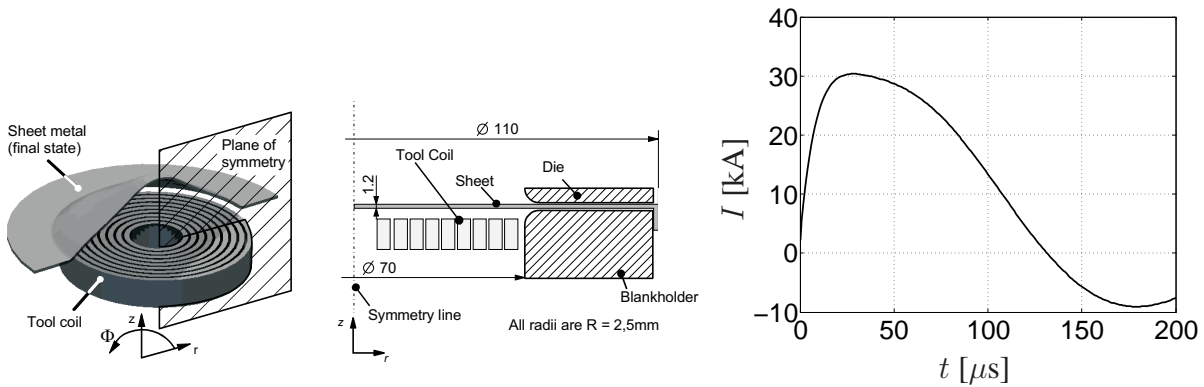


Figure 2.1: Electromagnetic sheet metal forming setup.

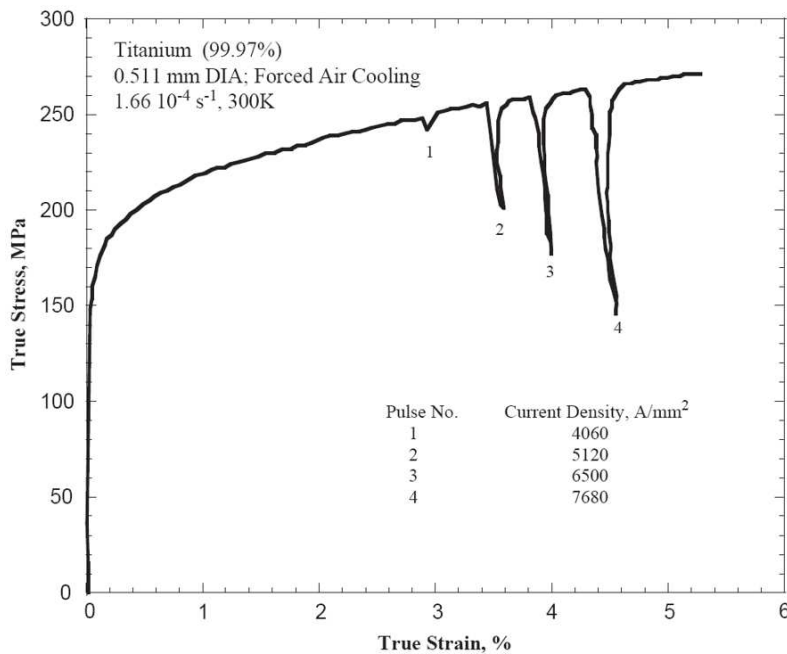


Figure 2.2: Experimental results of Okazaki et al. (1979). During tensile testing of a circular bar, an imposed current density results in stress drops. The current density achieved maximum values of from 4060 to 7680 A/mm^2 and lasted for about 60 μs . For pulse no. 2 tensile stress decreased to about 70% of its original value.

erable debate regarding the significance of such an effect in polycrystalline metals (Goldman et al., 1980).

Figure 2.2 shows the current density and tensile test response of an experiment performed by Okazaki et al. (1979). In their experiment a titanium bar with diameter $d = 0.511 \text{ mm}$ was subjected to simple tension tests. As shown in Figure 2.2, the discharge of a capacitor bank at given times during this loading resulted in an sudden increase of the current density and in a time-correlated drop in the yield stress. Okazaki et al. (1979) showed that each of these current-density “jumps” resulted in a temperature rise of about 12.2 K to 99.9 K depending on the imposed current density. Since a temperature rise of this order of magnitude implies a drop of the yield stress of about 0.4% and 5.0%, authors favoring the electroplastic effect concluded that the observed drops are due to an interaction of electron movements and the

moving dislocations. Recently, Bilyk et al. (2005) showed that the introduction of an EP effect is not necessary to explain the stress drops shown in Figure 2.2. They concluded that the stress drops can be modeled by an accurate modeling of viscoplastic rate effects during pulsing. The work presented here confirms the view that the stress drops can be explained with the help of conventional effects. However, it is concluded that mainly thermal expansion leads to the observed stress drops.

2.2 Thermoelastic, viscoplastic model including Joule heating

The multifield material model used in the current work represents a special case of the general continuum thermodynamic formulation of such models from Svendsen and Chanda (2005) to the formulation of models for electromagnetic thermoelastic, viscoplastic solids. In particular, this work provides a framework for the treatment of EMF processes also accounting for the interaction between the electromagnetic and thermomechanical effects at *large* deformations. The case of the simple tension tests mentioned above is somewhat simpler than that of sheet metal forming shown in Figure 2.1 in the sense that the deformation is significantly smaller. Following Svendsen and Chanda (2005), in our case the magnetic field can be modeled as diffusive over the length- and timescales of interest. In this case Maxwell's equations and Ohm's law yield the diffusive field relation

$$\mathbf{0} = \partial \mathbf{b} - \kappa_{\text{EM}} \nabla^2 \mathbf{b} \quad (2.1)$$

for the spatial magnetic flux density \mathbf{b} . Here, $\kappa_{\text{EM}} := \sigma_{\text{EM}}^{-1} \mu_{\text{EM}}^{-1}$ represents the magnetic diffusivity, μ_{EM} the magnetic permeability, and σ_{EM} the electric permittivity. (Note that all material and modeling data can be found in tables 2.1 and 2.2). In particular, on a timescale τ , κ_{EM} implies a skin depth (*i.e.*, penetration depth of the magnetic field into the material) of $\ell_{\text{EM}} = \sqrt{\kappa_{\text{EM}} \tau}$. As indicated in Table 2.1, for the case of titanium, the skin depth is significantly larger than the radius of the “bar” (*i.e.*, a wire here). Consequently, the current density is constant throughout the whole cross section. For a long wire (*i.e.*, $l/r_0 \gg 1$), (2.1) can be solved to obtain

$$(b_r, b_\varphi, b_z)(r) = (0, \frac{\sigma_{\text{EM}} I r}{2\pi r_0^2}, 0) \quad (2.2)$$

in cylindrical coordinates (r, φ, z) (Jackson, 1975). Here, I represents the imposed current and r_0 the radius of the wire. In turn, this implies a constant current density

$$(j_r, j_\varphi, j_z)(r) = (0, 0, I/\pi r_0^2) \quad (2.3)$$

within the cross-section of the wire.

Consider next the energy balance and temperature evolution in the bar. Here, the characteristic length scale is determined as usual by the thermal diffusivity $\kappa_{\text{TM}} := k_r / \varrho_r c_r$, where k_r represents the thermal conductivity, c_r the specific heat capacity, and ϱ_r the mass density at reference temperature θ_r . As usual on a timescale τ , significant thermal conduction will take place on the length scale $\ell_{\text{TM}} = \sqrt{\kappa_{\text{TM}} \tau}$. Since this length scale is much smaller than the width of the wire (see Table 2.1), we are justified in assuming adiabatic conditions over the timescale of the pulses ($\leq 100 \mu\text{s}$). Over longer timescales, of course, this is not the case. Finally, in contrast

to EMF we neglect the radially acting Lorentz force for two reasons; firstly its magnitude is significantly smaller than the applied mechanical loads (Bilyk et al., 2005) and secondly the structural response is minimal due to the present setup geometry.

	ℓ_{EM}/r_0	ℓ_{TM}/r_0
Al	5.8×10^0	4.0×10^{-1}
Ti	2.2×10^1	1.2×10^{-1}
Assumption	uniform current density	adiabatic during pulsing

Table 2.1: Scaling relations for electromagnetic diffusion and thermal diffusion.

With these simplifications the temperature is homogeneous and treated as an internal variable (see (2.10)₃ below). Consequently, the deformation $\boldsymbol{\xi}$ is the only thermomechanical field given as usual by the weak form

$$\int_{B_r} \varrho_r \ddot{\boldsymbol{\xi}} \cdot \boldsymbol{\xi}_* + \mathbf{K} \cdot \nabla \boldsymbol{\xi}_* = 0 \quad (2.4)$$

for pure kinematic boundary conditions with respect to the reference configuration B_r for all corresponding test fields $\boldsymbol{\xi}_*$. Here, \mathbf{K} represents the Kirchhoff stress. As usual, this latter variable, along with the internal variables, is given by a material model. For simplicity, attention is restricted here to the case of (isotropic) thermoelastoviscoplasticity with isotropic hardening. Further, in the case of metals, we have small elastic strain. The relevant internal variables are then the elastic left logarithmic stretch $\ln \mathbf{V}_E$ and the accumulated inelastic strain ϵ_P . On this basis the thermodynamic formulation being pursued here is based on specific model relations for the referential free energy density ψ as well as on the evolution relations for the internal variables. In particular, assuming for simplicity that the elastic behavior is not affected by inelastic processes such as damage, the split

$$\psi(\theta, \ln \mathbf{V}_E, \epsilon_P) = \psi_E(\theta, \ln \mathbf{V}_E) + \psi_P(\theta, \epsilon_P) \quad (2.5)$$

of the free energy into thermoelastic and inelastic parts is justified (*e.g.*, Svendsen, 2001). Assuming for simplicity that the specific heat capacity c_r is constant (Rosakis et al., 2000), and exploiting the condition of small elastic strain, one obtains the thermoelastic neo-Hooke form

$$\begin{aligned} \psi_E(\theta, \ln \mathbf{V}_E) &= \frac{1}{2} \lambda_r (\mathbf{I} \cdot \ln \mathbf{V}_E)^2 - (3\lambda_r + 2\mu_r) \alpha_r (\theta - \theta_r) (\mathbf{I} \cdot \ln \mathbf{V}_E) + \frac{1}{2} \mu_r (\ln \mathbf{V}_E \cdot \ln \mathbf{V}_E) \\ &+ \varrho_r c_r [\theta - \theta_r - \theta \ln(\theta/\theta_r)] \end{aligned} \quad (2.6)$$

for ψ_E , where λ_r and μ_r represent Lamé's constants and α_r the thermal heat expansion coefficient. The inelastic part ψ_P is determined empirically with the help of experimental data, as discussed in the next section. Consider next the evolution of the internal variables and the inelastic behavior. In the metallic polycrystalline materials of interest at low-to-moderate homologous temperature, inelastic deformation processes are controlled predominantly by the activation of dislocation glide on glide systems (*e.g.*, Teodosiu (1997)), even at higher strain rates. As such, higher homologous temperatures are required for other mechanisms such as dislocation climb or even dynamic recrystallization to activate. Resistance to dislocation glide arises due to extended

obstacles generating longer-range stress fields related in the phenomenological context to hardening behavior. In addition, such resistance is caused by short-range local obstacles which can be overcome by thermal fluctuation under the action of local effective stress, represented in the current phenomenological context by $|\text{dev}(\mathbf{K})| + \varsigma_P - \sigma_{F0}(\theta)$, where

$$-\varsigma_P := \psi_{,\epsilon_P} \quad (2.7)$$

represents the static contribution to the flow stress (in shear). On this basis

$$f_P := \frac{|\text{dev}(\mathbf{K})| + \varsigma_P}{\sigma_P} \quad (2.8)$$

represents an activation function or non-dimensional overstress in the current rate-dependent context. Here, σ_P represents the dynamic drag contribution to the effective flow stress in the system. On this basis a power-law approximation of the more exact transition-state-based micromechanical relations for the kinetics of dislocation glide leads to the power-law form

$$\phi = \frac{\gamma_P \sigma_P}{m_P + 1} \langle f_P \rangle^{m_P + 1} \quad (2.9)$$

upon which the evolution of the internal variables is based. Here, γ_P represents a characteristic strain rate, $\langle x \rangle := \frac{1}{2}(x + |x|)$ the MaCauley bracket, and m_P the strain rate exponent. In general, these will be functions of temperature and rate of deformation; here, we treat them for simplicity as constants. This potential determines as usual the forms

$$\begin{aligned} \ln^* \mathbf{V}_E &= -\phi_{,\mathbf{K}} &= -\text{sgn}(\text{dev}(\mathbf{K})) \dot{\epsilon}_P \quad (\mathbf{K} \neq \mathbf{0}), \\ \dot{\epsilon}_P &= \phi_{,\varsigma_P} &= \gamma_P \langle f_P \rangle^{m_P} \quad (f_P > 0), \\ \dot{\theta} &= \varrho_r^{-1} c_r^{-1} \{ \omega_r + \sigma_{EM}^{-1} \det(\mathbf{F}) \mathbf{j} \cdot \mathbf{j} \} \quad , \end{aligned} \quad (2.10)$$

for the evolution of the internal variables. Here, ω_r represents the rate of mechanical heating and $\sigma_{EM}^{-1} \det(\mathbf{F}) \mathbf{j} \cdot \mathbf{j}$ the electromotive power.

Now, for the case of incompressible material behavior, we assume that the isotropic forms of the viscoplastic parameters γ_P , σ_P and m_P are independent of the trace $\mathbf{I} \cdot \mathbf{D}$ of the rate of deformation. In this case, the thermoelastic form

$$\mathbf{K} = \psi_{,\ln \mathbf{V}_E} = \{ \lambda_r (\mathbf{I} \cdot \ln \mathbf{V}_E) - (3\lambda_r + 2\mu_r) \alpha_r (\theta - \theta_r) \} \mathbf{I} + \mu_r \ln \mathbf{V}_E \quad (2.11)$$

for the Kirchhoff stress holds from (2.6). In addition,

$$\omega_r = \gamma_P \sigma_P \langle f_P \rangle^{m_P + 1} - (3\lambda_r + 2\mu_r) \alpha_r \theta \overline{\ln \det(\mathbf{F})} \quad (2.12)$$

then follows for the referential form of the mechanical heating rate.

This completes the basic model formulation. The detailed algorithmic formulation and numerical implementation of the finite element model has been presented partially in Stiemer et al. (2006a). In the present context the material model of this approach was extended by the above evolution equations. In particular, note that the time step size for tensile test simulation has to be chosen according to the particular timescale where changes of internal variables are to be expected. During current pulses, the time step size was chosen to be 10^{-6} s. Otherwise, much larger step sizes in the order of 10^0 s were chosen. The time integration of the velocity and acceleration fields was carried out using Newmark's method. Numerical damping was applied during pulsing and afterwards in order to avoid numerical oscillations.

2.3 Application to metal bars subject to pulsed currents and simple tension

In this section, the current model is applied to the tensile tests with pulsed electric currents. To this end, we specify here the semi-analytical form

$$-\zeta_P = \psi_{,\epsilon_P} = \sigma_{F0} \left(1 + \frac{\epsilon_P}{\epsilon_0} \right)^n - \sigma_{F0} \quad (2.13)$$

for the strain hardening due to energy storage, with

$$\sigma_{F0} = \sigma_{F0r} (1 - \omega_{TM}(\theta - \theta_r)) \quad (2.14)$$

for the initial static flow stress, σ_{F0r} being the initial flow stress at reference temperature θ_r . The parameter ω_{TM} mediates the reduction of the initial flow stress due to an increase of the temperature. Table 2.2 summarizes the material parameters characterizing the inelastic material behavior. For titanium, the parameters in (2.13) were obtained from Bilyk et al. (2005). In particular, ω_{TM} , γ_P , σ_P and m_P were fitted to the model data also provided in Bilyk et al. (2005). For aluminum, the tensile test data were used for the strain hardening fit. Table 2.3 lists the remaining material parameter values needed.

	σ_{F0r} MPa	ϵ_0 -	n -	ω_{TM} K^{-1}	γ_P s^{-1}	σ_P MPa	m_P -
Al	3.5×10^1	2.0×10^{-3}	1.9×10^{-1}	1.4×10^{-3}	1.0×10^{-4}	5.0×10^0	4.0×10^0
Ti	1.7×10^2	2.0×10^{-3}	1.5×10^{-1}	8.7×10^{-4}	1.0×10^{-4}	4.0×10^0	4.0×10^0

Table 2.2: Inelastic parameters.

	λ_r MPa	μ_r MPa	α_r K^{-1}	ϱ_r $kg\ m^{-3}$	c_r $m\ s^{-2}\ K^{-1}$	k_r $J\ s^{-1}\ m^{-1}\ K^{-1}$
Al	5.0×10^4	2.6×10^4	2.3×10^{-5}	2.7×10^3	9.2×10^8	2.4×10^2
Ti	8.5×10^4	4.4×10^4	8.6×10^{-6}	4.5×10^3	5.2×10^8	2.2×10^1

Table 2.3: Thermoelastic parameters.

Consider next the results in Figure 2.3 for the case of a current pulse applied to a titanium bar undergoing simple tension in the z -direction. At the time of the pulse ($t = 200$ s), Joule heating results in a temperature rise from 301 K to 363 K within 60 μs . The slight temperature rise of 3 K before the pulse is due to mechanical dissipation. In the left part of Figure 2.3, the change in the zz -component of the Cauchy stress $\mathbf{T} = J^{-1}\mathbf{K}$ is shown as a function of time. As can be seen, the current pulse results in a reduction of this component. In addition, both the rate-dependent and rate-independent cases show this change. In contrast to the work of Bilyk et al. (2005), we claim that not the rate effect, but rather the thermal expansion effect, is crucial to correctly model the observed stress drop.

To delve into this in more detail, consider the results depicted in Figure 2.4 for the rate of the accumulated inelastic strain ϵ_P as well as the rate of $\epsilon_E = |\text{dev}(\ln \mathbf{V}_E)|$, representing the norm

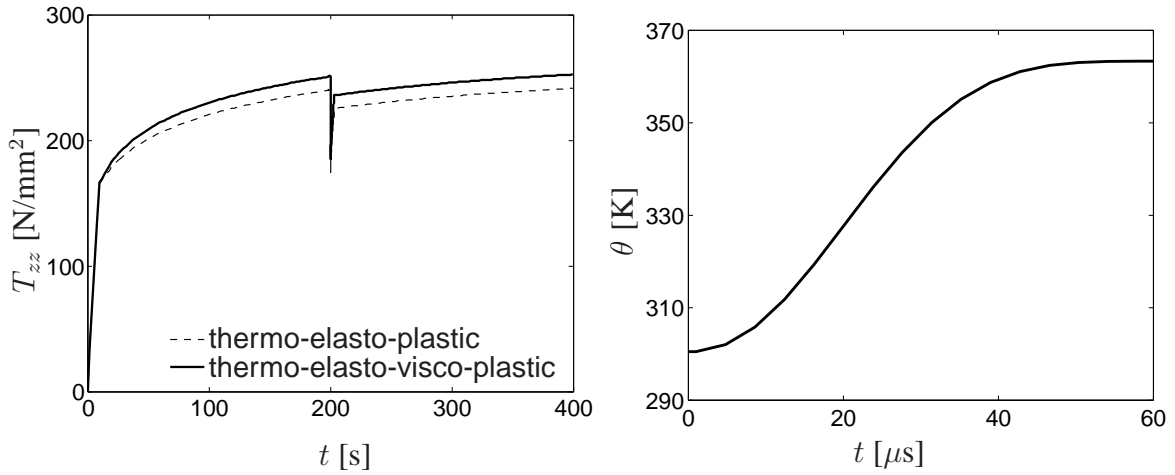


Figure 2.3: Current pulse applied to a titanium bar undergoing simple tension. Left: Development of the zz -component of the Cauchy stress simulated with a thermoelastic, viscoplastic model (rate-dependent: solid line) and a thermoelastic, elastoplastic model (rate-independent: dashed line). Right: Temperature rise from Joule heating during the current pulse starting at $t = 200$ s.

of the deviatoric part of the left logarithmic stretch tensor. As soon as the temperature rises, the spherical part $\text{sph}(\ln \mathbf{V}_E)$ of $\ln \mathbf{V}_E$ increases (see (2.11)). Conversely, the deviatoric part and hence ϵ_E decreases. Accordingly, since $|\text{dev}(\mathbf{K})| = 2\mu\epsilon_E$, the activation stress (2.9) decreases and elastic unloading can be observed. The drop of $\dot{\epsilon}_p$ to zero takes place within 60 μ s (see Figure 2.4 right). Afterwards for several seconds the tensile testing machine continues to load the specimen in the elastic domain until the inelastic flow is reactivated. As shown, in this range, $\dot{\epsilon}_p = 0$.

Such testing has also been carried out for technically pure aluminum (*e.g.*, Al99,5 or AA1000

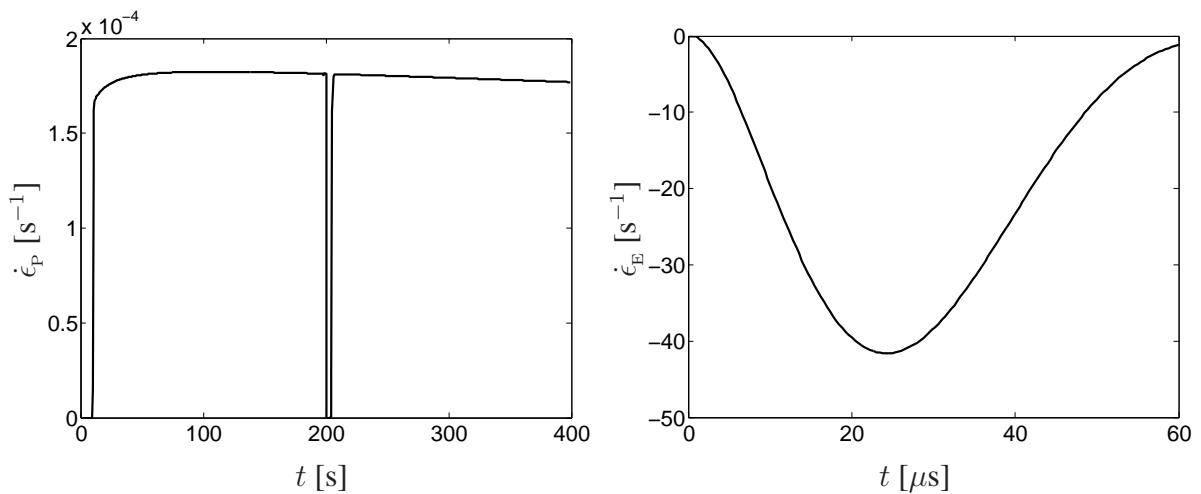


Figure 2.4: Rate of change of the accumulated inelastic strain as a function of time during pulsing. Left: The current pulse at 200 s forces the stress state below the activation threshold, resulting in $\dot{\epsilon}_p = 0$. Right: Variation in time of $\dot{\epsilon}_E$ starting at $t = 200$ s (note the difference of the timescale).

series). As all experimental conditions are the same as for the tests with titanium, the particular material characteristics of aluminum are the reason for a smaller stress drop. In particular, for the same geometry and imposed current I , \mathbf{j} as given by (2.3) is the same for both materials. Since the contribution to $\dot{\theta}$ from Joule heating is given by $\det(\mathbf{F}) \mathbf{j} \cdot \mathbf{j} / (\rho_r c_r \sigma_{EM})$ from (2.10)₃, any difference between the two materials is due to the magnitude of $\rho_r c_r \sigma_{EM}$. The parameter values in Table 2.3 imply that the heat capacity $\rho_r c_r$ per unit volume is almost the same for aluminum and titanium. On the other hand, $\sigma_{EM}^{Al} = 3.8 \times 10^7 \text{ Ohm}^{-1} \text{ m}^{-1}$ and $\sigma_{EM}^{Ti} = 2.6 \times 10^6 \text{ Ohm}^{-1} \text{ m}^{-1}$ are substantially different. Consequently, since $\sigma_{EM}^{Al} \gg \sigma_{EM}^{Ti}$, it is clear why the temperature rise in aluminum (6 K) is much smaller than that in titanium (50 K). Via the thermoelastic coupling in (2.11), then, this difference in temperature increase is reflected in the respective stress drops, *i.e.*, 60 MPa for titanium and 6 MPa for aluminum (Figure 2.5).

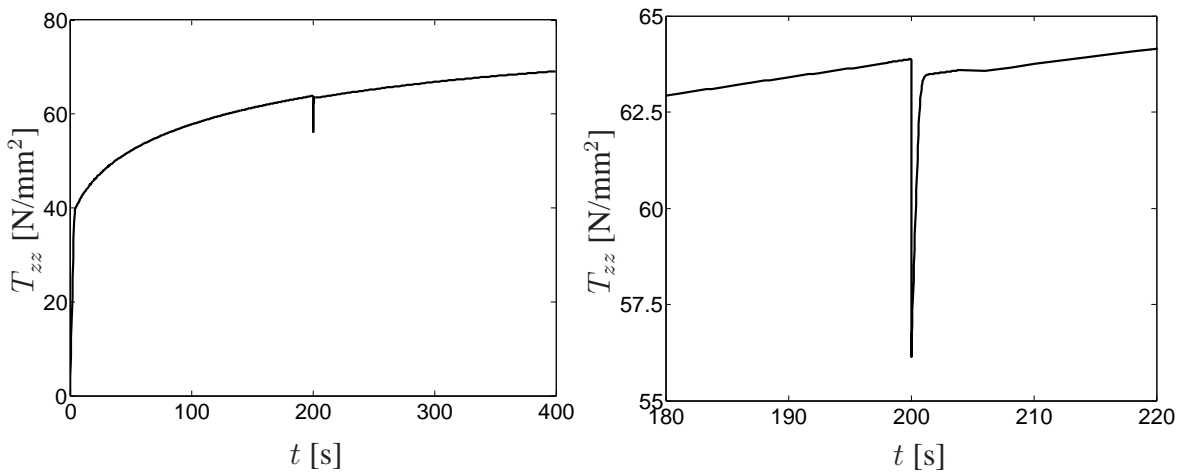


Figure 2.5: Simulated stress drop for aluminum due to Joule heating during simple tension. Left: Change of T_{zz} with time. Right: Blow-up of the stress drop region in time.

2.4 Conclusions

For the typical timescales imposed current densities and materials generally relevant for EMF processes load drops during tensile testing are observed. For titanium and aluminum it was shown that the magnitude of the load drops can be modeled without postulating a direct interaction between electron and dislocation movement. The modeling of experimental results indicate that "conventional" effects allow for a sufficiently accurate rendering of the experimental observations and such an interaction can be considered of second order in particular for industrial applications of EMF. Of all the effects considered, the adiabatic thermo-elastic expansion leads to the observed load drops; visco-plastic rate effects and thermal softening are notable but secondary.

Chapter 3

Inverse error propagation and model identification for coupled dynamic problems with application to electromagnetic metal forming*

Abstract – The purpose of this work is the development and application of strategies to identify material model parameters for metals at high strain-rates using data obtained from high-speed electromagnetic metal forming. To this end, a staggered algorithm for the finite element based numerical solution of the coupled electromagnetic-mechanical boundary value problem has been developed based on mixed Eulerian-Lagrangian multigrid methods. On this basis, the parameter determination together with a sensitivity study, correlation analysis and error estimation are carried out. After verifying the validity of this approach using synthetic data sets, it is applied to the identification of material parameters using experimental results from electromagnetic tube forming.

3.1 Introduction

Inverse problems are present in many fields of science and engineering. Classes of such inverse problems include, *e.g.*, seismic problems in geophysics (Scales et al., 2001; Snieder and Trampert, 1991), crack and defect detection (Tanaka and Dulikravich, 2001), process design (Kompalka et al., 2007; Tortorelli and Michaleris, 1994; Zabaras et al., 2003), or, as in the current work, material model parameter identification or material model calibration from experimental data. The aim here is to determine the set of material parameters from experimental data. In the current work, these data are obtained at high strain-rates via electromagnetic metal forming (EMF). In this case, strain-rates of up to 10^4 s^{-1} are achieved. Given the low-to-moderate homologous temperatures achieved during EMF, experimental evidence summarized in Jones (1997), as well as considerations regarding dislocation dynamics (*e.g.*, Kocks and Mecking, 2003; Teodosiu, 1997), imply that the material behavior in this case is rate-dependent. Following Svendsen and Chanda (2005), micromechanical and thermodynamic considerations for metals under such conditions imply that a semi-phenomenological Perzyna-type thermoelastic, viscoplastic constitutive model is appropriate. In particular, using the electromagnetic forming data, the material parameters in this model which control the rate-dependence are to be determined.

Classical experimental methods for the determination of dynamical material behavior include for example the split Hopkinson bar or Kolsky bar, gas gun, electromagnetic ring expansion and drop tower (*e.g.*, El-Magd and Abouridouane, 2005; Field et al., 1994; Gilat and Clifton, 1985; Gray, 2000; Klepaczko and Malinowski, 1978; Kolsky, 1949; Meyers, 1994). These gen-

*Unger et al. (2007a)

erally utilize specimen geometries designed to induce a homogeneous deformation state and deformation rate. More recent approaches based on numerical solutions of the boundary-value problem can also deal with experimental results involving non-homogeneous deformation of the specimen (*e.g.*, Mahnken, 2000; Scheday, 2003; Springmann and Kuna, 2005). For example, Kajberg et al. (2004) use data from high speed photography of impact tests to identify viscoplastic material parameters via a finite element analysis of the inhomogeneous deformation of the specimen. Similarly, the deformation field obtained during EMF is inhomogeneous, so that the corresponding material model identification involves the finite element simulation of the specimen. Such an identification procedure always involves the solution of an inverse problem. Often, this identification does not take measurement errors into account (*e.g.*, Gelin and Ghouati, 1994; Kleinermann and Ponthot, 2003, and previously cited authors). Those investigations that do are usually based on homogeneous deformation results. For example, Bruhns and Anding (1999) quantified correlations of parameters and estimate variances for identified material parameters. In addition, Harth et al. (2004) identified parameters for AINSI SS316 stainless steel and estimated their variances by generating synthetic data sets mimicing experimental data. In the current work, the finite element inverse analysis is extended using such methods common to statistical model identification and applied to identify material parameters by means of data obtained via EMF. This approach is then verified with the help of additional data from homogeneous tests.

The paper begins (Section 3.2) with a brief summary of the mechanical material model for electromagnetic forming and its numerical implementation. The latter is based on a finite element based staggered multigrid approach in which the electromagnetic field relations are solved on an Eulerian, and the mechanical field relations on a Lagrangian mesh. In the model, the full coupling between the deformation and magnetic fields is taken into account. Next, we review the formulation of the corresponding inverse problem (Section 3.3). This includes error, sensitivity and correlation analysis. The approach here exploits the staggered structure of the numerical solution algorithm as well as the fact that the model parameters are only weakly sensitive to variations in the electromagnetic fields. In any case, the parameters are identified on the basis of the fully coupled model and simulation. To validate the approach, it is applied to synthetic data sets generated with assumed parameter values for the case of aluminum tube forming. After first carrying out a sensitivity and correlation analysis (Section 3.4), the viscoplastic material parameters are identified using these data sets along with error estimates (Section 3.5). In the last part of the work, the approach is applied (Section 3.6) to actual experimental data of Brosius (2005) for the aluminium alloy AA 6060.

3.2 Coupled model and algorithmic formulation

The matter of interest in this section is the modeling of the dynamic interaction of strong electromagnetic fields with metallic solids resulting in their deformation. There exist a number of modeling approaches for coupled magneto-mechanical problems. Some focus on specific geometries, like in the case of ring forming (Gourdin, 1989; Triantafyllidis and Waldenmyer, 2004). Others are applied to arbitrary geometries but are restricted to small deformations (*e.g.*, Schinnerl et al., 2002). For the case of interest here, *i.e.*, large-deformation inelastic processes,

very little work exists (El-Azab et al., 2003; Fenton and Daehn, 1998). The model to be summarized in this section represents a special case of the general continuum thermodynamic formulation (Svendsen and Chanda, 2005) in which a strong magnetic field induces electric currents in thermoelastic, viscoplastic electric conductors generating Lorentz forces resulting in large inelastic deformations.

Here the system consists of a *fixed* region $R \subset E$ of Euclidean point space E containing one or more solid bodies moving through it as well as the surrounding air. In the case of EMF, for example, these bodies include the workpiece (*e.g.*, sheet metal) and tool coil consisting of technically pure copper (see Figure 3.1 and Figure 3.2). As such, R contains the reference (*e.g.*,

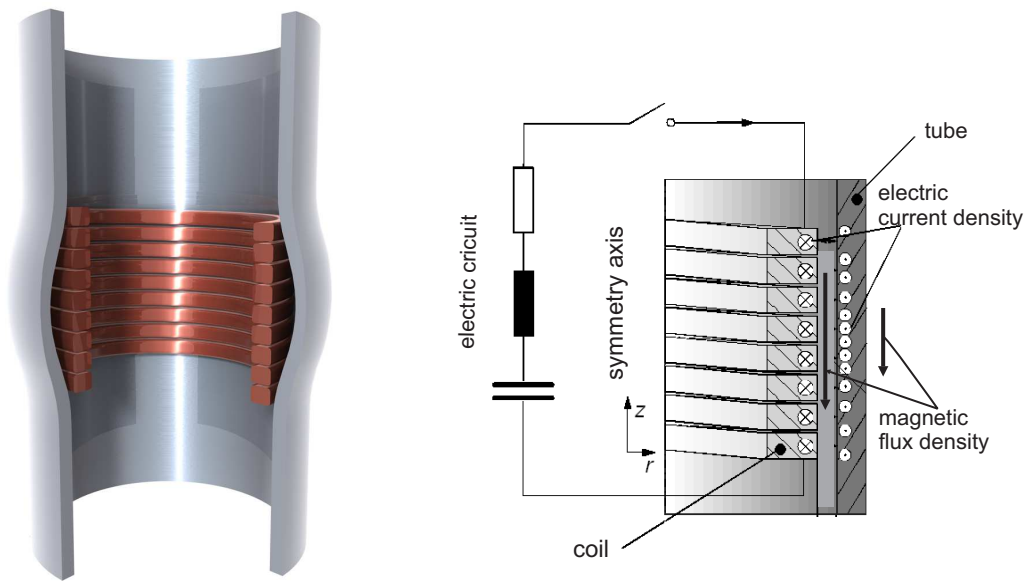


Figure 3.1: Electromagnetic (tube) forming. Left: 3D illustration of the workpiece (tube) and tool coil (copper windings). Right: Schematic axisymmetric 2D representation depicting the electric circuit, tool coil and workpiece as well as the magnetic flux and current densities in the workpiece and tool coil.

initial) $B_r \subset R$ and current $B_c \subset R$ configurations of any of these bodies. They are modeled here as electromagnetic, mechanical continua characterized by a time dependent deformation field ξ together with the additional degrees of freedom representing the electromagnetic fields to be introduced in what follows. Whereas the time dependent electromagnetic fields are defined on the entire region R , *i.e.*, also in the air surrounding stationary or moving material bodies, the deformation field ξ and all kinematic fields derived from it, are logically restricted to the configurations of deforming and moving bodies. Since the relevant electromagnetic frequencies for the engineering structures of interest (*i.e.*, less than 10 MHz) correspond to electromagnetic wavelengths which are much larger than these structures, note that the wave character of the electromagnetic fields is insignificant, and can be neglected. In effect, this corresponds to the so-called quasistatic approximation (Moon, 1980, §2.2 and §2.8). For simplicity, any thermo-electric effects, as well as any magnetostriction (*i.e.*, the Hall effect), are also neglected here. This is reasonable for conductors like aluminum or copper at room temperature and “weak” magnetic fields. In addition, although there is a temperature increase during electromagnetic forming due to mechanical dissipation and Joule heating (*e.g.*, Svendsen and Chanda, 2005),

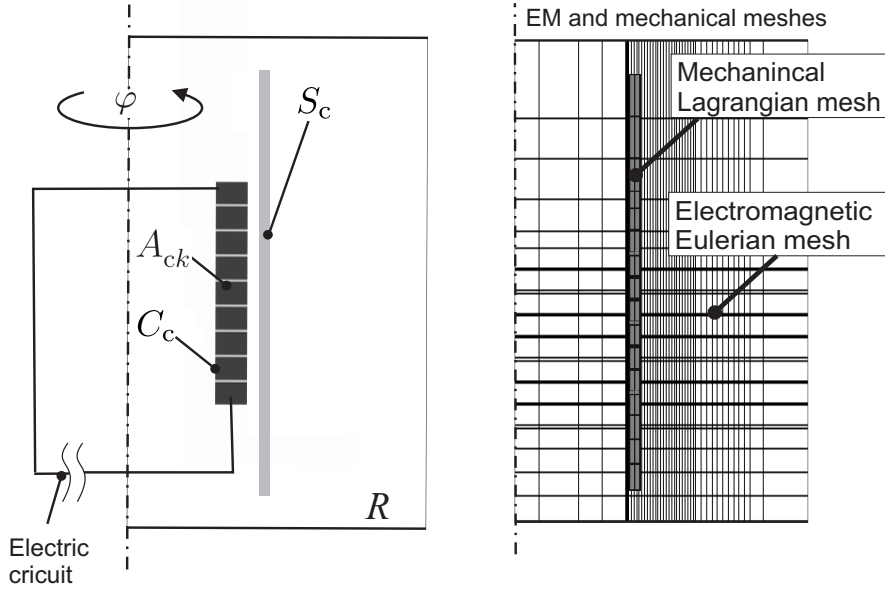


Figure 3.2: Electromagnetic and mechanical domains and meshes for the coupled finite element simulation. Here, S_c represents the current configuration of the workpiece, C_c that of the tool coil, A_{ck} the cross section of the k^{th} torus, and R the region of space containing workpiece, tool coil and the surrounding air with boundary ∂R . Shown on the right is the multigrid configuration for the coupled simulation consisting of fixed Eulerian electromagnetic and moving Lagrangian mechanical meshes.

this increase is small (20-50 K). Consequently, for simplicity we assume isothermal conditions in this work. Under these conditions, field relations for the electromagnetic vector and scalar potentials can be derived following Svendsen and Chanda (2005). The magnetic field can be modeled as diffusive here over the length- and timescales of interest. In this case, Maxwell's equations and the Coulomb gauge condition $\text{div}_s \mathbf{a} = 0$ yield the diffusive field relation

$$\partial \mathbf{a} + \nabla_s \chi - \kappa_{\text{EM}} \text{div}_s(\nabla_s \mathbf{a}) = \mathbf{0} \quad (3.1)$$

for the vector potential \mathbf{a} together with

$$\text{div}_s(\nabla_s \chi) = \nabla_s^2 \chi = 0 \quad (3.2)$$

for the scalar potential χ , where κ_{EM} represents the magnetic diffusivity. As usual, \mathbf{a} and χ determine the magnetic flux via $\mathbf{b} = \text{curl}_s \mathbf{a}$ and the electric field via $-\mathbf{e} = \partial \mathbf{a} + \nabla_s \chi$. Given that the electromagnetic fields vary on a timescale much shorter than that of the mechanical fields, the convective term $\mathbf{b} \times \mathbf{v}$ in the electromotive intensity $\boldsymbol{\epsilon} = \mathbf{e} + \mathbf{v} \times \mathbf{b}$ is much smaller than \mathbf{e} and hence $-\boldsymbol{\epsilon} \approx \partial \mathbf{a} + \nabla_s \chi$ (e.g., Stiemer et al., 2006a). For more details, the reader is referred to this latter work.

Consider next the modeling of the tool coil. During tube expansion, it can be treated as stationary. Consequently, the current C_c and reference $C_{c,r}$ configurations of this coil coincide and are fixed (see Figure 3.2, left). As depicted in Figure 3.1, the tool coil has the shape of a helix consisting of n windings with constant inner and outer radii. The cross section of any winding at any azimuthal angle φ is always identical. The tool coil consists of copper embedded

in a resin matrix whose electromagnetic properties are close to those of a vacuum. Although the tool coil is not perfectly axisymmetric, it can be approximated as such with sufficient accuracy due to the small pitch of the helix. In this case, the n windings of the copper helix are replaced by n tori W_{ck} , $k = 1, \dots, n$, possessing the same cross section (Figure 3.2, below). These are connected in series via cuts in each torus at an azimuthal angle of $\varphi = 0$. The cross section of each W_{ck} , $k = 1, \dots, n - 1$, at $\varphi = 2\pi$ is then treated differently from that at $\varphi = 0$ and identified with that at $\varphi = 0$ of the next winding W_{ck+1} . In particular, this means that the electrostatic potential is continuous across the transition from one torus to another. This simplification also results in the triggering current having only an azimuthal component. Since the n windings are connected in series, the (measurable) total current $I = I(t)$ (see Figure 3.4 below) flowing through a cross section A_{ck} of any winding W_{ck} at an arbitrary azimuthal angle is always the same. Outside the tool coil, *i.e.*, in the resin matrix, or in the moving workpiece S_c , or in the air around the tool coil and workpiece, the boundary and transition conditions for the electromagnetic fields at material interfaces imply that χ is constant there and so $\nabla_s \chi$ vanishes. Note that χ and \mathbf{a} may be reasonably approximated by zero at the boundary of the region R containing the tool coil, the workpiece, and the surrounding air. Solving then equation (3.2) explicitly in every W_{ck} subject to the usual boundary conditions between a perfect conductor (copper) and an insulating medium (resin), one obtains the result

$$-\nabla_s \chi = \begin{cases} 0 & \text{in } R \setminus (C_c \cup S_c) \\ 0 & \text{in } S_c \\ c \left\{ \sigma_{\text{EM}}^{-1} I + \int_{A_{ck}} \mathbf{n}_k \cdot \partial \mathbf{a} \right\} \mathbf{e}_\varphi & \text{in } W_{ck} \end{cases} \quad (3.3)$$

for the source term $\nabla_s \chi$ in (3.1) (Stiemer et al., 2006a), with

$$c := \left\{ r \int_{A_{ck}} \frac{1}{r} \mathbf{e}_\varphi \cdot \mathbf{n}_k \right\}^{-1}. \quad (3.4)$$

Note that the latter quantity is independent of the chosen cross section A_{ck} under the given geometric conditions. Here, \mathbf{e}_φ denotes a unit vector in φ -direction and A_{ck} the cross section of the k^{th} torus with outer unit normal vector \mathbf{n}_k . As such, the model simplifications just discussed result in an analytic solution of (3.2) and so the elimination of χ as a degree-of-freedom in the model. Substituting (3.3) into (3.1), forming the scalar product of the result with the test vector potential \mathbf{a}_* , and partial integration, yields the weak form

$$\begin{aligned} & \int_R \partial \mathbf{a} \cdot \mathbf{a}_* + \int_R \kappa_{\text{EM}} \nabla_s \mathbf{a} \cdot \nabla_s \mathbf{a}_* \\ &= \sum_k \int_{W_{ck}} c \left\{ \sigma_{\text{EM}}^{-1} I + \int_{A_{ck}} \mathbf{n}_k \cdot \partial \mathbf{a} \right\} \mathbf{e}_\varphi \cdot \mathbf{a}_*, \end{aligned} \quad (3.5)$$

together with the boundary conditions for \mathbf{a} as discussed above. The relation (3.5) is the starting point for the finite element discretization to be discussed below.

Consider next the mechanical part of the coupled model. This is based on the weak momentum balance of the deformation field ξ . Assuming purely kinematic boundary conditions, this is given by

$$\int_{B_r} (\varrho_r \ddot{\xi} - \mathbf{f}) \cdot \xi_* + \mathbf{P} \cdot \nabla_r \xi_* = 0 \quad (3.6)$$

with respect to the referential configuration $B_r \subset R$ for all corresponding test fields ξ_* . Here,

$$\mathbf{f} = \det(\mathbf{F}) \mathbf{l} = \det(\mathbf{F}) \mathbf{j} \times \mathbf{b} \quad (3.7)$$

represents the Lorentz (body) force (density), \mathbf{l} its representation in the current configuration, \mathbf{P} the first Piola-Kirchhoff stress, and $\mathbf{F} := \nabla_r \xi$ the deformation gradient. The mechanical model is completed by the specification of the material model. Here, attention is restricted to such a model for the metallic workpiece, which is formulated here as a hyperelastic, viscoplastic material. For simplicity, the (mild) elastic and flow anisotropy of the metals of interest (*e.g.*, Al) is neglected here, as well as any kinematic hardening. More generally, *e.g.*, for the case of deformation-induced anisotropic flow behavior (*e.g.*, Svendsen, 2001), this is of course no longer possible. Since the metal forming processes of interest here are predominantly monotonic in nature, however, this last assumption is reasonable. In this case, the constitutive model is specified via the form of the referential free energy density $\psi_r(\ln \mathbf{V}_E, \epsilon_P)$ together with the evolution relations for the elastic left logarithmic stretch tensor $\ln \mathbf{V}_E$ and accumulated equivalent inelastic deformation measure ϵ_P . In the context of small elastic strain, the usual Hooke-based form

$$\psi_r(\ln \mathbf{V}_E, \epsilon_P) = \frac{1}{2} \kappa_r (\mathbf{I} \cdot \ln \mathbf{V}_E)^2 + \mu_r \text{dev}(\ln \mathbf{V}_E) \cdot \text{dev}(\ln \mathbf{V}_E) + \psi_P(\epsilon_P) \quad (3.8)$$

is relevant. Another common assumption in the non-isothermal context in the case of metals is that of constant specific heat (*e.g.*, Rosakis et al., 2000). Here, κ_r represents the bulk modulus, μ_r the shear modulus, and $\psi_P(\epsilon_P)$ the contribution from energy storage due to isotropic hardening processes as usual. From (3.8), one obtains in particular the usual hyperelastic form

$$\mathbf{K} = \partial_{\ln \mathbf{V}_E} \psi_r = 3\kappa_r \text{sph}(\ln \mathbf{V}_E) + 2\mu_r \text{dev}(\ln \mathbf{V}_E) \quad (3.9)$$

for the Kirchhoff stress $\mathbf{K} = \mathbf{P}\mathbf{F}^T$. As usual, $\psi_P(\epsilon_P)$ is estimated with the help of fits to the quasi-static yield curve for the materials of interest at room temperature, as discussed in what follows. Consider next the evolution of the internal variables and the inelastic behavior. In the case of the metallic polycrystalline materials of interest at a low-to-moderate homologous temperature, inelastic deformation processes are controlled predominantly by the activation of dislocation glide on glide systems (*e.g.*, Kocks and Mecking, 2003; Teodosiu, 1997). Indeed, this seems to be the case even at high strain-rates (*e.g.*, Frost and Ashby, 1982). Apparently, higher homologous temperature levels are required for other mechanics such as dislocation climb or even dynamic recrystallization to begin playing a role. Resistance to dislocation glide arising due to obstacles and other factors is related in the phenomenological context to hardening behavior. Quasi-static processes of this nature contributing to energy storage in the material result in the contribution

$$-\varsigma_P := \psi_{r, \epsilon_P} \quad (3.10)$$

to the effective quasi-static flow stress in the material. Such resistance to dislocation motion can be overcome by thermal fluctuation under the action of the local effective stress, represented in

the current phenomenological context by $\sigma_{\text{vM}}(\mathbf{K}) + \varsigma_{\text{P}} - \sigma_{\text{F0}}$, where $\sigma_{\text{vM}}(\mathbf{K})$ represents the von Mises effective stress with respect to \mathbf{K} , and σ_{F0} is the initial flow stress. On this basis,

$$f_{\text{P}}(\mathbf{K}, \varsigma_{\text{P}}) := \sigma_{\text{vM}}(\mathbf{K}) + \varsigma_{\text{P}} - \sigma_{\text{F0}} \quad (3.11)$$

represents an activation measure or overstress in the current rate-dependent context. A power-law approximation of the more exact transition-state-based micromechanical relations for the kinetics of dislocation glide (*e.g.*, Kocks and Mecking, 2003; Teodosiu, 1997) leads to the power-law form

$$\phi(\epsilon_{\text{P}}, \mathbf{D}, \mathbf{K}, \varsigma_{\text{P}}) = \frac{\gamma_{\text{P}}(\epsilon_{\text{P}}, \mathbf{D}) \sigma_{\text{P}}(\epsilon_{\text{P}}, \mathbf{D})}{m_{\text{P}}(\epsilon_{\text{P}}, \mathbf{D}) + 1} \left\langle \frac{f_{\text{P}}(\mathbf{K}, \varsigma_{\text{P}})}{\sigma_{\text{P}}(\epsilon_{\text{P}}, \mathbf{D})} \right\rangle^{m_{\text{P}}(\epsilon_{\text{P}}, \mathbf{D})+1} \quad (3.12)$$

upon which the evolution of the internal variables is based. Here, σ_{P} represents the dynamic contribution to the flow stress, γ_{P} a characteristic strain-rate and m the strain-rate exponent. Further, $\langle x \rangle := \frac{1}{2}(x + |x|)$ represents the ramp function. As indicated, γ_{P} , σ_{P} and m_{P} are in general functions of accumulated inelastic deformation and deformation rate. For simplicity, however, these material properties will be treated as constants in the algorithmic formulation to follow. To indicate this, we write $\gamma_0 \hat{=} \gamma_{\text{P}}$, $\sigma_0 \hat{=} \sigma_{\text{P}}$, and $m_0 \hat{=} m_{\text{P}}$. The form (3.12) determines the evolution relations

$$\begin{aligned} -\ln \mathbf{V}_{\text{E}}^* &= \partial_{\mathbf{K}} \phi = \sqrt{\frac{3}{2}} \operatorname{sgn}(\operatorname{dev}(\mathbf{K})) \dot{\epsilon}_{\text{P}} \quad (\mathbf{K} \neq \mathbf{0}), \\ \dot{\epsilon}_{\text{P}} &= \partial_{\varsigma_{\text{P}}} \phi = \gamma_0 \left\langle \frac{f_{\text{P}}}{\sigma_0} \right\rangle^{m_0} \quad (f_{\text{P}} > 0), \end{aligned} \quad (3.13)$$

for the evolution of the internal variables, with

$$\ln \mathbf{V}_{\text{E}}^* := \frac{1}{2} \ln(\mathbf{F} \overline{\mathbf{C}}_{\text{P}}^{-1} \mathbf{F}^{\text{T}}) \quad (3.14)$$

in terms of the inverse plastic right Cauchy-Green deformation $\mathbf{C}_{\text{P}}^{-1}$.

In summary, the material parameters introduced in the above model include the magnetic diffusivity κ_{EM} , the electrical conductivity σ_{EM} , the bulk modulus κ_r , the shear modulus μ_r , as well as the dynamic viscoplastic parameters γ_0 , σ_0 , and m_0 appearing in the viscoplastic potential (3.12) and flow rule (3.13). For the purpose of model identification, we will assume to a good approximation that the first five of these are known and fixed. In this case, the array \mathbf{p} of parameters to be identified takes the form

$$\mathbf{p} := (\gamma_0, \sigma_0, m_0). \quad (3.15)$$

The values which these may take are as usual subject to certain physical constraints, *e.g.*, $\gamma_0 > 0$ and $\sigma_0 > 0$. Further, micromechanical as well as experimental observations suggest that $m_0 > 1$. This also holds from the point of view that (3.13) represents an approximation of more exact transition-state-based micromechanical relations (*e.g.*, Kocks and Mecking, 2003; Teodosiu, 1997). We return to these issues below.

Next, the algorithmic formulation of the above presented model is summarized. The difference in electromagnetic and mechanical timescales, together with the distinct nature of the

fields involved (*i.e.*, Eulerian in the electromagnetic case, Lagrangian in the mechanical large-deformation context), suggest a staggered numerical solution procedure involving separate grids for the electromagnetic and mechanical fields (see Figure 3.2). In addition, the electromagnetic mesh is adapted according to the movement of the structure by means of an ALE-scheme. Each algorithmic formulation is discussed separately before being combined in the framework of the staggered algorithm at the end of this section. The discretization of the mechanical weak form (3.6) by means of the finite element method and usage of the Newmark algorithm to integrate (3.6) over the time interval $t_{n,n+1}$, yields the implicit algorithmic system

$$\mathbf{f}_{n+1,n}^s \{ \mathbf{x}_{n+1}^s, \mathbf{p} \} = \mathbf{0} \quad (3.16)$$

in terms of the array \mathbf{x}_{n+1}^s of time dependent nodal positions at fixed Lorentz force $\mathbf{l}_{n+1} = \sigma_{\text{EM}} \text{curl}_s^{n+1} \mathbf{a} \times \partial \mathbf{a}_{n+1}$. The solution of (3.16) is obtained via Newton-Raphson iteration in terms of its consistent linearization. A detailed and concise discussion of the advantages of an implicit solution scheme in contrast to an explicit one in the context of metal forming can be found in Tekkaya (2000). Through \mathbf{K} , the discrete form (3.16) depends as well on the current (unknown) values of the internal variables. Using backward-Euler integration to solve (3.13) over $t_{n,n+1}$, one obtains the algorithmic relation written in the compact form

$$r_{\alpha} \mathbf{r}_{\alpha} \{ \boldsymbol{\alpha}_{n+1}, \mathbf{F}_{n+1}, \mathbf{p} \} = \mathbf{0}, \quad (3.17)$$

with $\boldsymbol{\alpha} = (\ln \mathbf{V}_{\text{E}}, \epsilon_{\text{P}})$ and $r_{\alpha} = (r_{\ln \mathbf{V}_{\text{E}}}, r_{\epsilon_{\text{P}}})$. This last relation is again solved via Newton-Raphson iteration and holds at each integration point in each element of the structure.

Turning next to the electromagnetic weak form (3.5), finite element discretization and temporal integration via the generalized trapezoidal rule over the interval $t_{n,n+1}$ yield the system

$$\begin{bmatrix} \mathbf{A}^s & \mathbf{B}_{n+1}^s \\ \mathbf{I} & -\alpha t_{n+1,n} \mathbf{I} \end{bmatrix} \begin{bmatrix} \mathbf{a}_{n+1}^s \\ \dot{\mathbf{a}}_{n+1}^s \end{bmatrix} = \begin{bmatrix} \mathbf{c}_{n+1}^s \\ \mathbf{a}_n^s + (1 - \alpha) t_{n+1,n} \dot{\mathbf{a}}_n^s \end{bmatrix} \quad (3.18)$$

to be solved for \mathbf{a}_{n+1}^s and $\dot{\mathbf{a}}_{n+1}^s$, in the context of the current staggered approach with fixed \mathbf{x}_{n+1}^s . Here, \mathbf{A}^s represents the discretized spatial "stiffness" part and \mathbf{B}^s the diffusive "mass" part in (3.5). Through \mathbf{c}_{n+1}^s the measured input current, which is driving the forming operation, is implemented. The amount of artificial damping is controlled by the parameter $0 < \alpha \leq 1$.

The aforementioned staggered solution scheme is described in detail in what follows:

1. Update the boundary conditions and supply terms (*e.g.*, current I in the tool coil) to $t = t_{n+1}$.
2. Update the boundary conditions and initialize the nodal fields, *i.e.*, $\mathbf{x}_{n+1}^{s(k)} = \mathbf{x}_n^s$, $\dot{\mathbf{x}}_{n+1}^{s(k)} = \dot{\mathbf{x}}_n^s$, $\ddot{\mathbf{x}}_{n+1}^{s(k)} = \ddot{\mathbf{x}}_n^s$ and $\mathbf{e}_{n+1}^{s(k)}$ for $k = 1$.
3. Obtain $\mathbf{a}_{n+1}^{s(k)}$ and $\dot{\mathbf{a}}_{n+1}^{s(k)}$ from (3.18) depending in particular on the (*e.g.*, experimentally determined) value I_{n+1} of the electrical current in the tool coil as well as the current spatial distribution of σ_{EM} and κ_{EM} in R .
4. Obtain $\mathbf{l}_{n+1}^{(k)}$ from (3.7). Transfer the results to the embedded Lagrangian mesh for the workpiece.

5. Solve (3.16) at fixed $\mathbf{l}_{n+1}^{(k)}$ and \mathbf{p} to obtain $\mathbf{x}_{n+1}^{s(k+1)}$, $\dot{\mathbf{x}}_{n+1}^{s(k+1)}$, $\ddot{\mathbf{x}}_{n+1}^{s(k+1)}$ and $\mathbf{e}_{n+1}^{s(k+1)}$.
6. Steps 2-5 are repeated for $k = 2, \dots$ until convergence is obtained, yielding \mathbf{x}_{n+1}^s , \mathbf{a}_{n+1}^s , and the updated internal variables.

We refer to this as Algorithm 1 in the following.

3.3 Model identification procedure

In the algorithm of the previous section, \mathbf{p} was fixed. Since we assume the material behavior here to be homogeneous, the parameter identification takes place basically at the material point level with the help of the finite element solution at the structural level. Indeed however, in the case of EMF and other high-strain-rate methods, the deformation field is not homogeneous. To formulate the corresponding algorithm, we proceed as follows. First of all, since the data available to us concerns the deformation of the workpiece, for matters of simplicity attention is restricted to the mechanical part of the model. Let $\mathbf{d}_{\text{exp}}(t)$ represent the (incomplete and inexact) experimental data array (*e.g.*, discrete displacement field of the specimen) parameterized in time. This is to be compared with the corresponding information derived from the solution of (3.16) and (3.18) using the algorithm at the end of the last section. As implied by the notation, this solution takes the form of \mathbf{x}_i^s and \mathbf{a}_i^s as implicit functions of all parameters and in particular \mathbf{p} , at each discrete time $t = t_i$ for $i = 1, \dots, m$ in the context of $[0, d] = \bigcup_{i=1}^m [t_{i-1}, t_i]$. Since \mathbf{p} is constant in space and time, the complete sets $(\mathbf{x}_0^s, \mathbf{x}_1^s, \dots, \mathbf{x}_m^s)$ and $(\mathbf{a}_0^s, \mathbf{a}_1^s, \dots, \mathbf{a}_m^s)$ of algorithmic solutions in the time interval $[0, d] = \bigcup_{i=1}^m [t_{i-1}, t_i]$ are relevant here. In the context of the staggered solution approach being pursued here, as well as due to the fact that the available data are purely mechanical in nature (*i.e.*, deformation data), we neglect for simplicity the implicit dependence of \mathbf{a}^s on \mathbf{p} and focus on that implied by (3.16). Again, to indicate this implicit dependence of \mathbf{x}_{n+1}^s on \mathbf{p} in the notation, we write $\mathbf{x}_{n+1}^s = \mathbf{x}_{n+1,n}^s\{\mathbf{p}\}$. In this context, the choice of \mathbf{p} is judged to be “good” if the deviation

$$\mathbf{z}_{n+1}\{\mathbf{p}\} := \mathbf{d}_{\text{exp}}^s(t_{n+1}) - \mathbf{d}_{\text{mod}}^s(\mathbf{x}_{n+1,n}^s\{\mathbf{p}\}) \quad (3.19)$$

between $\mathbf{d}_{\text{exp}}^s$ and the model prediction $\mathbf{d}_{\text{mod}}^s(\mathbf{x}_{n+1}^s)$ is “small.” Here, $\mathbf{d}_{\text{mod}}^s$ maps the simulation results \mathbf{x}_{n+1}^s onto a form consistent with the experimental observations. In Section 3.6, it is shown (see Figure 3.6) that, due to the weak coupling, the neglect of $\mathbf{a}_{n+1}^s = \mathbf{a}_{n+1,n}^s\{\mathbf{p}\}$ in (3.19) is justified. As such, the identification procedure involves directly the mechanical part of the coupled problem. In general, note that $\mathbf{d}_{\text{mod}}^s$ could be highly non-trivial, *e.g.*, when inhomogeneous displacement fields are measured optically and compared with finite element nodal displacements (Scheday, 2003). In the current context, however, the data consists of the tube displacement at a single point in the structure as a function of time (see Figure 3.3). In this case, a direct comparison of experimental and simulation results is possible.

Statistical maximum likelihood considerations (*e.g.* Bevington, 1969; Press et al., 2002, Ch. 15) motivate the chi-square form

$$\chi^2\{\mathbf{p}\} := \frac{1}{2} \sum_{i=1}^m \mathbf{W}_i \mathbf{z}_i\{\mathbf{p}\} \cdot \mathbf{W}_i \mathbf{z}_i\{\mathbf{p}\} = \frac{1}{2} \sum_{i=1}^m \mathbf{z}_i\{\mathbf{p}\} \cdot \mathbf{E}_i \mathbf{z}_i\{\mathbf{p}\} \quad (3.20)$$

for the objective function based on $\mathbf{z}^s\{\mathbf{p}\}$. Here, \mathbf{W}_i represents the weighting matrix taking into account possible differences in variance and physical dimension of the experimental data, and $\mathbf{E}_i := \mathbf{W}_i^T \mathbf{W}_i$. As usual, the best-fit parameter set \mathbf{p}_* then minimizes $\chi^2\{\mathbf{p}\}$,

$$\chi^2\{\mathbf{p}_*\} \leq \chi^2\{\mathbf{p}\}, \quad \forall \mathbf{p}. \quad (3.21)$$

In the differentiable case, \mathbf{p}_* is determined as usual by

$$\begin{aligned} \partial_{\mathbf{p}}^a \chi^2 &= \sum_{i=1}^m (\partial_{\mathbf{p}}^a \mathbf{z}_i)^T \mathbf{E}_i \mathbf{z}_i = \mathbf{0}, \\ \partial_{\mathbf{p}}^a (\partial_{\mathbf{p}}^a \chi^2) &= \sum_{i=1}^m (\partial_{\mathbf{p}}^a \mathbf{z}_i)^T \mathbf{E}_i (\partial_{\mathbf{p}}^a \mathbf{z}_i) + (\partial_{\mathbf{p}}^a (\partial_{\mathbf{p}}^a \mathbf{z}_i))^T \mathbf{E}_i \mathbf{z}_i \quad \text{positive-definite,} \end{aligned} \quad (3.22)$$

where ∂^a represents the partial algorithmic or implicit derivative operator. Note that

$$\partial_{\mathbf{p}}^a \mathbf{z}_i = -(\partial_{\mathbf{x}^s} \mathbf{d}_{\text{mod}})(\partial_{\mathbf{p}}^a \mathbf{x}_{i,i-1}^s) = (\partial_{\mathbf{x}^s} \mathbf{d}_{\text{mod}})(\partial_{\mathbf{x}_i^s} \mathbf{f}_{\mathbf{x}_i,i-1}^s)^{-1} (\partial_{\mathbf{p}}^a \mathbf{f}_{\mathbf{x}_i,i-1}^s) \quad (3.23)$$

holds via (3.16). In addition,

$$\partial_{\mathbf{x}^s} \mathbf{f}_{\mathbf{x}_i,i-1}^s = \sum_e \mathbf{I}_{\mathbf{x}}^{eT} (\partial_{\mathbf{x}^e} \mathbf{f}_{\mathbf{x}_i,i-1}^e) \mathbf{I}_{\mathbf{x}}^e, \quad \partial_{\mathbf{p}}^a \mathbf{f}_{\mathbf{x}_i,i-1}^s = \sum_e \mathbf{I}_{\mathbf{x}}^{eT} (\partial_{\mathbf{p}}^a \mathbf{f}_{\mathbf{x}_i,i-1}^e) \quad (3.24)$$

follow from (3.16). Further,

$$\begin{aligned} \partial_{\mathbf{x}_i^e} \mathbf{f}_{\mathbf{x}_i,i-1}^e &= \partial_{\mathbf{x}^e} \mathbf{f}_{\mathbf{x}_i,i-1}^e + (\partial_{\mathbf{e}^e} \mathbf{f}_{\mathbf{x}_i,i-1}^e)(\partial_{\mathbf{x}_i^e} \mathbf{e}_{i,i-1}^e) \\ &= \partial_{\mathbf{x}^e} \mathbf{f}_{\mathbf{x}_i,i-1}^e - (\partial_{\mathbf{e}^e} \mathbf{f}_{\mathbf{x}_i,i-1}^e)(\partial_{\mathbf{e}^e} r_{\alpha i,i-1}^e)^{-1} (\partial_{\mathbf{x}^e} r_{\alpha i,i-1}^e), \\ \partial_{\mathbf{p}}^a \mathbf{f}_{\mathbf{x}_i,i-1}^e &= (\partial_{\mathbf{e}^e} \mathbf{f}_{\mathbf{x}_i,i-1}^e)(\partial_{\mathbf{p}}^a \mathbf{e}_{i,i-1}^e) \\ &= -(\partial_{\mathbf{e}^e} \mathbf{f}_{\mathbf{x}_i,i-1}^e)(\partial_{\mathbf{e}^e} r_{\alpha i,i-1}^e)^{-1} (\partial_{\mathbf{p}}^a r_{\alpha i,i-1}^e), \end{aligned} \quad (3.25)$$

are obtained from (3.17). In particular, $\partial_{\mathbf{e}^e} r_{\alpha i,i-1}^e$ represents the Jacobian matrix of the local Newton-Raphson iteration for the internal variables at the Gauss-point level. Now, if a local quadratic approximation to χ^2 is reasonable, then the first of these can be solved via Newton-Raphson iteration as based on

$$(\partial_{\mathbf{p}}^a (\partial_{\mathbf{p}}^a \chi^2))_k [\mathbf{p}_{k+1} - \mathbf{p}_k] = -(\partial_{\mathbf{p}}^a \chi^2)_k. \quad (3.26)$$

Otherwise, one would have to “globalize” this approach by combining it with, *e.g.*, a line search or steepest descent step. In any case, assuming that \mathbf{z} becomes small as \mathbf{p}_{k+1} approaches \mathbf{p}_* , the second term $(\partial_{\mathbf{p}}^a \mathbf{z}_i)^T \mathbf{E}_i \mathbf{z}_i$ in the sum in (3.22)₂ should become negligible in comparison to the first one. Further, assuming the model is physically reasonable, this term is just related to the random measurement error at each point (Press et al., 2002). This error can have either sign, and should in general be uncorrelated with the model. As such, we work with the approximation

$$\partial_{\mathbf{p}}^a (\partial_{\mathbf{p}}^a \chi^2) \approx \sum_{i=1}^m (\partial_{\mathbf{p}}^a \mathbf{z}_i)^T \mathbf{E}_i (\partial_{\mathbf{p}}^a \mathbf{z}_i) \quad (3.27)$$

in (3.26). On this basis, \mathbf{p}_* is determined via the following algorithm:

1. Choose starting values \mathbf{p}_k ($k = 1$) for the parameters to be identified.

2. Solve for $\mathbf{x}_{i,i-1}^s\{\mathbf{p}_k\}$, $\mathbf{a}_{i,i-1}^s\{\mathbf{p}_k\}$, and $\mathbf{e}_{i,i-1}^s\{\mathbf{p}_k\}$ for all times steps $i = 1, \dots, m$ using Algorithm 1.
3. Use (3.26) to solve for \mathbf{p}_{k+1} .
4. Repeat steps 2.-3. for $k = 2, \dots$ until convergence is achieved.

This is referred to as Algorithm 2 in what follows. Again, note that we are neglecting the (weak) coupling $\mathbf{a}_{n+1}^s = \mathbf{a}_{n+1,n}^s\{\mathbf{p}\}$ in the identification process. Clearly, this scheme is general and can be applied to any model identification based on a staggered solution scheme.

Consider next a variation $\delta\mathbf{p}$ of the parameters. This induces for example that

$$\delta\mathbf{x}_i^s = (\partial_{\mathbf{p}}^a \mathbf{x}_{i,i-1}^s) \delta\mathbf{p} = -(\partial_{\mathbf{x}_i^s}^a \mathbf{f}_{\mathbf{x}_i^s, i-1}^s)^{-1} (\partial_{\mathbf{p}}^a \mathbf{f}_{\mathbf{x}_i^s, i-1}^s) \delta\mathbf{p} \quad (3.28)$$

in \mathbf{x}_i^s , representing the sensitivity of \mathbf{x}_i^s to variations in \mathbf{p} . As it turns out, it is useful to work with a normalized sensitivity matrix $\mathbf{S}(t_i)$ based on this

$$S_{jk}(t_i) := \frac{|p_k|}{|x_{ij}^s|} (\partial_{\mathbf{p}}^a \mathbf{x}_{i,i-1}^s)_{jk} \quad (3.29)$$

(e.g., Kleiber, 1997). In particular, $S_{jk}(t_i)$ represents the variation of x_j due to a variation of p_k at $t = t_i$. The normalization facilitates comparison of the sensitivities for different model parameters (Bolzon et al., 2004). Possible correlations among the model parameters are determined by the covariance matrix

$$\mathbf{C} := \{\partial_{\mathbf{p}} (\partial_{\mathbf{p}} \chi^2)\}_*^{-1} \approx \left\{ \sum_{i=1}^m (\partial_{\mathbf{p}} \mathbf{z}_i)^T \mathbf{E}_i (\partial_{\mathbf{p}} \mathbf{z}_i) \right\}_*^{-1} \quad (3.30)$$

(Press et al., 2002). In the general case of identification of more than one material parameter at a time, the correlation of the parameters represents a further important consideration in the context of determining a unique and accurate set of parameters (Bevington, 1969). As usual, the correlation coefficient

$$\rho_{ij} := \frac{C_{ij}}{\sqrt{C_{ii}C_{jj}}} \quad (3.31)$$

is a measure of the degree of correlation between two parameters. Let $\boldsymbol{\rho}$ represent the corresponding matrix, such that $[\boldsymbol{\rho}]_{ij}$ denotes its the ij -th element. In particular, $|\rho_{ij}| = 1$ implies that p_i and p_j are linearly dependent, in which case no unique solution of the optimization problem exists. In practice, the closer $|\rho_{ij}|$ is to 1, the less distinguishable are the contributions of p_i and p_j to the model behavior, *i.e.*, on the basis of the data used for the model identification.

Further, experimental error and statistical uncertainty are incorporated into the standard deviation of the determined model parameter values. To estimate this standard deviation, the Gaussian law of error propagation is assumed. In this case, the variance σ_k of $p_k \in \mathbf{p}$ is given by

$$\sigma_{p_k} = \sqrt{[\mathbf{C}]_{kk}} \quad (3.32)$$

in terms of the components of \mathbf{C} . To verify the current approach and obtain additional insight, these variances are also investigated using synthetic data sets based on known material parameter values endowed with experimental uncertainties equivalent to those of the actual experimental data.

3.4 Parameter identification, correlation and sensitivity

In the case of electromagnetic tube forming, the experimental results take the form of displacement values at the center of the tube in the radial direction. The measurement system utilizes a laser beam detected by a Position Sensitive Device (PSD). During the forming process, the sheet metal moves between the laser and the PSD, resulting in a change in detected laser light intensity which is directly proportional to the radial expansion (see Figure 3.3, left). The setup allows for carrying out of forming operations at different initial discharging energies of the capacitor depicted in Figure 3.1 resulting in an increasing deformation with increasing discharging energy E_{cp} . In this study we examined forming operations at three different discharging energies, namely 650 J, 800 J and 1000 J (see figures 3.3 and 3.4). Using this method, one obtains

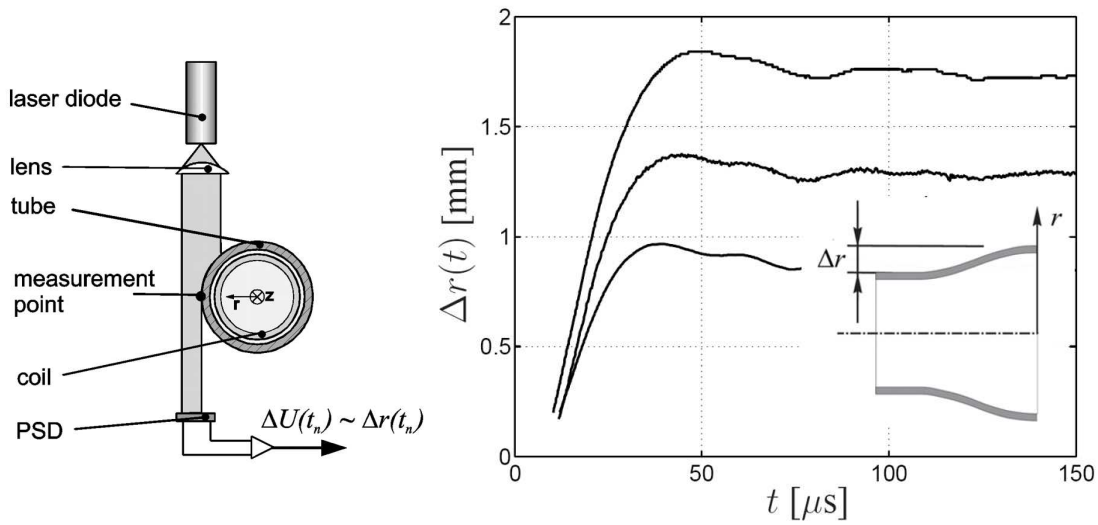


Figure 3.3: Experimental measurement of tube forming. Left: Laser-based measurement of the change in the outer radius of the tube with time. Right: Measured change of tube radius at the middle of the tube for the discharging energies 650 J, 800 J and 1000 J.

the data $\mathbf{d}_{\text{exp}}(t)$ in the form of the radial component $\Delta r(t) = u_r(t)$ of the displacement field \mathbf{u} in the middle of the tube, *i.e.*,

$$\mathbf{d}_{\text{exp}}(t_i) = (\Delta r(t_i)), \quad i = 0, \dots, m. \quad (3.33)$$

Together with the simulation, this determines $\mathbf{z}_i\{\mathbf{p}\}$ in (3.19). Assuming the same standard deviation σ for all data for simplicity, $\mathbf{W}_i = \sigma^{-1}\mathbf{I}$ for all $i = 1, \dots, m$, such that

$$\chi^2\{\mathbf{p}\} = \frac{1}{2\sigma^2} \sum_{i=1}^m \mathbf{z}_i\{\mathbf{p}\} \cdot \mathbf{z}_i\{\mathbf{p}\} \quad (3.34)$$

follows for $\chi^2\{\mathbf{p}\}$ from (3.20). Next, we turn to the specification of the forming setup. The tool coil consists of technically pure copper. The tube specimens utilized in the current work consist of AA 6060 aluminum. Values for the elastic constants, the mass density and the electromagnetic constants for this material and copper were obtained from the literature and are summarized in Table 3.1. The quasi-static yield behavior of AA 6060 is described here by the contribution

$$\psi_P(\epsilon_P) = c_1(\epsilon_P + c_2)^{c_3} \quad (3.35)$$

κ_r [MPa]	μ_r [MPa]	ϱ_r [kg m ⁻³]	$\sigma_{EM Cu}$ [V A ⁻¹ m ⁻¹]	$\sigma_{EM Al}$ [V A ⁻¹ m ⁻¹]
6.77×10^4	2.59×10^4	2.70×10^3	5.60×10^1	3.46×10^1

Table 3.1: Fixed elastic and electromagnetic properties of AA 6060 and conductivity of tool coil.

σ_{F0} [MPa]	c_1 [MPa]	c_2 -	c_3 -
7.17×10^1	3.32×10^2	1.00×10^{-3}	3.87×10^{-1}

Table 3.2: Fixed quasi-static isotropic hardening parameters for AA 6060.

γ_0 [s ⁻¹]	σ_0 [MPa]	m_0 -
6.00×10^3	5.00×10^1	4.00×10^0

Table 3.3: Initial values for the dynamic inelastic parameters for AA 6060.

to the stored energy due to isotropic hardening processes. The corresponding parameter values together with estimates for the initial flow stress σ_{F0} were determined with the help of tensile tests. These are shown in Table 3.2.

Lastly, starting values for the viscoplastic material parameters \mathbf{p} to be identified were obtained from Jones (1997) and are listed in Table 3.3. For completeness, the model geometry and the measured input current are depicted in Figure 3.4. For the finite element simulations, convergence studies of the coupled, as well as the purely mechanical problem indicate that four elements over the tube thickness yield a converged solution. The element type that was utilized represents a bilinear displacement formulation for large deformation problems. In addition time step size investigations (Stiemer et al., 2006a) for such systems imply that $t_{n+1,n} = 1 \mu\text{s}$ is a reasonable choice. Before carrying out the actual identification, consider the correlation and sensitivity properties of the model determined for a discharging energy of 1000 J. To this end, the derivatives $\partial_{\mathbf{p}}^a \mathbf{x}_{i,i-1}^s$, $i = 1, \dots, m$, were calculated numerically via finite differences using the starting values for \mathbf{p} given in Table 3.3, yielding

$$\boldsymbol{\rho} = \begin{pmatrix} 1.000000 & 1.000000 & 0.585362 \\ 1.000000 & 1.000000 & 0.586542 \\ 0.585362 & 0.586542 & 1.000000 \end{pmatrix}. \quad (3.36)$$

The values in (3.36) indicate that γ_0 and σ_0 are linearly dependent. Evidently, this can also be seen by factoring σ_0 out of (3.13). Consequently, it is reasonable to fix γ_0 to its initial value, in which case \mathbf{p} reduces to

$$\mathbf{p} = (\sigma_0, m_0). \quad (3.37)$$

Next, each $S_{jk}(t_i)$, $i = 1, \dots, m$, was calculated via (3.29). In particular, these are based on the single experimental result $\mathbf{d}_{\text{exp}}(t_i) = (\Delta r(t_i))$ at each t_i , $i = 1, \dots, m$. The results are displayed in Figure 3.5. As shown, in the first part of the forming process (*i.e.*, up to 7 μs), the deformation is elastic, and the sensitivity of the model to variations of the inelastic parameters is zero. Then the structure begins to deform inelastically and the sensitivity of

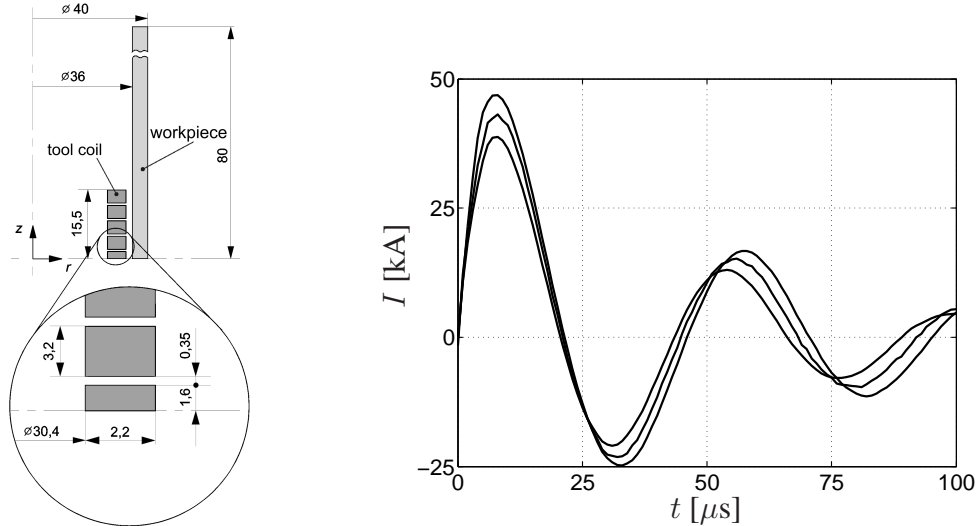


Figure 3.4: Experimental set-up and measured input currents. Left: Geometry of workpiece and tool coil for tube expansion (dimensions in mm). Right: Measured input currents $I(t)$ in the tool coil as a function of time for the discharging energies 650 J, 800 J and 1000 J.

the model to variations in both parameters increases up to about 55μ s. At this instance the deformation is again elastic. After 55μ s, the structure deforms mainly elastically and the sensitivities oscillate about a constant value of $S_{11} = 0.23$ and $S_{12} = 0.052$. The oscillations are due to the normalization using \mathbf{d}_{sim} . Note that the sensitivity of the model to the inelastic parameters does not reduce to zero during elastic deformation because of the accumulated and history-dependent nature of ϵ_p .

In comparison with other cases in the literature (Bolzon et al., 2004; Chen and Chen, 2003), the magnitudes of the sensitivities here indicate a good identifiability of the material parameters at the high strain-rates of interest here, for which the power-law form (3.13) of the flow rule is physically reasonable for $\sigma_0 = 50$ MPa and $m_0 = 4$. If the effect of rate hardening is reduced by setting $\sigma_0 = 5$ MPa, the sensitivity with respect to both parameters is reduced by one order of magnitude. This would make the identification much more difficult. In the real experimental situation, this could be the case for materials with less pronounced rate effects.

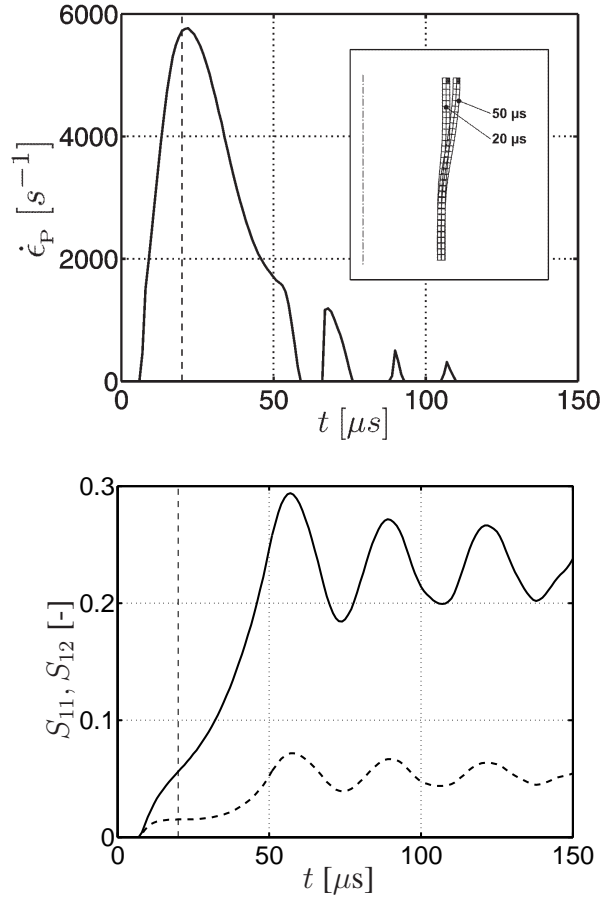


Figure 3.5: Correlation of model sensitivity to σ_0 and m_0 with inelastic deformation as measured by $\dot{\epsilon}_p$. Above: Equivalent inelastic strain-rate $\dot{\epsilon}_p$ at the center of the tube as a function of time. Below: Sensitivity of the model to changes in σ_0 (S_{11} , solid line) and m_0 (S_{12} , dashed line) as a function of time.

3.5 Identification using synthetic data

Following Harth et al. (2004), the purpose of the current section is to test the identification procedure under various assumptions regarding the experimental the data. To this end, the parameter values in Table 3.3 were used to generate synthetic data. Working for simplicity with the case of no measurement errors first, consider the dependence of the determination of the material parameters on the number of updates of the Lorentz force, *i.e.*, on the number of coupled simulations required. To look into this, a synthetic experimental data set analogous to (3.33) is generated using the parameter values $\mathbf{p} = (50, 4)$. The starting values \mathbf{p}_1 for the determination are chosen to be (100,8). The identification procedure then begins with a fully coupled simulation to determine l_n^1 . The material parameter values are updated, and a new coupled simulation is carried out, yielding l_n^2 . The corresponding progression of updates of \mathbf{p} is shown in Figure 3.6. Each triangle represents an update at fixed body force density. Body force updates are indicated by circles.

In the case of tube forming, good accuracy is obtained using only one coupled simulation, *e.g.*, $\mathbf{p}_{15} = (5.00135 \times 10^1, 4.00839 \times 10^0)$. Indeed, a further body force update yielded only marginally better results, *e.g.*, $\mathbf{p}_{23} = (5.00000 \times 10^1, 4.00000 \times 10^0)$. This state of affairs can be

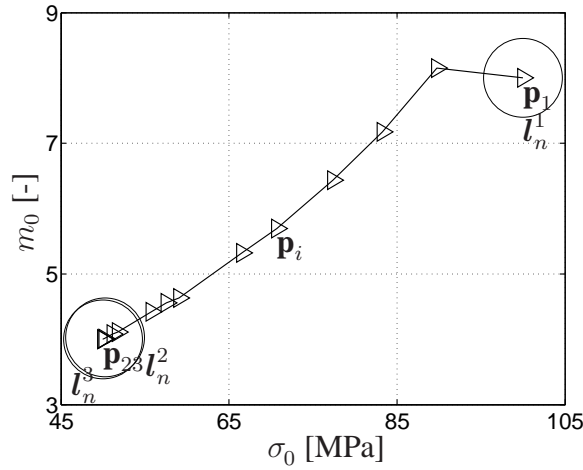


Figure 3.6: Application of the parameter identification algorithm (Algorithm 2) to synthetic data sets generated using the parameter values \mathbf{p}_* for AA 6060 from Table 3.3. Each triangle represents an update of \mathbf{p} at fixed body force density. Body force updates are indicated by circles.

explained as follows. At the beginning of the forming process, the body forces reach their maximum values at a time when the deformation of the tube is predominantly elastic. Consequently, inelasticity is not active, and the coupling is weak (Figure 3.5). This is in contrast to the case of sheet metal forming, where the Lorentz force is acting also during inelastic deformation of the sheet metal. Consequently, a larger number of Lorentz force updates is required for an accurate parameter determination.

Given the weak interaction between the body forces and inelastic processes in the case of tube forming, the body forces are fixed for simplicity in what follows. On this basis, consider the efficiency of the identification procedure for different combinations of the starting values for the material parameters. In Figure 3.7, the combinations $m_0^1/m_0 = 3$, $\sigma_0^1/\sigma_0 = 3$, and $m_0^1/m_0 = 3^{-1}$, $\sigma_0^1/\sigma_0 = 3^{-1}$ are considered. The identification procedure here is illustrated in terms of the fraction $[\mathbf{p}_n]_i/[\mathbf{p}]_i$ denoting the difference to the correctly identified material parameter for each direct computation numbered by n . If $[\mathbf{p}_n]_i/[\mathbf{p}]_i \approx 1$, the parameter can be considered to be identified. The crucial measure to quantify the efficiency of the applied methods is the number of direct model computations, as these represent the most costly operations in one iteration of the procedure. In both cases, the material parameters could be reidentified with the desired accuracy $|\mathbf{p} - \mathbf{p}_n| < 1 \times 10^{-4}$, and the identification was stopped.

On the numerical side of things, we compared the gradient-based trust-region method with the direct Nelder-Mead simplex method. Table 3.4 summarizes the efficiency of the two numerical solution methods for the different parameter value combinations considered. In all cases, the gradient-based method converges faster to the correct values than the direct approach. Due

$m_0^1/m_0, \sigma_0^1/\sigma_0$	3, 3	1/3, 1/3	3, 1/3	1/3, 3
function calls (trust-region Newton)	21	60	21	112
function calls (Nelder Mead)	120	92	90	114

Table 3.4: Numerical efficiency of the identification procedure for different starting values of the parameters and two different numerical solution methods.

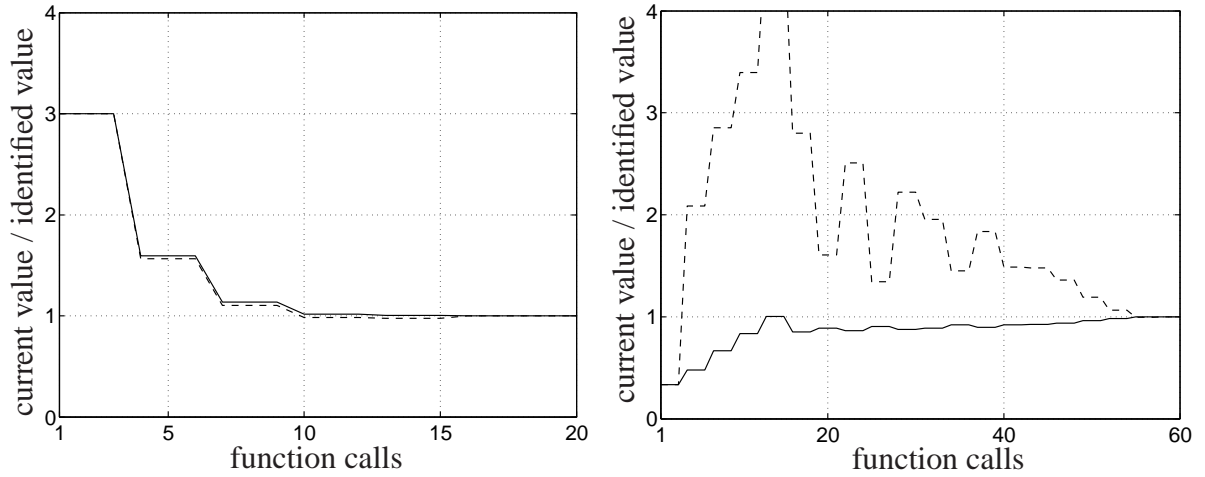


Figure 3.7: Ratio of current to identified parameter values as a function of the number of function calls for σ_0 (solid line) and m_0 (dashed line) for two different starting values. Left: $\sigma_0^1/\sigma_0 = m_0^1/m_0 = 3/1$. Right: $\sigma_0^1/\sigma_0 = m_0^1/m_0 = 1/3$.

to the mathematical form of the flow rule, initial values of m_0 which are smaller than the identified ones result in many more function evaluations.

Consider next the influence of measurement uncertainties on the parameter identification. This is done by generating a large number of data sets with normally distributed “measurement” errors. The influence of these on the confidence regions for the identification can be specified by applying the standard estimators for the mean

$$\mu_i \approx \bar{p}_i := \frac{1}{n} \sum_{k=1}^n p_i^k \quad (3.38)$$

and variance

$$\sigma_i^2 \approx s_i^2 := \frac{1}{n} \sum_{k=1}^n (p_i^k - \bar{p}_i)^2 \quad (3.39)$$

in terms of the sample variance s_i^2 , for n data. Those then facilitate the verification of confidence regions obtained from the Gaussian law of error propagation and sensitivity analysis (3.32). In the above part of Figure 3.8 the results of the error analysis for $N = 100$ experiments with a variance of $\sigma^2 = 1 \times 10^{-6}$ for each data point $\mathbf{d}_{\text{exp}}^s(t_i)$ are shown. The identified parameters so obtained can be represented in terms of their deviation from their mean values $\mathbf{p} - \bar{\mathbf{p}}$ to indicate the scattering (Press et al., 2002). In the lower part of Figure 3.8 the frequency of occurrence distributions for the parameters are shown. They can be obtained by projection onto the corresponding axis. The probability density functions obtained with the variances from the Gaussian law of error propagation are also depicted. Values for the variances estimated from the experiments are $s_{\sigma_0}^2 = 1.21 \times 10^{-3}$ and $s_{m_0}^2 = 9.86 \times 10^{-3}$ and values computed from the Gaussian law of error propagation are $\sigma_{\sigma_0}^2 = 1.24 \times 10^{-3}$ and $\sigma_{m_0}^2 = 1.01 \times 10^{-3}$, respectively. The relative variances for the strain-rate exponent are larger than the ones obtained for σ_0 . This reflects the results obtained from the sensitivity analysis; here the sensitivity with respect to m_0 turned out to be smaller than that for σ_0 (see Figure 3.8 below).

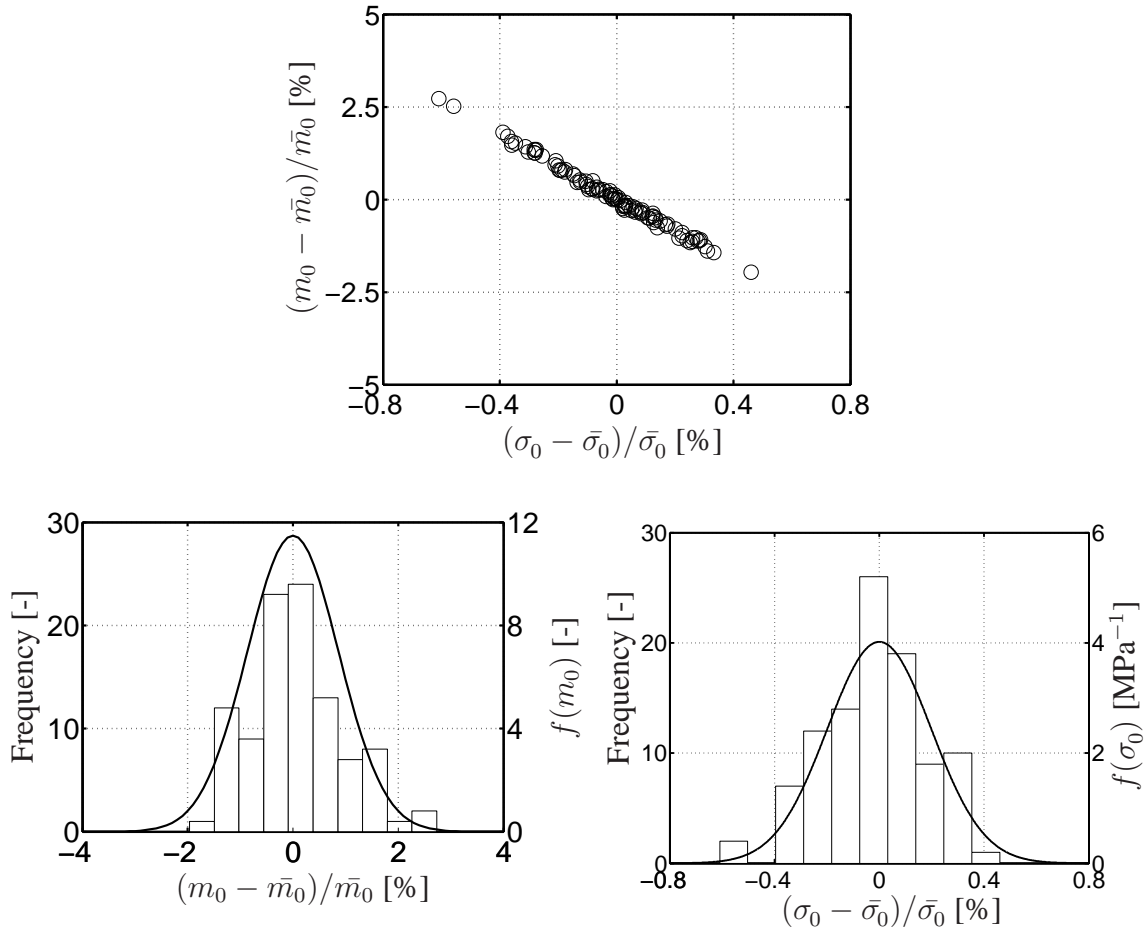


Figure 3.8: Effect of errors on determined parameter values. Above: Parameter value deviations from the mean for $N = 100$ identifications. Below left: Corresponding Gaussian distribution of deviation values for m_0 and probability density function f estimated via the sensitivity analysis and covariance matrix. Below right: Corresponding Gaussian distribution of deviation values for σ_0 .

3.6 Identification using experimental data

This section is focused on the identification of \mathbf{p} using real data. In contrast to the synthetic data sets, real data is available starting at $t = 10 \mu\text{s}$. Since the loading of the structure becomes non-proportional after $50 \mu\text{s}$ and the material model used in the current work takes only isotropic hardening into account, data after this instance was not used in the identification. The temporal development of the principal values $k_{1,2,3}$ of the Kirchhoff stress in Figure 3.9 shows that the loading becomes non-proportional after this instance. Note that k_2 (dash-dotted line) can be considered significantly smaller than k_1 and k_3 . This holds until $60 \mu\text{s}$. Likewise, the ratio of k_1 to k_3 remains approximately constant up to about $50 \mu\text{s}$. To indicate the degree of reproducibility for the input current as well as for the change of the radius their mean and standard deviation were computed and are shown in Figure 3.10. After characterization and selection of the experimental data, the calibration of the model was performed. In Table 3.5 the identified parameters are given for each of the 3 experiments conducted at 800 J. The left part of Figure 3.11 displays the radial expansion for the starting values of $\mathbf{p} = (100, 8)$,

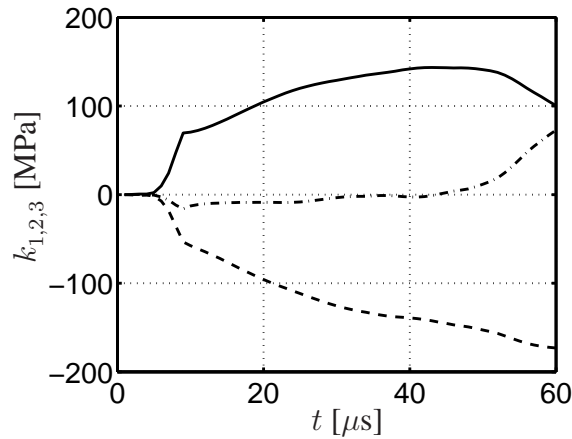


Figure 3.9: Loading path during electromagnetic tube forming. Left: Eigenvalues k_1 (solid line), k_2 (dash-dotted line) and k_3 (dashed line) of the Kirchhoff stress \mathbf{K} in the middle of the structure until $t = 60 \mu\text{s}$. Up to $t = 50 \mu\text{s}$, k_3/k_1 is approximately constant, and proportional loading prevails.

	Experiment 1	Experiment 2	Experiment 3
σ_0 [MPa]	5.91×10^1	5.82×10^1	5.41×10^1
m_0 [-]	2.41×10^0	2.55×10^0	2.80×10^0

Table 3.5: Identified dynamic viscoplastic material parameter values for $E_{cp} = 800 \text{ J}$ and $\gamma_0 = 6000 \text{ s}^{-1}$.

the identified values and the experimental data for Experiment 2. For validation purposes, the radial expansion was computed for the two remaining discharging energies based on the identified parameters. It can be seen that for $E_{cp} = 650 \text{ J}$, the simulation underestimates the actual deformation. This is in contrast to $E_{cp} = 1000 \text{ J}$, where the deformation is overestimated (see Figure 3.11 right). This discrepancy could be due to an insufficiently realistic material model. As is well-known, the rate contribution to the effective yield stress at low temperatures can be attributed to thermal activation of dislocation glide for low to moderate strain-rates (*i.e.*, $\dot{\epsilon}_p < 500 \text{ s}^{-1}$). For higher strain-rates (*i.e.*, $\dot{\epsilon}_p > 1000 \text{ s}^{-1}$), experiments exhibit a stronger rate sensitivity commonly attributed to the influence of drag forces (*e.g.*, Kocks and Mecking, 2003; Lindholm and Yeakley, 1964). Using the current model, the entire range of strain-rates can be covered with a reasonable degree of accuracy (see Figure 3.12) and only *two* parameters. This simplifies the identification significantly.

In the present situation, the fact that we are not taking the strain-rate dependence of the dynamic inelastic material parameters into account leads to the following behavior. The values obtained in Table 3.5 represent an experiment with a peak strain-rate of about $\dot{\epsilon}_p = 4200 \text{ s}^{-1}$. In the case of the experiment with a discharging energy of 1000 J , strain-rates up to $\dot{\epsilon}_p = 5900 \text{ s}^{-1}$ are achieved (see Figure 3.5). Since the strain-rate sensitivity increases with increasing strain-rate, the modeling of the 1000 J experiment with the parameters identified at 800 J underestimates the strain-rate sensitivity. Consequently, the deformation is overestimated. On the other hand, at 650 J , where a maximum strain-rate of about $\dot{\epsilon}_p = 3000 \text{ s}^{-1}$ is achieved, the parameter determination at 800 J leads to an overestimation of the strain-rate sensitivity. In this

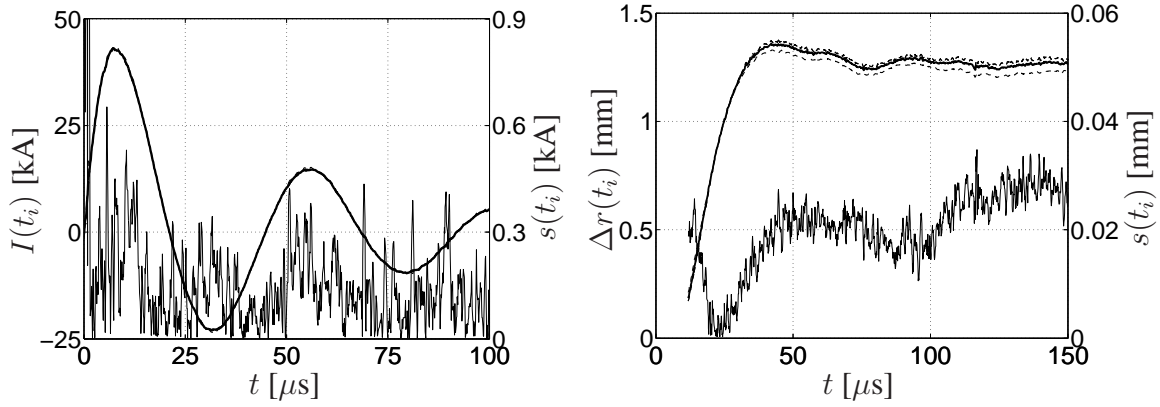


Figure 3.10: Characterization of reproducibility based on 3 experiments at a discharging energy of 800 J. Left: Input currents and their mean (hardly distinguishable from one another due to good match) and standard deviation $s(t_i)$ at each instance. Right: Corresponding radial change of tube for experiments (dashed lines), mean (solid line) and standard deviation $s(t_i)$ at each instance.

case, the deformation is underestimated. This is also reflected by the parameter values identified for the two remaining discharging energies. The expectedly higher strain-rate sensitivity for $E_{cp} = 1000$ J is rendered by $\sigma_0 = 71.2$ MPa and $m_0 = 2.3$. Conversely, for $E_{cp} = 650$ J the identification yields $\sigma_0 = 41.3$ and $m_0 = 2.7$. In this respect, the conclusion that γ_p , σ_p and m_p are in general functions of accumulated inelastic deformation and deformation rate (see Section 3.2) is confirmed. More detailed constitutive modeling represents work in progress.

Although the parameter values given in Table 3.5 are reasonable, there are a number of issues concerning the approximations built into the model and possible sources of experimental data or other errors worth mentioning. For example, possible convective effects on the magnetic field and Lorentz force involving the term $\text{curl}_s \mathbf{a} \times \mathbf{v}$ were neglected. Computations show that this results in a deviation of about 1%. In addition, any discretization errors are excluded for simplicity. Convergence studies in Stiemer et al. (2006a) imply that these are also quite small. In addition, simulation results seem to be quite insensitive to changes in the shape and position of the outer boundary, where homogeneous Dirichlet boundary conditions are assumed. The influence of the approximation of the tool coil by axisymmetric tori represents work in progress in the context of the extension of the simulation to 3D. Lastly, any influence of the temperature increase during the forming process on the material properties has been neglected here. Inclusion of the effects of Joule heating as well as heating due to inelastic dissipation yield a maximum local temperature rise of about 50 K at the inner surface of the tube. In other parts of the structure, the temperature rise is well below 20 K (Brosius, 2005). For Al, a temperature rise of 50 K is expected to result in a reduction of the yield stress of about 4% (see, *e.g.*, Bilyk et al., 2005). On the other hand, the deformation-rate sensitivity is expected to be one order of magnitude higher. Similar sensitivities apply to all other material parameters (*e.g.*, viscous properties, elastic material properties, mass density, etc.).

On the experimental side, errors in the geometry of the tube seem to represent the main source of error. Particularly due to the fact that the tubes are produced by an extrusion process, the geometry of the tube is unfortunately rather variable. The thickness of the tube varies,

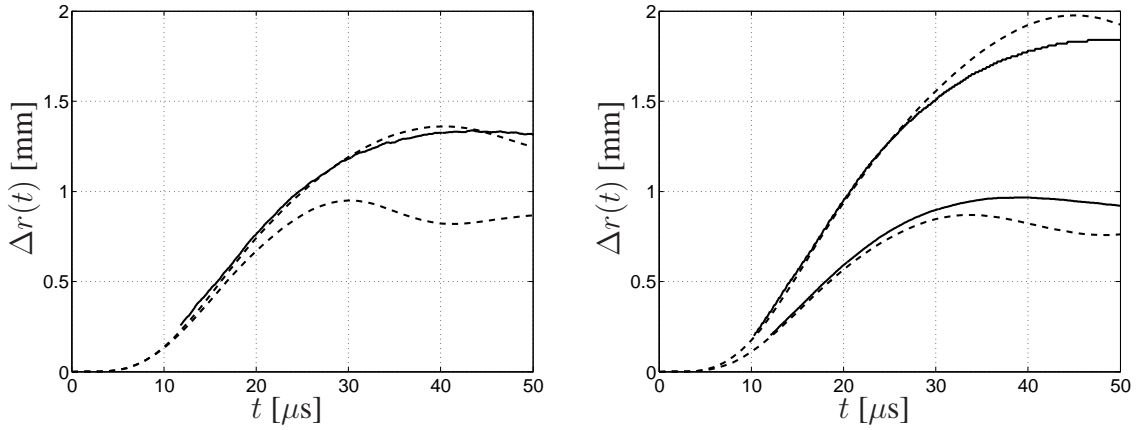


Figure 3.11: Parameter identification using experimental data. Left: Deviation of the radius computed with the initial vector of parameters (lower dashed line), identified parameters (dashed line) and measurements (solid line) Right: Modeling of remaining discharging energies (1000 J and 650 J) with identified material parameters (dashed lines) and corresponding experimental results (solid lines).

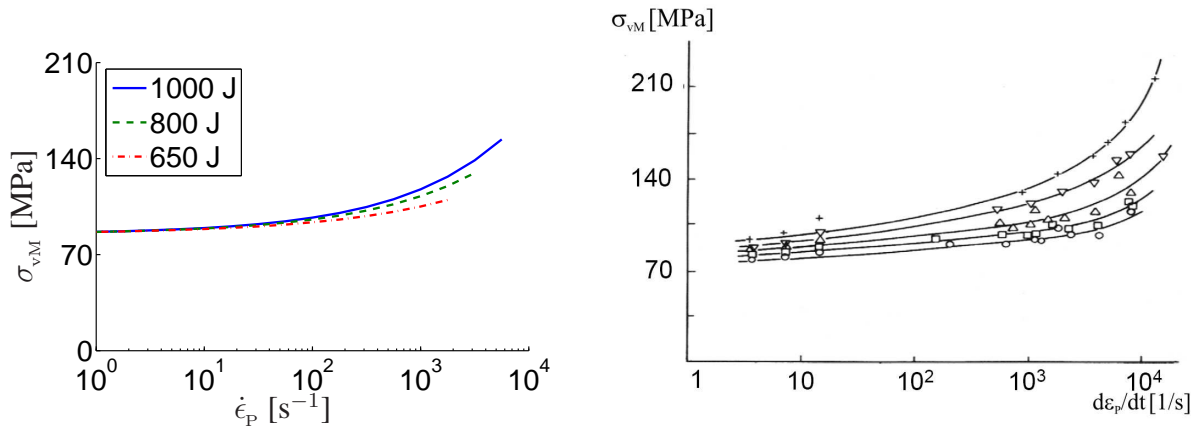


Figure 3.12: Left: Increase of effective yield stress with increasing strain-rate based on the identified model for each discharging energy ending at the corresponding maximum strain-rate. Right: Summary of experimentally determined increase of effective yield stress (Hopkinson bar) with increasing strain-rate taken from Hauser (1966).

affecting the stiffness of the structure. Secondly, deviations of the tube from being perfectly round result in additional deviations from the simulation. Regarding the measurement of the radial deviation with a PSD the degree to which the laser is distracted due to the geometry and surface of the tube needs to be evaluated. Some means to minimize such sources of error are discussed in Brosius (2005). Additional and less important sources of errors include the quasistatic inelastic material parameters, measured dimensions of the experimental setup, and measurement errors in the discharging current and tube displacement. In general, each of the discussed experimental sources of error accounts for deviations of the identified material parameters as has been discussed extensively above. Up to now, this has only been considered for the errors of the measured deviation of the radius. A full evaluation and quantification of

sources of error and the determination of variances for the parameters determined in Table 3.5 represents work in progress.

3.7 Conclusions

In the theoretical discussion of the methods for model identification it could be shown that the finite element inverse method can be extended with methods common to statistical model identification like correlation-, sensitivity- and error- analysis. Such methods are important since they offer measures for the reliability of the identified data. The incorporation of these into the inverse analysis as well as their validation could be demonstrated in the context of high strain-rate identification with electromagnetic forming. Moreover, it could be shown that the identification of the constitutive parameters can be simplified in a particular way. In contrast to a dependence on changes in geometry, which are fully considered, there exists very little sensitivity of the material model parameters to the sharp increase in the electromagnetic loading at the beginning of the process. This is the case since the structure deforms predominantly elastically at the beginning. It is just this situation that allows for the identification procedure at stepwise fixed electromagnetic loads.

The material parameters identified with real experimental data indicated a reasonable modeling of the electromagnetic forming operation. However, deviations to experimental results suggest that the ansatz chosen represents a relatively rough approximation regarding the wide range of strain-rates the model has to cover. Yet, for the actual identification procedure this simplicity represents a great advantage and allows for detailed insight. In this work, the measurement of the radial expansion of the tube was the focus of attention in regards to error analysis. In work in progress, additional aspects of the measurement process are being investigated, and will be reported on in future work.

Chapter 4

Strategies for 3D simulation of electromagnetic forming processes*

Abstract – Although electromagnetic forming is a technology known for a few decades, renewed interest for its industrial application is currently taking place. Along with this interest an increasing demand for simulation tools can be found. Up to now, modeling approaches found for this process in the literature are restricted to the axisymmetric case or small deformation problems. However, for real industrial applications, the modeling of large deformation 3D forming operations becomes crucial for an effective process design. On the basis of previous modeling concepts in the work at hand we develop and investigate further approaches particularly suitable to reduce the enormous computational cost inherent to 3D simulations. These consist of a carefully chosen discretization, a data transfer method for both, the electromagnetic loads and the mechanical deformation to utilize an efficient solid shell formulation and a termination criterion for the electromagnetic part of the model. As a result the simulation time is reduced by about one order of magnitude. Finally, a 3D forming setup is modeled and detailed insights with respect to the development of eddy currents, magnetic field and deformation of the sheet metal are provided.

4.1 Introduction

Electromagnetic forming (EMF) is a dynamic, high strain-rate forming method in which strain-rates of up to 10^4 s^{-1} are achieved. In this process, deformation of the workpiece is driven by the interaction of a current generated in the workpiece with a magnetic field generated by a coil adjacent to it. In particular, this interaction results in a material body force, i.e., the Lorentz force and the electromotive power, representing an additional supply of momentum and energy to the material. On the other hand the electromagnetic part of the system is sensitively influenced by the spatio-temporal evolution of the deformation of the mechanical structure. With increasing interest in this forming operation, in recent years considerable effort has been made to simulate such coupled processes. However, approaches tested so far were mainly restricted to axisymmetric geometries (Fenton and Daehn, 1998; Gourdin et al., 1989; Imbert et al., 2004; Oliveira et al., 2001; Takatsu et al., 1988) or to small deformation problems (Schinnerl et al., 2002). Yet, it is the 3D modeling capability in combination with the large inelastic deformations that is required to advance effectively in the design of industrial EMF processes. To meet these modeling requirements the sound derivation of a physical model of the relevant magneto-mechanical phenomena has been developed in Svendsen and Chanda (2005). Its algorithmic realization is given in Stiemer et al. (2006a) and Stiemer et al. (2006b).

For axisymmetric modeling, nowadays PC computational capacities are sufficient to model

*Unger et al. (2007b, 2006a)

forming operations within several hours. As it turns out, in the case of 3D process models the computational cost increases dramatically. While typical 2D models of EMF in general exhibit a model size of between about 3 000 and 10 000 degrees of freedom similar 3D models usually require discretizations with an extent of a model which is one order of magnitude higher. It is the goal of the present work to elaborate and demonstrate approaches particularly suitable to reduce the computational cost for the 3D modeling of EMF processes in the aforementioned context. In detail these represent an extensive study of convergence, the proposal of a body force and deformation data transfer method which facilitates the use of solid shell elements (Reese, 2007) and the development and elaboration of a termination criterion for the electromagnetic part of the model. These measures are demonstrated by means of a relatively simple forming setup. Although this presented forming setup geometry is rather exceptional (see figures 4.1 and 4.2), dimensions and timescales are relevant for typical forming setups. As elaborated below, since the results are general in nature they can be transferred to other forming setups.

After a brief summary of the physical model and its algorithmic formulation (see Section 4.2) the study of convergence is discussed in sections 4.3 and 4.5. Here, the study allows for the exploitation of potential for reduction of the computation time by selectively choosing a coarse discretization at locations where this is admissible according to the scope of the desired accuracy. Further, by studying the convergence of certain components of the EMF forming setup (*e.g.*, tool coil, sheet metal, air gap, etc.) further physical insight is provided and the algorithmic model can be verified. In Section 4.4 the data transfer between the electromagnetic and the mechanical part of the model is discussed. In contrast to 2D modeling of EMF where the electromagnetic loads are transferred elementwise, here an independent discretization of the sheet metal is facilitated. Here, we exploit the fact that the electromagnetic loads are algorithmically independent of the mechanical deformation in the context of the staggered solution algorithm and can be integrated separately. In consequence, the use of a very efficient solid shell element formulation for the mechanical part of the model becomes feasible. In Section 4.6 a termination criterion particularly suitable for an efficient modeling of EMF processes is proposed and evaluated. In Section 4.8 a fully coupled forming operation where all the aforementioned approaches were implemented is performed and the results are discussed. The work is concluded in Section 4.9.

4.2 Synopsis of model formulation and description of forming setup

The coupled multifield model for electromagnetic forming of interest represents a special case of the general continuum thermodynamic formulation for inelastic non-polarizable and non-magnetizable materials given in Svendsen and Chanda (2005), where a full elaboration of this model can be found. In summary, this special case is based on the quasi-static approximation to Maxwell's equations, in which the wave character of the electromagnetic (EM) fields is neglected. In this case, the unknown fields of interest are the motion field ξ , the scalar potential χ and the vector potential \mathbf{a} determining in particular the magnetic field in the usual fashion (Jackson, 1975). Assuming Dirichlet boundary conditions for all fields, one derives the weak

field relations

$$\begin{aligned}
0 &= \int_{B_r} (\varrho_r \ddot{\boldsymbol{\xi}} - \mathbf{l}_r) \cdot \boldsymbol{\xi}_* + \mathbf{K} \mathbf{F}^{-T} \cdot \nabla \boldsymbol{\xi}_* , \\
0 &= \int_R \{ \dot{\mathbf{a}} + \mathbf{L}^T \mathbf{a} \} \cdot \mathbf{a}_* + \int_R (\chi - \mathbf{a} \cdot \mathbf{v}) \operatorname{div} \mathbf{a}_* + \kappa_{\text{EM}} \operatorname{curl} \mathbf{a} \cdot \operatorname{curl} \mathbf{a}_* , \\
0 &= \int_R \nabla \chi \cdot \nabla \chi_* ,
\end{aligned} \tag{4.1}$$

for $\boldsymbol{\xi}$, \mathbf{a} , and χ , respectively. Here, $\boldsymbol{\xi}_*$, \mathbf{a}_* , and χ_* represent the corresponding test fields. Further, R represents a fixed region in Euclidean point space containing the system under consideration in which the electromagnetic fields exist and on whose boundary the boundary conditions for these fields are specified. Here, the system comprises the sheet metal consisting of the aluminum alloy AA 6060, the tool coil consisting of technically pure copper and air (see Figure 4.1). Electromagnetic and mechanical material properties of the system can be found in Unger et al. (2007a). The setup has a width and a depth of 60 mm and a height of 7 mm. Both, the air gap between the sheet metal and the tool coil and the thickness of the sheet metal measure 1 mm. The height of the tool coil measures 5 mm and each winding has a width of 20 mm.

As indicated in Figure 4.1, R contains in particular the fixed reference configuration B_r , and all subsequent (*i.e.*, deformed) configurations of the workpiece. Note that $\mathbf{F} := \nabla \boldsymbol{\xi}$ represents the deformation gradient, and $\mathbf{L} := \nabla \mathbf{v}$ the spatial velocity gradient. Further, κ_{EM} represents the magnetic diffusivity, \mathbf{v} the spatial velocity field, ϱ_r the referential mass density, \mathbf{K} the Kirchhoff stress, and $\mathbf{l}_r = \det(\mathbf{F}) \mathbf{j} \times \mathbf{b}$ the Lorentz force in terms of the magnetic flux \mathbf{b} and the current density \mathbf{j} . As usual, \mathbf{a} and χ determine the magnetic flux via $\mathbf{b} = \operatorname{curl} \mathbf{a}$ and the electric field via $-\mathbf{e} = \partial \mathbf{a} + \nabla_s \chi$. Given that the electromagnetic fields vary on a timescale much shorter than that of the mechanical fields, the convective contribution to \mathbf{j} is neglected here yielding $\mathbf{j} = \sigma_{\text{EM}} \mathbf{e}$ via Ohm's law. Note that (4.1)_{2,3} follow from Maxwell's equations, while (4.1)₁ represents the weak form of momentum balance. The above weak field relations are completed by the thermodynamically consistent formulation of the elasto-viscoplastic material model (Svendsen and Chanda, 2005).

As indicated in Figure 4.1 the sheet metal is fixed at its lateral edges representing the mechanical Dirichlet boundary conditions. For the tool coil the eddy current contribution to the current density is neglected. This facilitates the direct implementation of the measured input current I as a Neumann boundary condition via $\mathbf{j} = -\sigma_{\text{EM}} \nabla_s \chi$, where $\mathbf{j} = (0, -I/A_{\text{con}}, 0)$. Here, A_{con} represents the area of the surface connecting the tool coil to the capacitor bank that provides the energy for the forming operation. The other connection surface is grounded ($\chi = 0$). For the remaining surfaces $\nabla_s \chi \cdot \mathbf{n} = 0$ is postulated meaning that no electric current leaves the coil through any surface but the connection surfaces. Since the deformation of the sheet metal and thus the correct modeling of the electromagnetic loading represents the main concern in this work the effects of the eddy currents within the tool coil can be neglected. As a consequence the current density distribution can be assumed to be homogeneous in the cross section of the tool coil (*e.g.*, no skin effects). In other words, the effect of the eddy currents in the tool coil on the magnetic field strength outside the coil and in particular in the sheet metal is negligible since the total current I is considered correct. An additional assumption refers

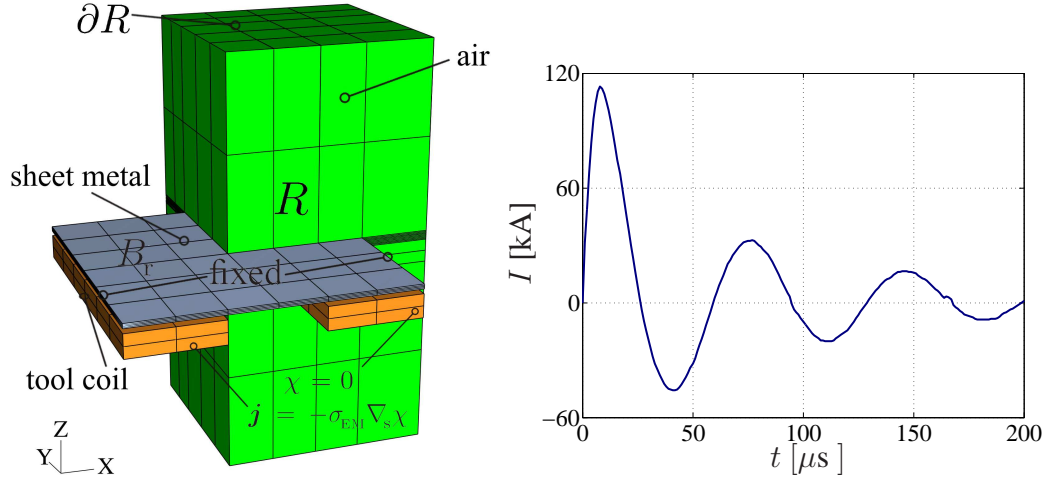


Figure 4.1: Illustration of forming setup including tool coil, sheet metal, air and annotation of the entire domain of the system R , its boundary ∂R and the mechanical domain B_r . At ∂R homogeneous Dirichlet boundary conditions are assumed. The experimentally measured input current is implemented as a Neumann boundary condition for χ , where $\mathbf{j} = -\sigma_{EM} \nabla_s \chi = (0, -I/A_{con}, 0)$. Regarding the mechanical component of the model, the lateral edges of the sheet metal are fixed.

to the sheet metal. Here the physical constraint $\mathbf{j} \cdot \mathbf{n} = 0$ is not considered. Since tool coils utilized for EMF generally induce circular eddy currents, the error made by this assumption can be regarded to be small.

Consider next the algorithmic realization of the aforementioned model in terms of the finite element discretization of (4.1). In more detail this is discussed in Stiemer et al. (2006a,b). The difference in electromagnetic and thermomechanical timescales together with the distinct nature of the fields involved (*i.e.*, Eulerian in the electromagnetic case, Lagrangian in the thermomechanical large deformation context), argue for a staggered numerical solution procedure resulting in the following algorithmic system:

$$\begin{aligned} \mathbf{f}_{n+1,n}(\mathbf{x}_{n+1}, \mathbf{a}_{n+1}) &= \mathbf{0}, \\ \mathbf{e}_{n+1,n}(\mathbf{x}_{n+1}, \mathbf{a}_{n+1}) &= \mathbf{0}, \end{aligned} \quad (4.2)$$

in terms of the arrays \mathbf{x}_{n+1} and \mathbf{a}_{n+1} of time-dependent system nodal positions and vector potential values at time increment t_{n+1} . The solution of the mechanical part of (4.2) involves in particular the consistent linearization required for the Newton-Raphson iteration in the context of large deformation inelastic problems. In detail, the staggered algorithm procedure consists of the following steps:

1. Initialize \mathbf{a}_0 , \mathbf{x}_0 and their time derivatives and proceed to (4).
2. A starting value \mathbf{a}_{n+1} of the nodal vector potential array is computed for the measured amperage in the tool coil at time t_{n+1} and the known mechanical state of the system at time t_n via (4.2)₂.
3. From \mathbf{a}_{n+1} , a corresponding value I_{n+1} for the Lorentz force is obtained. Using this, the

system consisting of (4.2)₁ is solved via Newton-Raphson iteration (*i.e.*, at fixed \mathbf{a}_{n+1}) to obtain \mathbf{x}_{n+1} .

4. Proceed to next time step $t_{n+1} = t_n + t_{n+1,n}$ and proceed with (2). Else, if $t_n \geq t_s$, terminate the simulation, where t_s is the total simulation time.

Besides the physical motivation the staggered algorithm offers the possibility to apply custom solutions for both, the mechanical as well as the electromagnetic system. Here, on the mechanical side, an effective continuum shell formulation is applied to minimize the computational effort Reese (2007) for the mechanical model. On the electromagnetic side, in contrast to the axisymmetric case, the Coulomb gauge condition is generally not satisfied and the electromagnetic fields are not regular for standard boundary conditions. To ensure that the corresponding finite element solution reflects this lack of smoothness, a penalty method or a least-squares approach is required. In the simulation presented here, Nédélec elements (Nédélec, 1986) are employed to overcome this difficulty. These are based on averaged degrees of freedom with respect to the element edges instead of discrete degrees-of-freedom at the element nodes.

4.3 Study of convergence of the electromagnetic model at fixed sheet metal

Since this is mainly an electromagnetic issue, the deformation of the sheet metal was suppressed in order to facilitate an easy and effective study of all mesh parameters. The simulation was performed until $t = 8 \mu\text{s}$, where the maximum input current is imposed and a time step of $t_{n+1,n} = 2 \mu\text{s}$ was chosen. In spite of simulating the entire process time, the magnetic flux and eddy current distribution were evaluated at $t = 8 \mu\text{s}$ in order to be able to deal with large models at reasonable simulation times. Particular attention is given to the modeling of the fields in the sheet metal. An accurate modeling in this regard accounts for accurate modeling of the forming operation. In Figure 4.2 three paths, denoted with PX, PY and PZ are depicted. Along these a quantitative investigation of the magnetic flux density and eddy currents was performed. The paths along the x - and y -axis are located in the *midplane* of the sheet metal and the path along the z -axis passes through the center of the left part of the coil and the sheet metal. For these paths, only the most significant component b_x of \mathbf{b} and j_y of the eddy current field \mathbf{j} are considered (see figures 4.27 and 4.28 in Section 4.8). Along with the results obtained from the path plots the values of

1. b_x at the lower surface of the sheet metal, denoted by \tilde{b}_x and
2. j_y at the same location, denoted by \tilde{j}_y

from the path in vertical direction serve as concrete quantities to measure the dependence of the solution on a chosen mesh parameter. These indicators of convergence are characteristic for the development of the electromagnetic fields in the sheet metal, since they represent the largest values in the sheet during the first alternation of the tool coil current and thus characterize the forming operation. The study of convergence involves the discretization of particular mesh parameters. They involve the size of the outer boundary of the electromagnetic domain, the number of elements along the x or y -direction and several mesh parameters that characterize

the discretization in vertical direction. The most effective way is to investigate those parameters first, which exhibit the most significant influence on the computational cost. For the study of some mesh parameter n , $\tilde{b}_x(n)$ and $\tilde{j}_y(n)$ are in general normalized by the results obtained for the finest discretization obtained for the maximal value of n . This indicates the relative deviation and relative sensitivity, which is more meaningful in comparison to the absolute values of $\tilde{b}_x(n)$ and $\tilde{j}_y(n)$.

4.3.1 Influence of the size of outer boundary of the electromagnetic domain

From an abstract point of view the EMF setup can be seen as two coupled antennas representing a magnetic quadrupole. Here, the two antennas consists of the EMF tool (capacitor bank and tool coil) and the sheet metal. In communications engineering it is very important to be able to predict the far field solution for, *e.g.*, antenna design. In this case the radiating fields are successfully predicted with boundary element methods (Poljak et al., 2006). For the simulation of EMF however, the magnetic near field is significant. As the near field of the flux density of a magnetic quadrupole decays like $O(|x|^{-4})$ it is admissible to assume homogeneous Dirichlet boundary conditions at some boundary ∂R to good accuracy. It is the subject of this section to investigate the influence of the distance of the boundary ∂R from the forming setup with respect to the magnetic flux density.

The box determined by ∂R is commonly referred to as the bounding box. Clearly, the smallest size of such a bounding box is determined by the size of the forming setup. In this respect, in what follows the parameter d denotes the distance from the forming setup in x - and y -direction. Three values of d , namely $d = 15$ mm, $d = 30$ mm and $d = 60$ mm, are examined. The height of the box is kept fixed at 90 mm corresponding to a distance of 45 mm above the sheet metal and 38 mm below the tool coil. Above the sheet metal the magnetic flux density is very small due to its shielding effect (see Section 4.8 for further details). Here, the choice of the boundary is hardly significant (see Section 4.3.3). However, some space is to be reserved to account for the deformation of the workpiece. For the volume below the tool coil the findings for the lateral

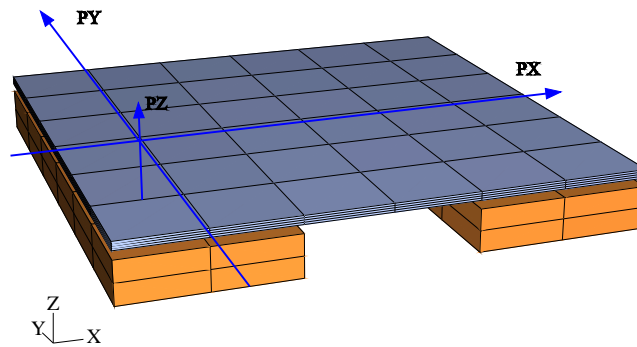


Figure 4.2: Forming setup with illustration of evaluation paths denoted by PX, PY and PZ. These proceed in horizontal and vertical direction. Horizontal paths are located in the midplane of the sheet metal.

boundary can be carried forward. It is advisable to evaluate the influence of the size of such a bounding box at the beginning of the study of convergence. This parameter is significant for the reduction of the computational cost. A well chosen size for the bounding box allows for higher levels of refinement regarding other mesh parameters.

At this point it is important to note that the field values at the border of the bounding box depend on the refinement of the mesh. For a proper study of the effect of d on the field values, a sufficiently refined mesh should be chosen. To indicate this the study was conducted with two different levels of mesh refinement along the x - and y -direction, one with element edge lengths of $h_x = h_y = 10$ mm and one with $h_x = h_y = 5$ mm. The refinement in vertical direction is kept constant at its finest value (see Section 4.3.3 for further details). In figures 4.3 and 4.4 detailed insight into the aforementioned influence of the discretization on the size of the bounding box is given. Considering b_x along PX in Figure 4.3 for $h_x = h_y = 10$ mm it can be seen that the rough discretization leads to a considerable overestimation of the magnetic flux density at the boundary. For $d = 15$ mm and $h_x = h_y = 5$ mm however, the magnetic field is significantly decayed. Here, an extension of the bounding box has a minor effect on \mathbf{b} inside the sheet metal.

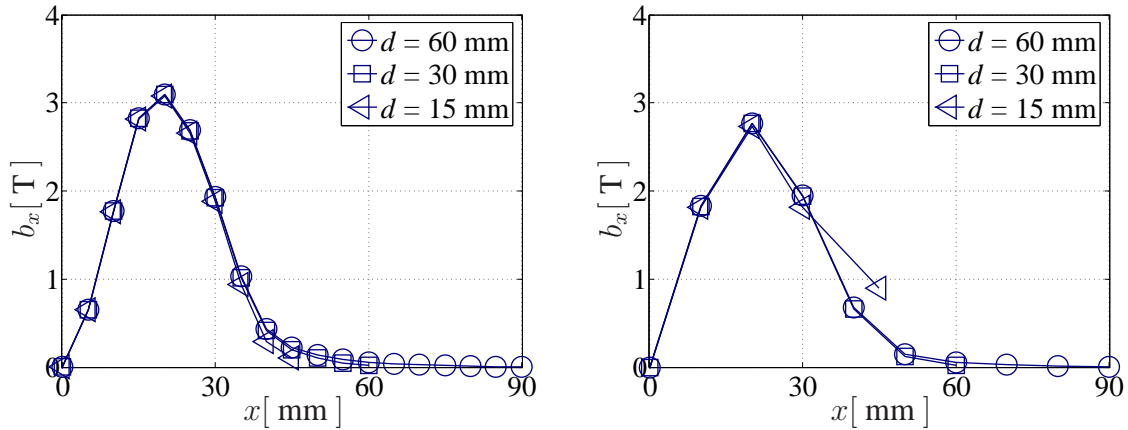


Figure 4.3: The component b_x of the magnetic flux density along the path parallel to the x -axis (see Figure 4.2) for different sizes of the bounding box and two levels of mesh refinement $h_x = h_y = 5$ mm (left) and $h_x = h_y = 10$ mm (right).

The comparison of the convergence indicators \tilde{b}_x and \tilde{j}_y for both meshes is shown in Figure 4.4. To indicate the above discussed relative deviation between the most accurate model, \tilde{b}_x and \tilde{j}_y are normalized by $\tilde{b}_x(d = 60)$ and $\tilde{j}_y(d = 60)$, respectively. For the refined mesh the smallest bounding box with $d = 15$ mm leads to an underestimation of the fields of about 1 %. For the coarse one an underestimation of about 7 % is observed.

Regarding the desired accuracy, $d = 15$ mm seems to be acceptable and is chosen for the following studies. Also the number of elements in the space between the bounding box and the forming setup was chosen such that the decay of the magnetic flux density can be resolved. This results in 3 elements for the space between the forming setup and the bounding box, corresponding to $h_x = h_y = 5$ mm in the above study.

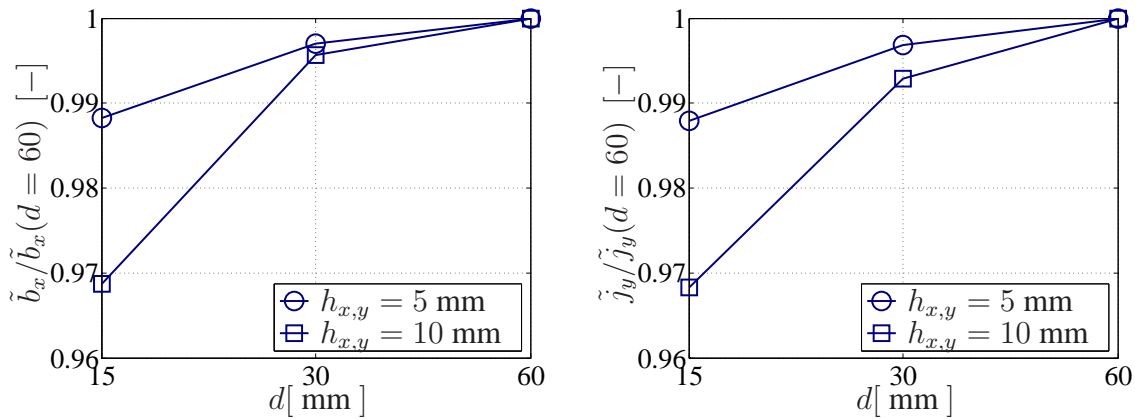


Figure 4.4: Study of the influence of the of the bounding box size for \tilde{b}_x and \tilde{j}_y for two levels of mesh refinement.

4.3.2 Refinement of horizontal mesh parameters

The determination of the size of the bounding box size resulted in a reduction of the total number of elements at acceptable modeling error levels (for details see Table 4.1). The smaller extent of the model now facilitates a higher refinement for the subsequent study of convergence of the electromagnetic mesh. The objective here is to start with the model with the finest mesh and successively reduce the refinement along the x - or y -direction in order to test the influence on the magnetic field and eddy current distribution in the sheet metal in comparison to the most refined and most accurate model. Here, the mesh parameter n_x denotes the number of elements in x -direction and n_y the number of elements in y -direction. For n_x and n_y , values of 6, 12 and 24 were tested. They correspond to an element edge length of 10, 5 and 2.5 mm in each direction. Due to the construction method of the mesh, its topology in the xy -plane holds along the z -axis and thus influences the refinement of all vertical regions (Schmaling and Unger, 2007). As in the case of the choice of the size of the outer boundary, the refinement in the xy -plane has a significant influence on the total number of elements.

Since n_x and n_y directly affect the discretization and field distribution in the sheet metal, their influence is studied with respect to PX, PY and PZ. The distribution of b_x along PZ indicates that the sensitivity of the discretization with respect to the x -direction is higher than in the y -direction (see Figure 4.5). For $n_x = 6$ the magnetic flux density is reduced by about 13 % while for $n_y = 6$ a reduction of 1 % can be observed (see Figure 4.7). The reason for the smaller influence of n_y on the field values can be attributed to the geometry of the tool coil. Two conductors of the tool coil are parallel to the y -axis and only the rear part of the coil is parallel to the x -axis. Via Ampere's law changes of \mathbf{b} are expected to occur *perpendicular* to the conductor which is mainly orientated along the y -axis here (see also 4.27). Consequently it is reasonable that a higher amount of elements in the x -direction is required to resolve these field changes. In more detail in the left part of Figure 4.6 the distribution of b_y in x -direction is shown, the high sensitivity of the magnetic field distribution to n_x can be confirmed. Conversely, the weak sensitivity to n_y is indicated for the eddy current distribution j_y in y -direction. Only for $y > 45$ mm where the eddy currents change their direction according to the electric field induced by the tool coil (see figures 4.28 and 4.26) significant deviations can be observed. In

Figure 4.7 the study of convergence for n_x and n_y is summarized again with respect to the indicators of convergence confirming the above considerations.

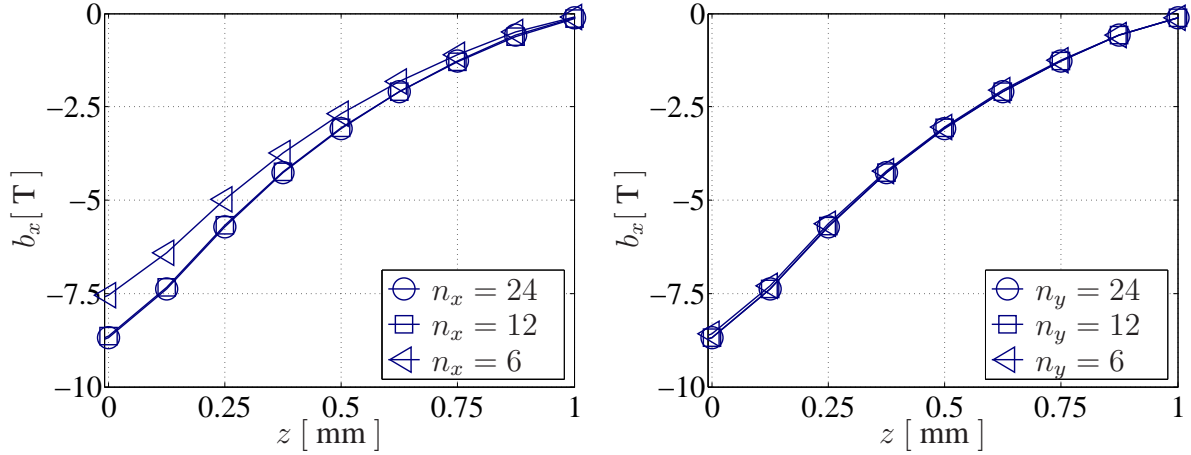


Figure 4.5: The component b_x along PZ for different values of n_x (left) and n_y (right). The results exhibit a stronger sensitivity to n_x than to n_y .

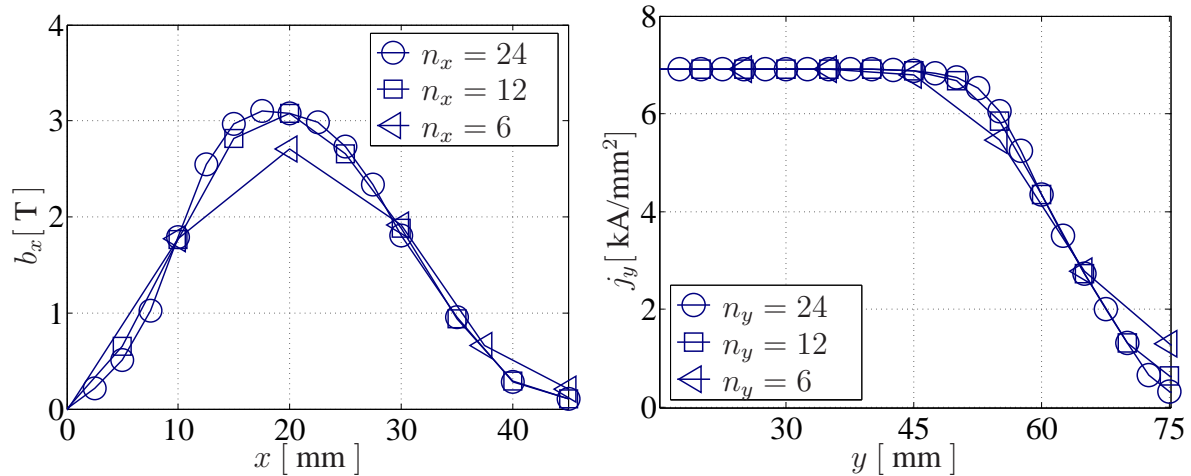


Figure 4.6: Illustration of the different sensitivities of the field results to n_x and n_y . Left: b_x along PX for different values of n_x . Right: j_y along PY for different values of n_y .

Considering the study depicted in 4.7 $n_x = 24$ and $n_y = 12$ represent a good reduction at relatively small discretization errors. It has to be noted that in contrast to the vertical mesh parameters and the size of the bounding box the mesh topology in horizontal direction affects the mesh of the mechanical part of the model (Schmaling and Unger, 2007). Here, for the horizontal mesh refinement of the mechanical mesh denoted by n_{mx} and n_{my} , $n_x \geq n_{mx}$ and $n_y \geq n_{my}$ have to hold. However, the choice of $n_x = 24$ and $n_y = 12$ corresponds well with the results of the mechanical study of convergence (see figures 4.22 and 4.23 in Section 4.5) and is therefore kept for subsequent computations.

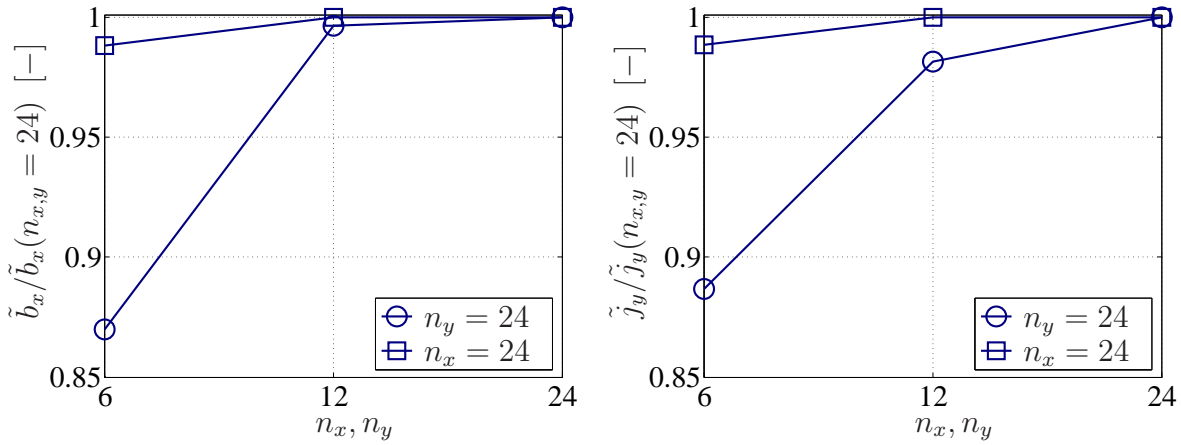


Figure 4.7: Study of convergence for the mesh refinement in horizontal x and y -direction for the convergence indicators \tilde{b}_x and \tilde{j}_y . Circles indicate the mesh refinement in x -direction at finest discretization in y -direction ($n_y = 24$) and squares indicate the mesh refinement in y -direction at finest discretization in x -direction ($n_x = 24$).

4.3.3 Refinement of vertical mesh parameters

As mentioned above, the forming setup can be divided into five regions of mesh refinement in vertical direction. These represent:

1. the air above the forming setup characterized by the number of element layers above the setup, denoted by n_{aa} ,
2. the air below the forming setup characterized by the number of element layers below the setup, denoted by n_{ab} ,
3. the number of element layers in the air gap between the tool coil and the sheet, denoted by n_{ag} ,
4. the vertical layers of the mesh which contain the tool coil, denoted by the parameter n_{tc} , and
5. the number of element layers in the sheet metal denoted by n_{sm} .

In Figure 4.8 these layers are illustrated for the present forming setup. We start here with the investigation of the parameters n_{aa} , n_{ag} and n_{tc} since these exhibit only a very small influence on \mathbf{b} and \mathbf{j} and can be treated in conjunction. In Figure 4.9 the distributions of b_x and j_y in thickness direction of the sheet along the path PZ are depicted for the *finest* mesh in vertical direction, indicated by crosses. Additionally, the mesh distributions where one of the aforementioned parameters was set to its *coarsest* value are depicted. As can be seen, the deviations turn out to be very small. In Figure 4.10 the normalized deviations for \tilde{b}_x and \tilde{j}_y are shown in more detail. The largest deviation can be observed for $n_{aa} = 1$ and is well below 1 % in comparison to the finest discretization with $n_{aa} = 8$. Note that $n_{aa} = 8$ is equivalent to $n_{ab} = 8$, $n_{tc} = 8$ and $n_{ag} = 8$, since only one parameter is changed at a time while the others were kept at their finest discretization. The physical reasons for these distinct insensitivities are explained in what

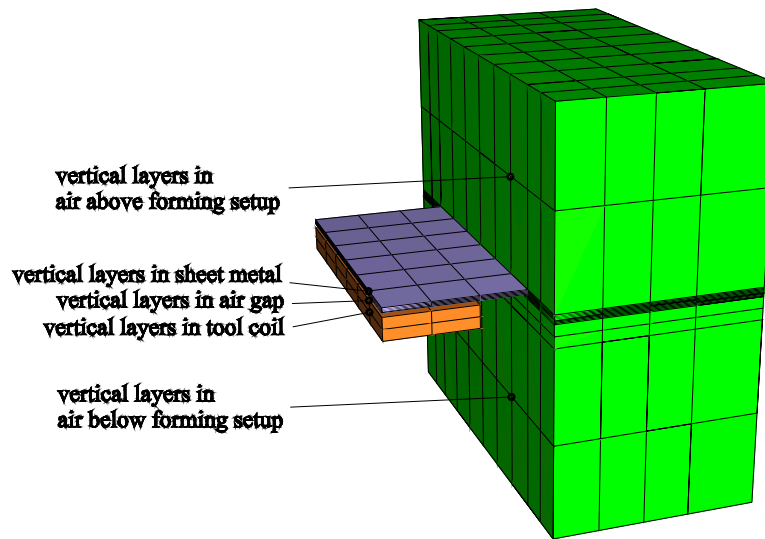


Figure 4.8: Illustration of vertical mesh parameters. Each characteristic mesh entity was attributed to a particular mesh parameter which is utilized for a selective study of convergence.

follows. In Figure 4.11 the vertical distribution of b_x along Path PZ is depicted. Moreover, the location of the tool coil and the sheet metal are indicated to be able to relate the distribution to the particular components of the forming setup. Due to the fact that eddy currents are neglected for the tool coil (see Section 4.2) a linear distribution can be observed inside the coil. From a qualitative point of view this is consistent with the outcome of analytical models for simple conductors at low frequencies (Jackson, 1975). In the air gap a homogeneous magnetic flux density can be observed, which is again coherent with results from axisymmetric and analytic models for similar EMF forming setups (Beerwald, 2004; Mamalis et al., 2004). In accordance with the character of the parabolic field equation inside the sheet metal the interaction between the eddy currents within the sheet are such that the magnitude of the magnetic field decays and is reduced to a value several orders of magnitude smaller than its maximum value. In more detail this is discussed in Section 4.8. These characteristics are crucial for the study of convergence of the vertical mesh parameters. Due to the nature of the finite element approximation the roughly *linear* field distribution in the tool coil can easily be rendered by a small number of vertical element layers (e.g., $n_{tc} = 2$). Similarly, in the case of the air gap, where an approximately homogenous field distribution prevails, again only few layers are sufficient (e.g. $n_{ag} = 2$). Regarding the upper air, one expects that more elements would be necessary since the magnetic flux density decays non-linearly just as in other parts of the surrounding air. However, it has to be noted that the magnetic flux density is only a fraction of its maximum value due to the shielding effect of the sheet metal. Even if the approximation of the field distribution in the air above the sheet metal is very rough, the field distribution *inside* the sheet metal remains unaffected due to the fact that field values are so small in this region that any approximation error has little influence here.

Next, we turn to the discretization of the sheet metal. If the accurate modeling of the deformation and forming of the sheet metal represents the key modeling objective, an accurate

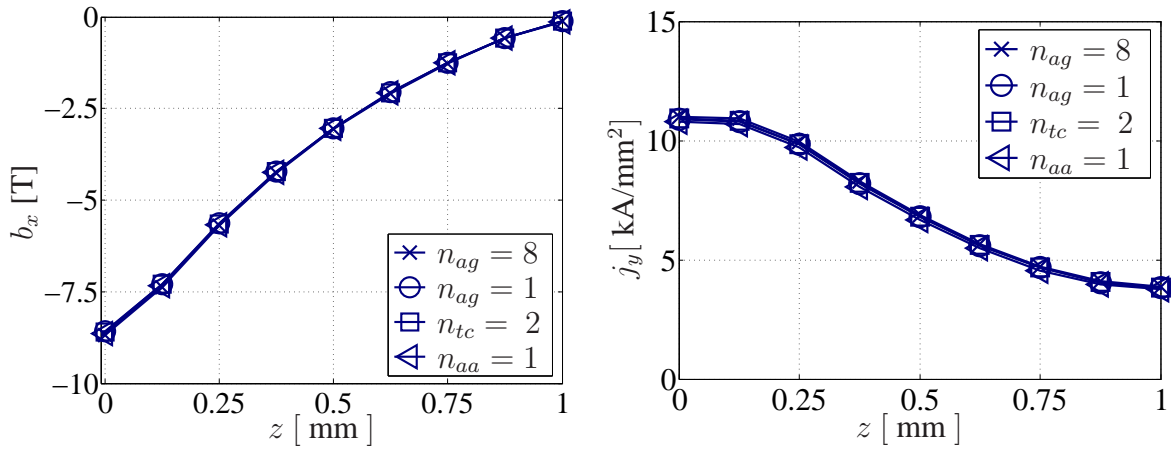


Figure 4.9: The component b_x of the magnetic flux density and current flux density j_y along the sheet thickness (see Figure 4.2, Path PZ). Each curve represents the solution for the coarsest possible discretization in a specific vertical layer. The value $n_{ag} = 8$ corresponds to the finest mesh and is equivalent to $n_{tc} = 8$, $n_{ag} = 8$ and $n_{aa} = 8$ since only one mesh parameter is refined at a time.

representation of the Lorentz forces in the sheet metal is fundamental (see also Section 4.4). While the magnetic field distribution is linear or constant in the tool coil and air gap, the electromagnetic fields decay is highly non-linear in the sheet metal. As shown in Section 4.8 in Figure 4.30 according to the electric field induced by the tool coil current, the eddy current distribution in the sheet metal is very variable. It is expected that the results for \mathbf{b} and \mathbf{j} converge for high values of n_{sm} only. This is confirmed by the study of convergence for this parameter (see figures 4.12 and 4.13).

Finally, we turn to the last vertical mesh parameter n_{ab} . As it turns out, the number of element layers for the air below the forming setup has a significantly stronger influence on the field distribution in the sheet metal than those for the air above the forming setup. In contrast to the air above the forming setup the magnetic field penetrates the air below the forming setup freely and at some distance from the forming setup the magnetic field is still significant. In return, for the lower part of the forming setup, the discretization influences the electromagnetic fields in the sheet metal. This is also confirmed by the study of convergence for the mesh parameter n_{ab} . Therefore, as shown in Figure 4.13, \tilde{b}_x and \tilde{j}_y are much more sensitive to the discretization of the lower air than to the one of the upper air (see Figure 4.9).

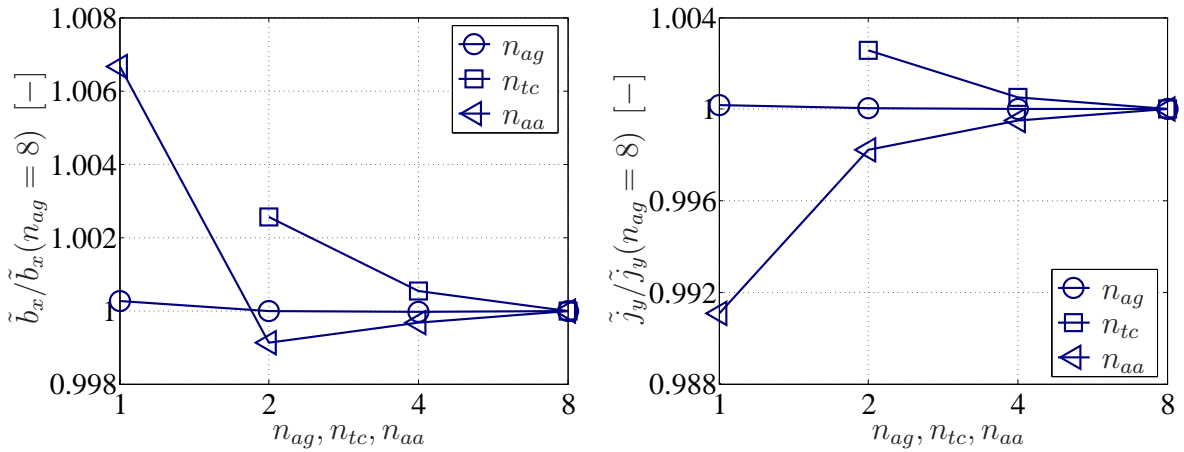


Figure 4.10: Convergence of \tilde{b}_x and \tilde{j}_y normalized by the most refined result. For the tool coil $n_{tc} = 1$ is inexpedient since this excludes unconstrained nodal components for the scalar potential χ .

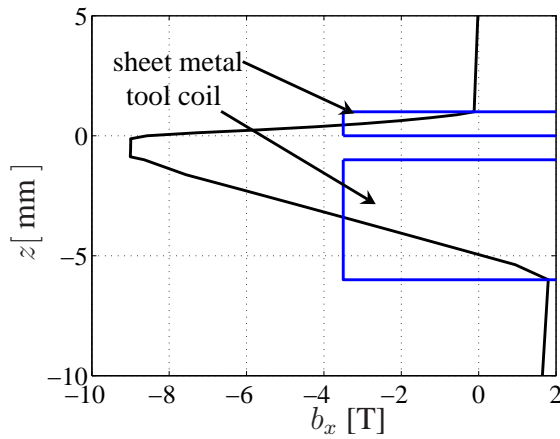


Figure 4.11: Illustration of vertical field distribution along Path PZ to indicate field distributions in particular features of the EMF setup.

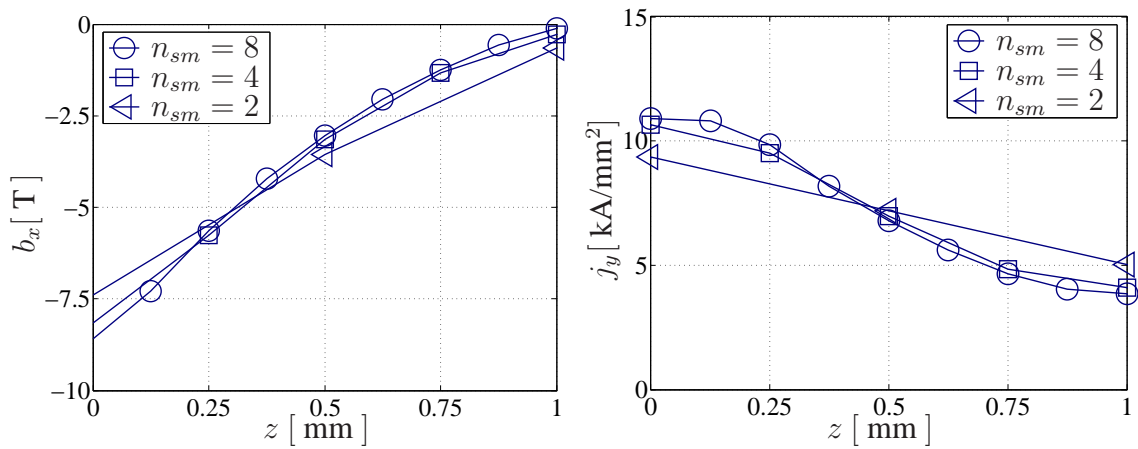


Figure 4.12: Study of convergence of b_x and j_y for the number of element layers in the sheet metal along Path PZ.

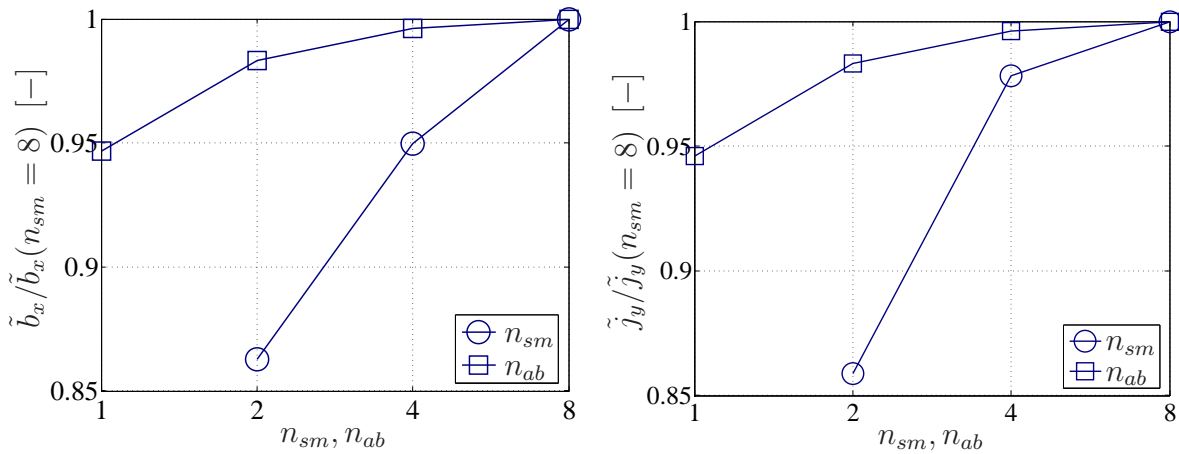


Figure 4.13: Convergence of \tilde{b}_x and \tilde{j}_y normalized by the most refined result. The strong sensitivity of the results to n_{sm} is evident.

4.4 Mesh adaption and body force data transfer for solid shell elements

In the case of a staggered approach the solution of the coupled system is achieved on two meshes. In Stiemer et al. (2006a) a coupled simulation has been presented where the discretization of the electromagnetic subsystem was based on an Eulerian formulation of the discrete system. This means that the Lagrangian mesh for the mechanical structure is moved over a *fixed* Eulerian mesh for the electromagnetic field. However, there are problems inherent to this approach since the character of the electromagnetic field equation in a certain point of the electromagnetic mesh changes from one instant to another when the structure moves over it: As long as it is not covered by the mechanical structure, the field equations are elliptic (instantaneous assumption of the equilibrium field) and they become parabolic (diffusion process) as soon as the point is covered by the sheet metal. This leads to a sudden change in the local discretizations since a contribution to the mass matrix arises as soon as a point is covered by the structure and it disappears when it is uncovered again (see Figure 4.14 above right). Methods that rely on this Euler-Lagrange approach are sometimes called fictitious boundary methods and are also applied to simulate liquid-structure interaction in computational fluid dynamics (e.g. Anca et al. (2006)). It has turned out that this change of the discretization in a certain point of the electromagnetic mesh causes oscillations in the time derivative of the vector potential and thus in the Lorentz force. If a good approximation to the forces is required an ALE-based method is more promising. Here, the position of the electromagnetic mesh is adapted to the current position of the structure so that the character of the electromagnetic field equations as well as the local discretizations never changes (see Figure 4.14 below right and left). In an ALE approach, the electromagnetic mesh is adapted to the moving structure so that the same elements are always covered by the moving mechanical structure. Consequently, the character of the discretization in a particular element does never change, which avoids jumps of the Lorentz force. The movement of the electromagnetic mesh is arbitrary in the sense that the position of the discretizing mesh is not determined by requirements of the electromagnetic field equations themselves, but by accompanying conditions. As mentioned above, one of these represents the matching of the mechanical and electromagnetic elements of the sheet metal according to its deformation. Ele-

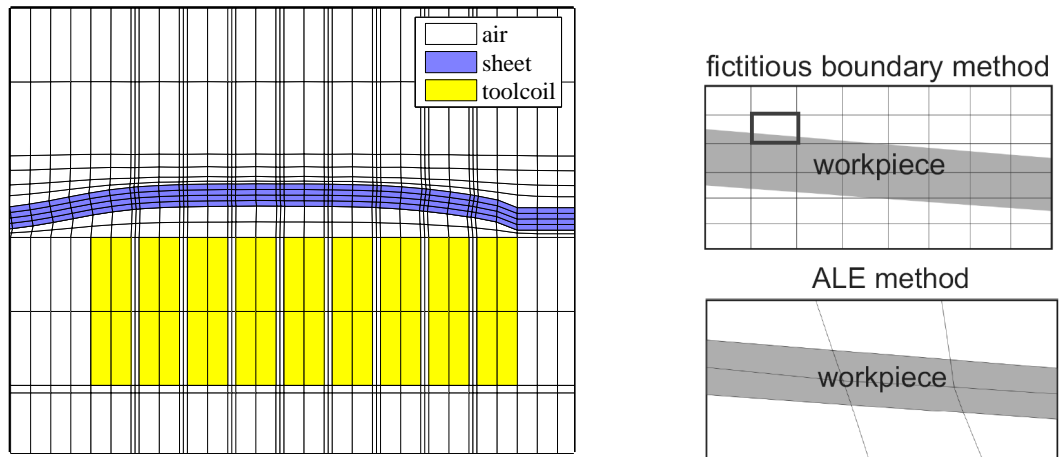


Figure 4.14: Illustration of the interaction between the mechanical and electromagnetic mesh. Left: 2D Modeling of an EMF process by means of the ALE algorithm. The electromagnetic and mechanical meshes of the sheet metal match. Right: Schematics of the fictitious boundary method (fixed Eulerian mesh) and the ALE method (matching meshes).

ments in the tool coil are fixed at their initial positions. To avoid mesh distortion or intersection induced by the deforming sheet metal the mesh in the surrounding air has to be adopted. This is based on a Lagrangian smoothing algorithm (Field, 1988).

In the above example of the ALE approach for 2D EMF modeling deformation and body force data is transferred from each element to each element. In this respect both discretizations can not be chosen independently. This situation can lead to unnecessary refinement for each subdomain depending on the necessary refinement of the other (see mesh in Figure 4.14 left). Since the extent of the problem in the case of 2D is relatively small in terms of computation time, this extra refinement can be accepted. Due to the problem size of 3D EMF simulations there is a strong motivation to refine both meshes independently. This requirement becomes even more fundamental if shell elements – commonly used in sheet forming simulations – are used for the mechanical mesh. Evidently, then the discretization in thickness direction of the mechanical mesh is fixed to one layer of elements. Here, an independent mesh refinement in thickness direction of the electromagnetic component of the sheet metal is mandatory. To resolve this issue in the electromagnetic part of the model, the deformation of the electromagnetic elements contained in the mechanical domain needs to be taken into account.

The approach to be presented here is based on the fact that at $t = 0$ the boundaries of the discretized electromagnetic and mechanical domain overlap. Later the sheet deforms and the vertex positions $\tilde{\mathbf{x}}$ of the electromagnetic mesh elements have to be adopted such that mesh domains are congruent again. To achieve this, similar to the 2D case, first the vertex positions of the electromagnetic elements of the sheet metal are moved according to the mechanical deformation and then the remaining vertex positions of the electromagnetic mesh are smoothed. In the 2D example (see Figure 4.14 left) the sheet element vertices of both, the mechanical and electromagnetic mesh match. In contrast, when using solid shell elements this is not the case.

A mapping of the mechanical deformation to those vertices of the electromagnetic mesh which are contained in the sheet metal is required. One proximate approach to achieve this is given by the simple shape function mapping of the actual nodal element positions $\mathbf{x}^e(t_n)$

$$\tilde{\mathbf{x}}_{\text{SM}}^i(t_n) = \mathbf{H}(\boldsymbol{\zeta}^i(\tilde{\mathbf{x}}_{\text{SM}}^i(t_n)))\mathbf{x}^e(t_n) \quad (4.3)$$

to the element vertex i contained in the sheet metal yielding its new position $\tilde{\mathbf{x}}_{\text{SM}}^i(t_n)$ at t_n . Here, $\tilde{\mathbf{x}}_{\text{SM}}(t_n)$ represents the positions of all element vertices of the electromagnetic mesh which are contained in the sheet, \mathbf{H} the shape function matrix evaluated at the local element coordinates $\boldsymbol{\zeta}^i$ which corresponds to $\tilde{\mathbf{x}}_{\text{SM}}^i(t_n)$.

Next, all variable positions of $\tilde{\mathbf{x}}$ are then adopted to $\tilde{\mathbf{x}}_{\text{SM}}$ via the aforementioned smoothing technique yielding the new mesh topology of the electromagnetic mesh at t_n . Figure 4.15 shows how the electromagnetic elements are moved according to the mechanically deformed mesh.

Next, the mapping of the electromagnetic loads is discussed. As shown in Section 4.8, for typical frequencies and sheet thicknesses, the Lorentz force distribution in sheet thickness direction can be highly non-linear and variable (see Figure 4.30). This motivates the separation of the algorithmic form (4.2) of the weak momentum balance (4.1)₁ into a component that is purely mechanical and a component resulting from the electromagnetic loads,

$$\mathbf{f}_{n+1,n} = \mathbf{f}_{n+1,n}^{\text{EM}}(\mathbf{x}_{n+1}, \mathbf{a}_{n+1}) + \mathbf{f}_{n+1,n}^{\text{Mech}}(\mathbf{x}_{n+1}) . \quad (4.4)$$

As indicated in Equation (4.4), $\mathbf{f}_{n+1,n}^{\text{EM}}$ is the part which is attributed to the Lorentz force coupling and receives particular attention, here. The structural force vector can be rewritten in terms of the usual assembly relation

$$\mathbf{f}_{n+1,n} = \sum_e \mathbf{I}_x^{eT} (\mathbf{f}_{n+1,n}^{e \text{ EM}}(\mathbf{x}_{n+1}^e, \mathbf{a}_{n+1}^e) + \mathbf{f}_{n+1,n}^{e \text{ Mech}}(\mathbf{x}_{n+1}^e)) . \quad (4.5)$$

Here, $\mathbf{f}_{n+1,n}^e$ represents the element contribution to the structural right hand side \mathbf{f}_n which is assembled with the help of the element connectivity matrix \mathbf{I}_x^e . In more detail the electromagnetic contribution $\mathbf{f}_{n+1,n}^{e \text{ EM}}$ is obtained via the usual integration over the element domain B_r^e

$$\mathbf{f}_{n+1,n}^{e \text{ EM}}(\mathbf{x}_{n+1}^e, \mathbf{a}_{n+1}^e) = - \int_{B_r^e} \mathbf{H}^T \det(\mathbf{F}^e(\mathbf{x}_{n+1}^e)) \boldsymbol{\ell}_{n+1}^e . \quad (4.6)$$

It is important to note that the integration of (4.6) needs to be accurate in the direction where $\boldsymbol{\ell}_{n+1}^e$ decays (see Figure 4.30 and 4.28). Equation (4.6) is integrated via Gaussian quadrature (Hughes, 1987). The accurate rendering of the non-linear decay is archived by choosing a high number of Gaussian points in the thickness direction of the element domain of the solid shell element. Both, mapping of the deformation and transfer of the body forces are illustrated in Figure 4.15.

The integration accuracy with which (4.6) is integrated is *one* condition to obtain an accurate representation of $\mathbf{f}_{n+1,n}^{e \text{ EM}}$. It should be notified that (4.6) leads to accurate results if not only the number of integration points is sufficiently high enough but also the values for $\boldsymbol{\ell}_{n+1}^e$ at the integration points are sufficiently accurate. For the edge based elements the magnetic flux density \mathbf{b} and current flux density \mathbf{j} are given at the barycenter of the element and so is $\boldsymbol{\ell}_{n+1}^e$.

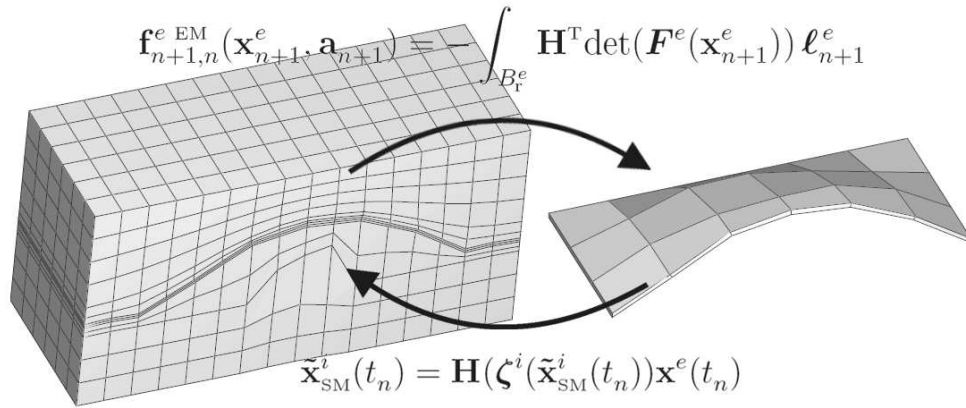


Figure 4.15: Illustration of data transfer in the context of the staggered solution algorithm at t_n . Body force data of the refined electromagnetic mesh is utilized to receive an accurate representation of the electromagnetic loading. The subsequent deformation of the sheet mapped to its electromagnetic counterpart and the element topology of the air is smoothed.

The barycenter closest to the global coordinates of a particular Gaussian point coordinate is used to evaluate ℓ_{n+1}^e in (4.6).

The method proposed above was tested by means of a single mechanical element. Here, the objective of the study at hand is to obtain an accurate representation of $\mathbf{f}_{n+1,n}^{e EM}$. To this end the influence of both, the accuracy of the integration of (4.6) and the one of ℓ_{n+1}^e at the integration points were investigated. Here, for any fixed number of integration points the amount of electromagnetic elements contained in the mechanical element was increased and the corresponding sum of the vertical electromagnetic element loads was examined. An eddy current and a magnetic field distribution was imposed. Both are acting in the plane of the sheet metal and are perpendicular to each other. As in the case of the fully coupled model, an exponential decay of both prevails. Decay constants were chosen closely resembling those computed below (see Figure 4.30). Magnetic flux and eddy current vectors are given at the barycenters of the electromagnetic elements. Exemplarily two mechanical elements containing two and eight electromagnetic elements with \mathbf{b} and \mathbf{j} at their barycenters are depicted in Figure 4.16.

The study of convergence depicted in Figure 4.17 demonstrates how the vertical loads converge with increasing number of electromagnetic elements and Gaussian points. Regardless of the number of Gaussian points, all curves start at the same value, which is sensible. If only one electromagnetic element is contained, the Lorentz force is assumed to be constant in the element and the nodal force result is independent of the accuracy of the integration. For the highest number of Gaussian points the nodal representation of the Lorentz force exhibits the best convergence. For lower numbers of Gaussian points the loads converge to values that are too small. A low number of Gaussian points implies that the bottom and top integration points are not located closely enough to the surface of the sheet, where body forces are maximal. This results in a pathological underestimation of the loads, which is also confirmed by an underestimation of the deformation of the sheet metal for the fully coupled simulation (see Figure 4.17).

Since the additional numerical effort to integrate (4.6) with 8 Gaussian points is relatively

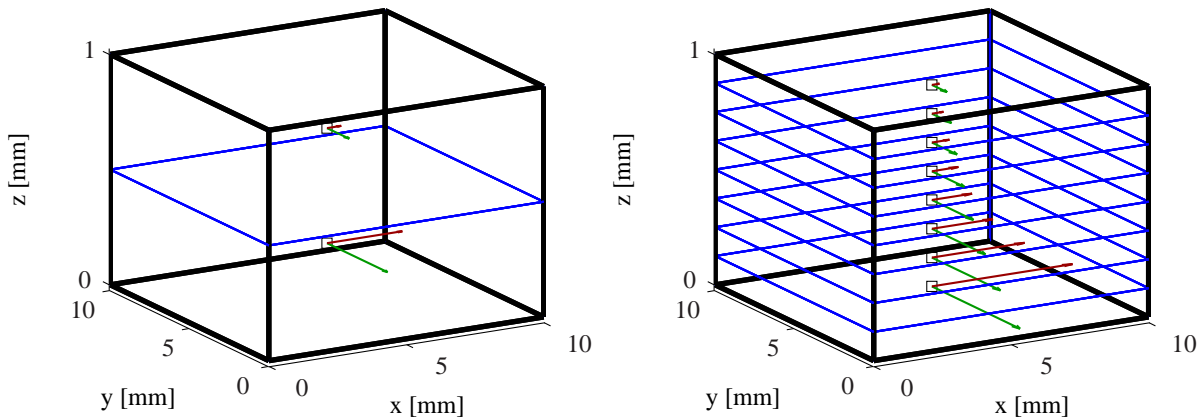


Figure 4.16: Two of seven electromagnetic discretizations to investigate the convergence of the electromagnetic loads with increasing refinement of the electromagnetic elements embedded in the mechanical one. Magnetic flux and eddy current vectors are given at the barycenters of the electromagnetic elements.

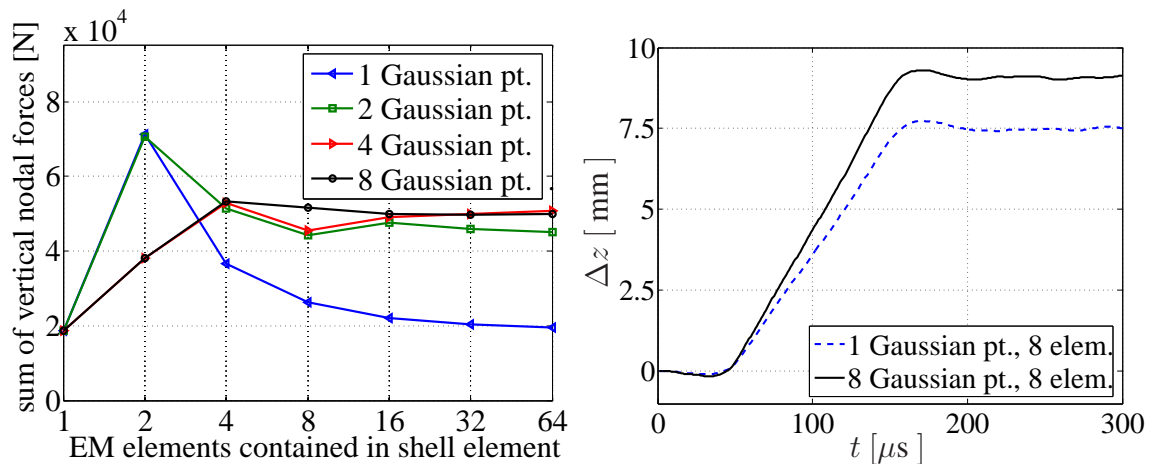


Figure 4.17: Study of accuracy of body force mapping algorithm. Left: Convergence of sum of vertical nodal forces resulting from electromagnetic body forces with increasing number of elements in sheet metal and Gaussian points. Right: Study of influence of Gaussian quadrature for a fully coupled simulation with respect to the vertical displacement at Point P2 (see Figure 4.19). The underestimation of electromagnetic loads for a small number of Gaussian points is confirmed.

small and a sound integration can be ensured, all subsequent calculations were computed in this manner. Secondly, it can be seen that good accuracy of the electromagnetic loads can be achieved by embedding at least 4 elements in the solid shell element.

4.5 Study of convergence of the mechanical model at fixed electromagnetic loads

To be able to determine the convergence behavior of the mechanical solution, the interaction between the mechanical and the electromagnetic model was suppressed. Even if one worked with an electromagnetic model, which remained unchanged in terms of its discretization, an

independent evaluation of the mechanical model would not be possible. If only the mechanical mesh was refined, the Lorentz force distribution would still be different due to the fact that the electromagnetic fields depend sensitively on the deformation of the sheet which in turn depends on its mechanical discretization. In this respect a separate comparability of the mechanical model discretization is only provided if the electromagnetic model is replaced by a body force distribution which is independent of the mechanical deformation. On the other hand however, the spatial body force distribution and its temporal progression should be chosen such that they are closely related to the fully coupled problem. Otherwise the conclusions drawn from the study of convergence might not apply in the context of the fully coupled problem. To find a suitable distribution the magnetic and eddy current field distributions of the finest mesh with $n_x = n_y = 24$ and full vertical discretization at $t = 8 \mu s$ serve as basis for the spatial component of the field. Regarding the temporal progression, the directions of \mathbf{b} and \mathbf{j} are independent of t . Only their magnitude is scaled with a time function which serves as a realistic temporal weighting. This function is obtained from coupled simulations and is depicted in Figure 4.18. As mentioned above the sheet metal is fully clamped at the edges parallel to the y -axis (see figures 4.18 and 4.20).

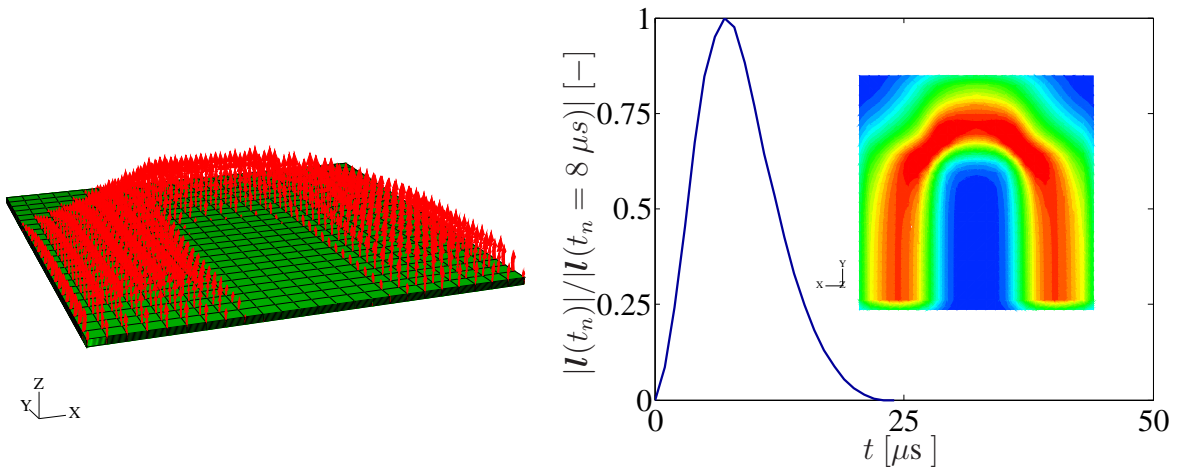


Figure 4.18: Illustration of fixed (*i.e.*, no interaction between mechanical and electromagnetic fields) Lorentz force distribution. Left: Direction Lorentz force field. Right: Temporal progression and vertical component at lower surface of plate.

Combinations of mesh refinement in x - and y -direction are investigated for the mechanical part of the model. Here, the number of elements in x -direction is denoted by n_{mx} and the number of elements in y -direction by n_{my} . Selected characteristic nodal values of the vertical deformation and the nodal projections of the equivalent plastic strain ϵ_p serve as indicators of convergence. As depicted in Figure 4.19 these are denoted by P1 and P2 and located above the winding of the tool coil and at the center of the plate .

While the evaluation at P1 and P2 serves as quantitative comparison of different discretizations, the figures 4.20 and 4.21 provide a qualitative impression of the progression of the inelastic and total deformation of the sheet metal. Here, Figure 4.20 shows deformation stages at the instances $t = 30 \mu s$, $t = 60 \mu s$, $t = 90 \mu s$ and $t = 120 \mu s$. At the beginning of the process the center of the plate remains at rest, whereas just above the tool coil the plate experiences

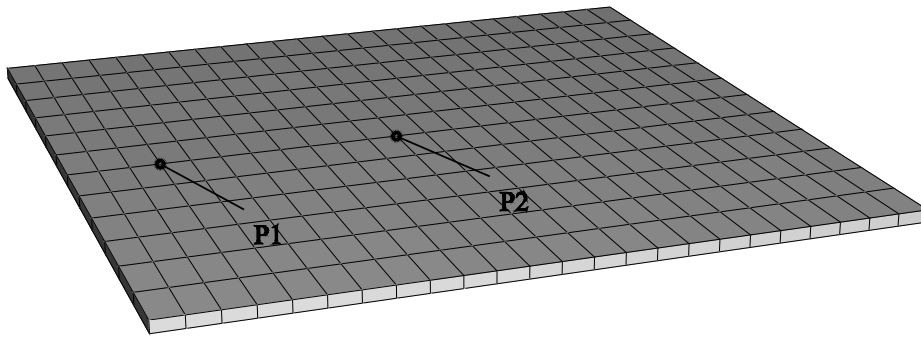


Figure 4.19: Illustration of points of evaluation for mechanical study of convergence. Here, P1 is located at the center of the left coil winding and P2 at the center of the sheet metal.

high Lorenz forces and begins to accelerate (see also Figure 4.18). In later stages the center of the plate is then pulled along by the rest of the plate and accelerated via predominantly inertial forces. The final shape representing a rooftop-shaped structure is depicted in Figure 4.21 along with top view contour plots of ϵ_p .

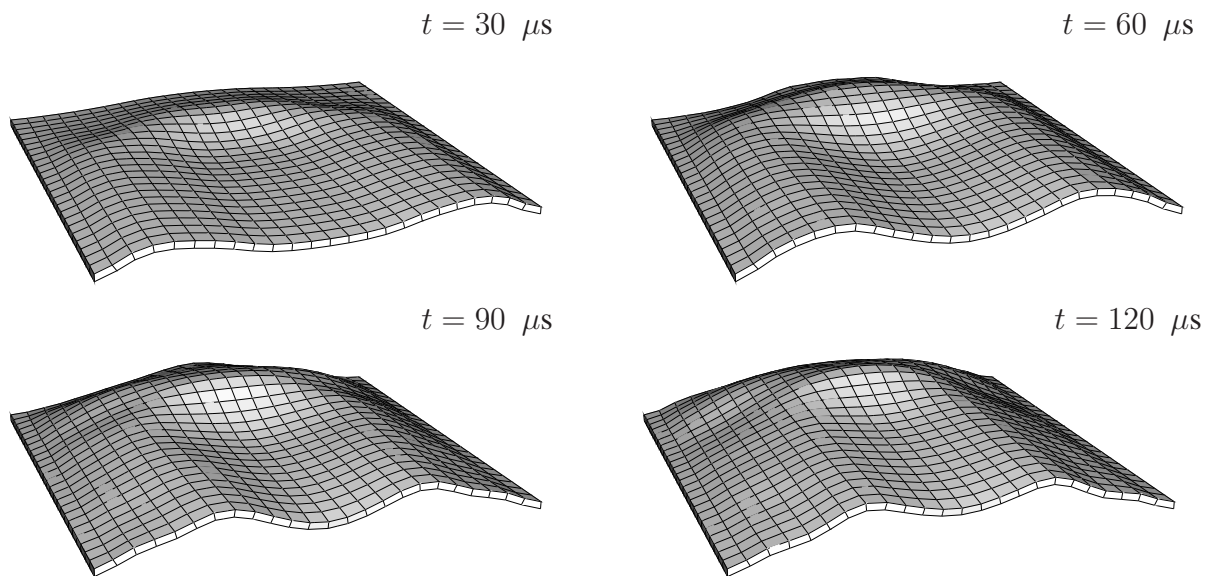


Figure 4.20: Deformation stages at various instances for the finest discretization (*i.e.* $n_{mx} = n_{my} = 24$) obtained by means of the body force distribution depicted in Figure 4.18.

Figure 4.21 also indicates the dependence of the deformation and ϵ_p on mesh refinement in a particular direction. Regarding the maximal deformation and maximal value of ϵ_p Figure 4.21 indicates that the sensitivity to mesh refinement in x -direction is much stronger than in y -direction. While the coarsest mesh refinement in y -direction with $n_{mx} = 4n_{my} = 24$ still yields a similar final shape and maximal value for ϵ_p as the finest discretization with $n_{mx} = n_{my} = 24$, a coarse discretization in x -direction results in a wrong prediction of the deformation and maximal value of ϵ_p . This can be explained by the electromagnetic loading in combination with the mechanical boundary conditions. Due to the geometry of the tool coil, the corresponding body force distribution and the lateral fixing the plate is bent predominantly about the y -axis.

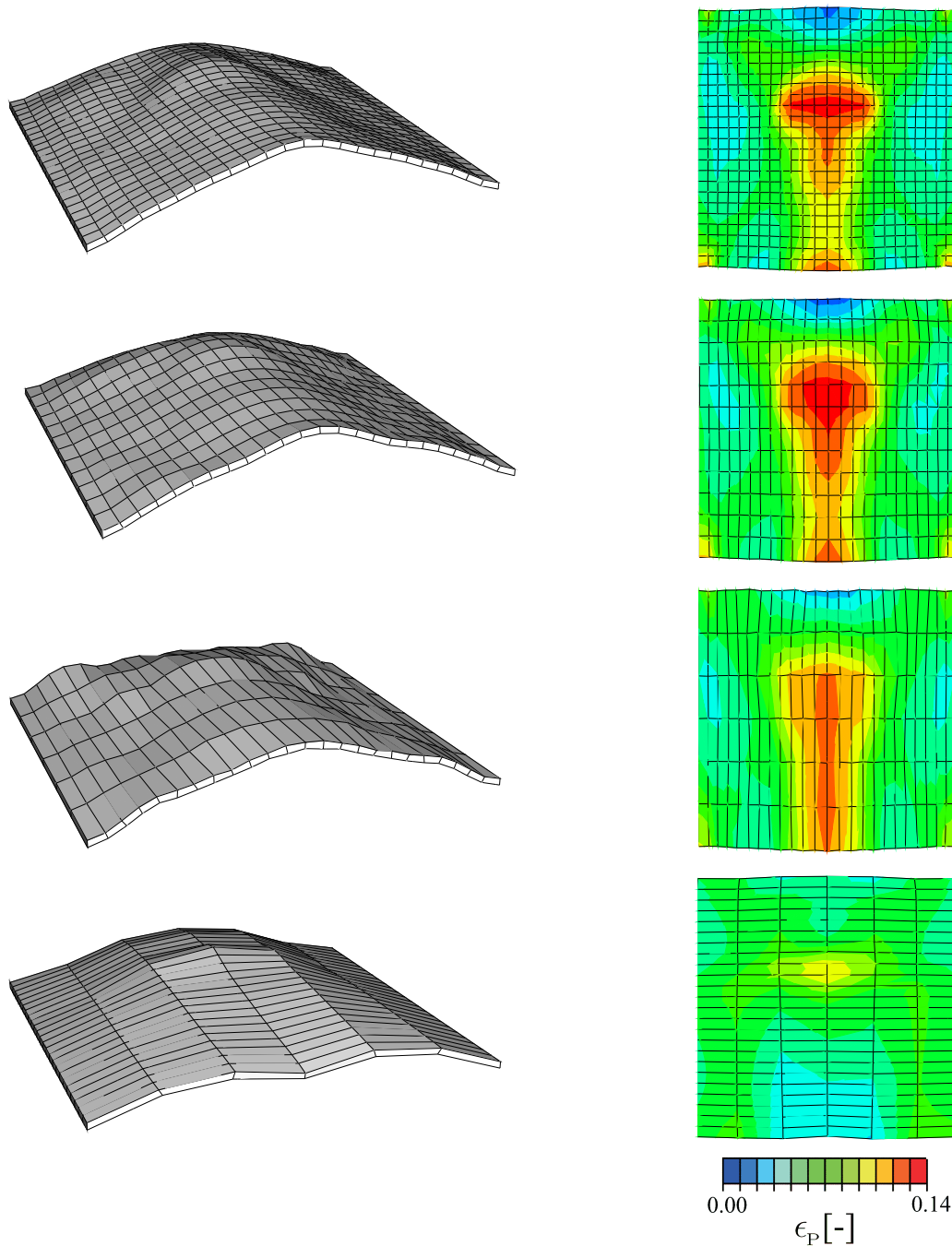


Figure 4.21: Final shape of sheet metal and corresponding top view contour plots of ϵ_p at $t = 300 \mu\text{s}$ for different mechanical discretizations ($n_{mx} = n_{my} = 24$, $n_{mx} = 2n_{my} = 24$, $n_{mx} = 4n_{my} = 24$ and $4n_{mx} = n_{my} = 24$). Deformed shapes and contour plots indicate a pronounced sensitivity with respect to the discretization in x -direction (see in particular last discretization with $4n_{mx} = n_{my} = 24$) while the y -direction is less sensitive to mesh refinement (see first three discretizations).

Only at the rear part of the coil the electromagnetic loads are such that bending about the x -axis occurs. However, since there is no mechanical fixing at these locations it turns out to be less pronounced.

A quantitative evaluation at P1 and P2 confirms the above findings. Here, Figure 4.22 demon-

strates the sensitivity to mesh refinement with respect to vertical deformation Δz . While a coarse mesh in y -direction yields a reduction of about 2.5 % of the final shape of the sheet metal, coarsening in x -direction results in an underestimation of the deformation by about 25 %. For the accumulated equivalent inelastic strain the deviations are even more severe (see Figure 4.23). Here, for $n_{mx} = 6$ at P1 the inelastic deformation is overestimated by 35 % and underestimated by 43 % at P2. As can be seen in figures 4.21, 4.22 and 4.23, a very good agreement can be found between $n_{mx} = n_{my} = 24$ and $n_{mx} = 2n_{my} = 24$. By choosing $n_{mx} = 2n_{my} = 24$ for subsequent coupled simulations the computation time can be reduced significantly while conserving solution accuracy.

Regarding computation time, the electromagnetic part of the coupled system represents the most extensive part of the model. In this respect the reduction of computational cost due to mesh coarsening of the mechanical component of the model is relatively small. However one should note that an interrelation between the electromagnetic and the mechanical mesh exists. For a particular electromagnetic discretization it is possible to choose a mechanical discretization which is coarser than the electromagnetic one. Vice versa it is not possible to choose a mechanical mesh which is more refined than the electromagnetic one. In this respect the above discussed mesh coarsening (*i.e.*, $n_{mx} = 2n_{my} = 24$) allows for a mesh coarsening of the electromagnetic mesh. This is the reason for the significant reduction of computational cost.

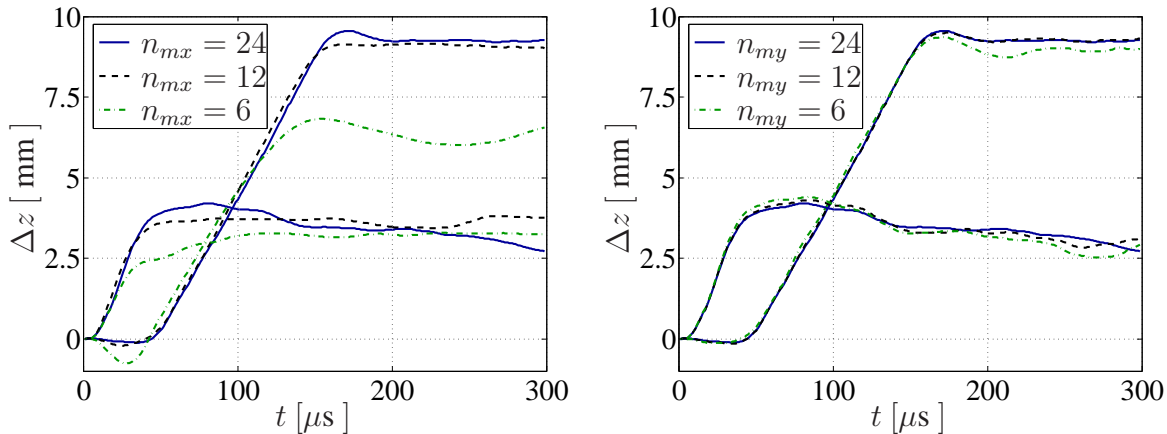


Figure 4.22: Study of convergence of mechanical mesh with respect to different directions of refinement for vertical deformation at P1 and P2. Left: Study of convergence for x -direction. Right: Study of convergence for y -direction.

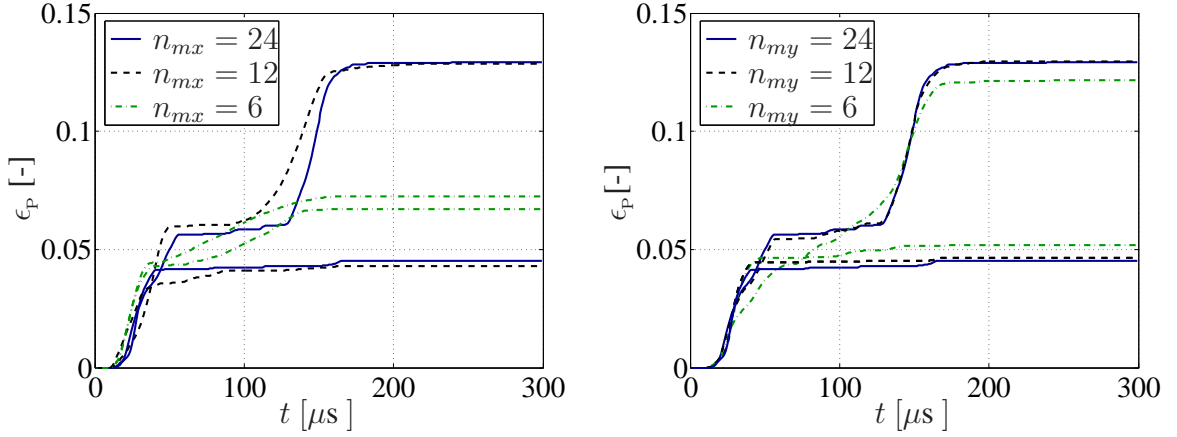


Figure 4.23: Study of convergence of mechanical mesh with respect to different directions of refinement for ϵ_p at P1 and P2. Left: Study of convergence for x -direction. Right: Study of convergence for y -direction.

4.6 Termination criterion for the computation of the electromagnetic part

As mentioned above, the largest computational effort is to be attributed to the solving of the electromagnetic part of the model. Since the forming operation is the focus of the current study, it is important to note that external loading due to Lorentz forces typically takes place in the beginning of the process, during the first alternation of the tool coil current. Later, the amount of energy transferred to the sheet metal via electromagnetic loads is relatively small. At this time the actual forming takes place predominantly due to inertial forces. This offers potential to save further computational cost. If it is possible to find a meaningful criterion to judge whether the electromagnetic loads are still significant for the forming operation or whether they can be neglected, the total computation time could be reduced enormously. If such a termination criterion indicates the insignificance of the electromagnetic loads, the electromagnetic part of the model can be turned off and only the fast mechanical part of the model remains. In the field of non-linear finite element modeling convergence criteria commonly applied for the termination of global Newton Raphson schemes are usually based on the change of the energy of the corresponding Newton step in relation to the energy change of the first iteration

$$\Delta \mathbf{x}_{n+1,n}^i \cdot \mathbf{f}_{n+1,n}^i \leq \epsilon_c \Delta \mathbf{x}_{n+1,n}^1 \cdot \mathbf{f}_{n+1,n}^1 \quad (4.7)$$

Here, $\Delta \mathbf{x}_{n+1,n}^i \cdot \mathbf{f}_{n+1,n}^i$ represents the energy change in terms of the deviation $\Delta \mathbf{x}_{n+1,n}^i$ of the nodal positions and the residual force vector $\mathbf{f}_{n+1,n}^i$ corresponding to the Newton step i . ϵ_c represents the tolerance for which (4.7) is fulfilled. Accordingly a termination criterion for the electromagnetic model is based on the energy transferred from the electromagnetic system to the mechanical one. If the amount of energy transferred after some time $t \geq t_{\text{ter}}$ is significantly smaller than the amount of energy that has been transferred up to this instance, it can be expected that an accurate representation of the mechanical deformation can be obtained without further consideration of the electromagnetic system. Therefore, with some tolerance ϵ_{EM} the electromagnetic simulation is stopped at termination time t_{ter} if

$$E_{\text{EM}}(\infty) - E_{\text{EM}}(t_{\text{ter}}) = \int_{t_{\text{ter}}}^{\infty} P_{\text{EM}} dt \leq \epsilon_{\text{EM}} \int_0^{t_{\text{ter}}} P_{\text{EM}} dt \quad (4.8)$$

is fulfilled. Here, $P_{EM}(t)$ represents the rate of energy transferred at instance t and $E_{EM}(t)$ the energy transferred from the electromagnetic system until instance t . Since the quantity $E_{EM}(\infty) - E_{EM}(t_{ter})$ is unknown, an alternative criterion based on the comparison of $P_{EM}(t)$ is employed. Here, the rate of energy at $t_{n+1,n}$ is estimated on the basis of the nodal velocities at t_{n+1} and the nodal representations of the electromagnetic loads given in (4.4)

$$P_{EM}(t_{n+1}) \approx \frac{(\mathbf{x}_{n+1} - \mathbf{x}_n) \cdot \mathbf{f}_{n+1}^{EM}}{t_{n+1,n}}. \quad (4.9)$$

In the particular case of EMF the rate of energy transferred to the mechanical part oscillates with decreasing amplitude as can be seen in Figure 4.24. This results from the oscillation of the input current. In particular during the first alternation, the largest amount of energy is transferred to the mechanical part. At later instances the intensity of the magnetic field is reduced due to the imposed input current and the expanded air gap between the sheet and the tool coil. Correspondingly, the peak values $P_{EM}(t_{Pi})$ of $P_{EM}(t)$ decay. In this case, relating the first peak value $P_{EM}(t_{P1})$ to the current peak value $P_{EM}(t_{Pi})$ represents a close match for the termination criterion given in (4.8) and represents a meaningful termination criterion. If the energy contribution for $t \geq t_{Pi}$ is sufficiently small, the computation of the electromagnetic system can be terminated. In this respect the new termination criterion is denoted by

$$t_{ter} = t_{Pi} \text{ if } P_{EM}(t_{Pi}) \leq \epsilon_{EM} P_{EM}(t_{P1}). \quad (4.10)$$

It is important to note that the value for ϵ_c in (4.7) can precisely be determined on the basis of the best possible numerical accuracy (usually $\epsilon_c = 1 \times 10^{-16}$). For ϵ_{EM} this is not the case. There is some degree of freedom given to the modeler to choose some value for ϵ_{EM} for which accurate results can be expected at reasonable modeling effort for a particular class of EMF processes. To show and quantify the effect of the termination of the electromagnetic simulation with respect to the forming result, different values for ϵ_{EM} were chosen and the corresponding results were compared. Since the principal findings regarding the energy conversion are similar for coarse and fine meshes (see Section 4.8 Figure 4.31), a coarse mesh for the study of the termination criterion was chosen to save computation time.

Figure 4.24 shows the progression of P_{EM} . Each marker indicates the termination of the electromagnetic system corresponding to three different values for ϵ_{EM} attributed to 1.5 %, 3 % and 6 % of the first peak value $P_{EM}(t_{P1})$. After terminating the electromagnetic simulation the total amount of energy $E_{EM}(t)$ transferred to the mechanical system remains constant which can be confirmed by the straight lines. The dotted red curve shows a simulation without termination of the electromagnetic system and serves as reference solution. Further, the graphs for the total amount of energy transferred $E_{EM}(t)$ indicate how criteria (4.8) and (4.10) are related to each other. As depicted in figures 4.24 and 4.25 the difference between the reference solution and the terminated one becomes smaller with decreasing ϵ_{EM} .

Also interesting from the point of view of the technological process simulation is certainly the degree of deviation in terms of the deformation. To this end, the vertical displacement at evaluation Point P2 was examined for the three values for ϵ_{EM} . As can be seen in the left part of Figure 4.25 only for $\epsilon_{EM} = 0.06$ the deformation exhibits a significant underestimation (solid curve). For all other termination criteria the deformation is very close to the reference solution

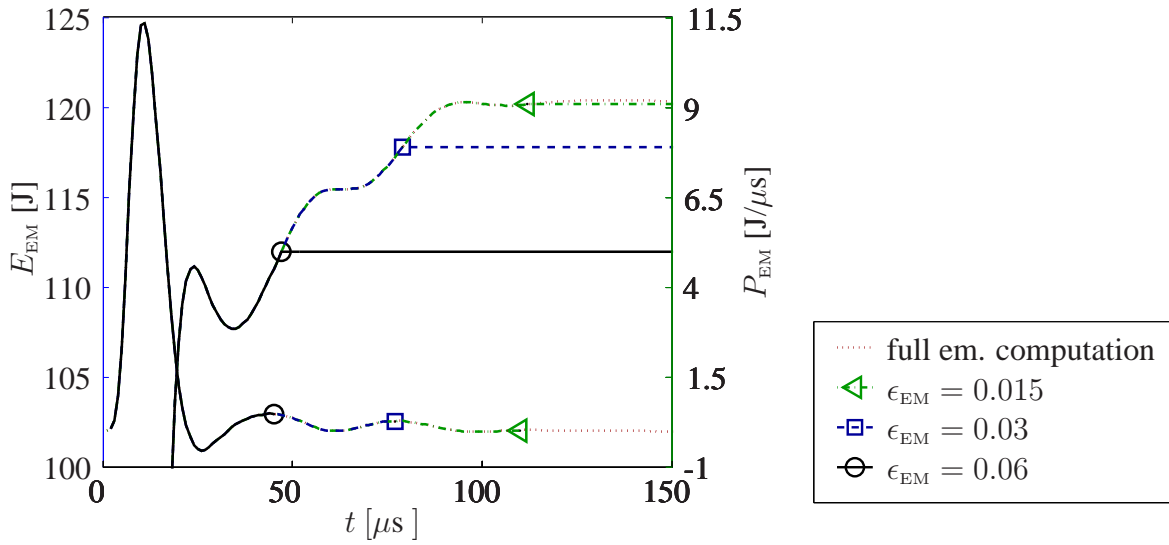


Figure 4.24: Illustration of termination criterion for different termination tolerances ϵ_{EM} corresponding to 1.5 %, 3 % and 6 % of the first peak value $P_{EM}(t_{P1})$. The plot for P_{EM} shows how most of the energy is transferred to the mechanical system during the first alternation. To resolve the increase of E_{EM} due to subsequent alternations the left ordinate starts at 100 J. After termination of the electromagnetic part of the model $P_{EM} = 0$ and $E_{EM} = \text{const.}$.

(dotted curve). To quantify this the displacement Δz and transferred energy E_{EM} at $t = 300 \mu s$ were compared for the different termination criteria (see right part of Figure 4.25). Similar as in previous cases the relative deviation is highlighted by normalization with the reference solution yielding the normalized values $\Delta \bar{z}$ and \bar{E}_{EM} . Due to the nature of the termination criterion $\bar{E}_{EM} < 1$. As a result of small elastic oscillations $\Delta \bar{z} > 1$ is possible for the comparison of the deformation. In view of subsequent simulations, $\epsilon_{EM} = 0.03$ seems to represent a reasonable choice.

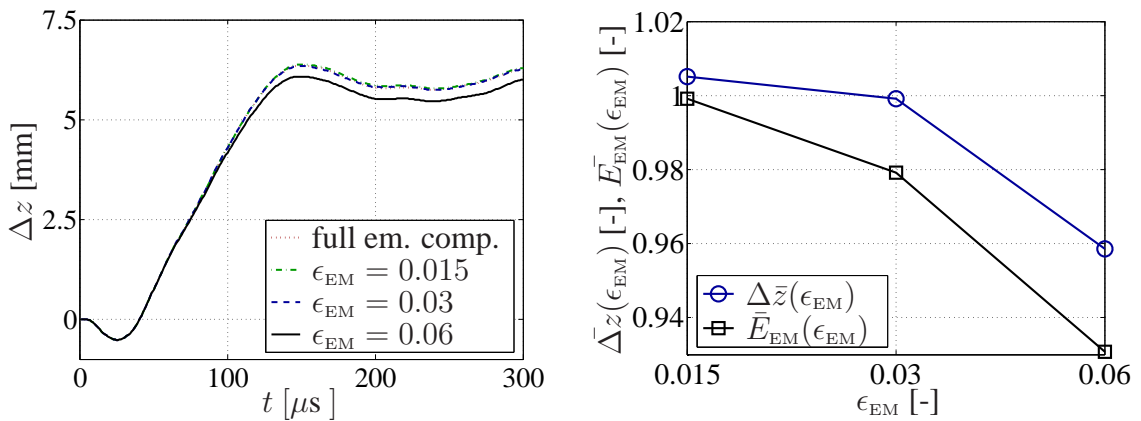


Figure 4.25: Influence of ϵ_{EM} on the vertical deformation at P2 and E_{EM} . Left: Vertical deformation with evolving time. Right: Normalized vertical deformation at $t = 300 \mu s$ and E_{EM} depending on different values for ϵ_{EM} .

4.7 Discussion of all model simplifications

Two objectives drive the above considerations regarding means to evaluate the size of the bounding box, spatial finite element discretization and termination criterion. On the one hand these studies allow for an estimation of the degree of convergence of the solution and provide insight with respect to the expected error due to the chosen discretization. On the other hand the findings allow for the exploitation of potential for reduction of the computation time by selectively choosing a coarse discretization at locations where this is admissible according to the study of convergence within the scope of the desired accuracy. A good example of this reasoning is the evaluation of the vertical mesh parameters for the tool coil, air gap and upper air. The studies of convergence for these parameters indicate that an accurate solution is already obtained for a very coarse mesh (see Figure 4.10). This could be explained by physical phenomena in the particular element layer (tool coil layer, air gap layer or upper air layer). Crucial to the modeling accuracy and model simplification however was the *quantification* of the deviation by means of the study of convergence. Here, it is important to note that the choice of field variables subject to the study of convergence has to be made with respect to the simulation objective. In the case of EMF the objective is to obtain an accurate prediction of the deformation and inelastic internal variables. In Table 4.1 all taken measures to obtain a simplified model are summarized. This includes information regarding the model reduction in terms of the number of degrees of freedom of the electromagnetic system and the computation time for a coupled simulation ending at $t = 300 \mu\text{s}$ with a time step $t_{n+1,n} = 1 \mu\text{s}$ (see *e.g.* (Schinnerl et al., 2002)). Further, on the basis of the study of convergence the deviation of the deformation due to the particular measure was estimated. In general the reduction of the size of the bounding box, mesh coarsening or termination of the electromagnetic simulation leads to an underestimation of the magnitude of \mathbf{b} and \mathbf{j} and thus of the deformation. To roughly quantify the reduction of deformation for the mechanical simulation the magnitude of \mathbf{b} and \mathbf{j} was reduced by 1 % for the fixed field distribution shown in Figure 4.18. As a result the deformation at P2 was reduced by about 0.8 % serving as a basis for the quantification of the error of the model simplifications listed in Table 4.1. For the subsequent fully coupled simulation all mesh parameters are summarized in Table 4.2.

For many mesh parameters the results of the studies of convergence can be transferred to other typical forming setups. In general, the results for discretization parameters like the number of elements in the air gap n_{ag} , tool coil n_{tc} , sheet metal n_{sm} , air above and below the setup $n_{aa,ab}$ can at least qualitatively be transferred to any other setup, regardless of the particular tool coil design (circular, elliptical, rectangular, etc.) and forming setup, since all of these setups exhibit equivalent features that can be discretized with the arguments discussed above. The same applies to the evaluation of the size of the bounding box d and the termination criterion. For the discretization parameters in the plane of the sheet metal (n_x and n_y) some degree of transferability is given for elliptical or circular tool coil forming setups. For such a setup, n_x can be attributed to the radial direction and n_y to the circumferential one. It is expected that the sensitivity of the results is less pronounced in circumferential direction, where the coil windings proceed.

Modeling of EMF is an evolving field and the above discussed measures represent only a

selection of means to save computational cost. However these are general since they refer to physical features of the forming operation and are valid regardless of the numerical methods that are utilized. Further development of algorithmic strategies also offer potential in this regard and represent work in progress.

	reduction of size of bounding box	mesh coarsening in xy -plane	mesh coarsening in vertical dir.	termination criterion
No. dof before	6.5×10^5	1.4×10^5	6.9×10^4	3.2×10^4
No. dof after	1.4×10^5	6.9×10^4	3.2×10^4	3.2×10^4
T_{sim} [d] before	too large	3.7×10^1	1.7×10^1	6.5×10^0
T_{sim} [d] after	3.7×10^1	1.7×10^1	6.5×10^0	2.4×10^0
approx. reduction of deformation	< 1.5 %	< 0.2 %	< 2 %	< 0.1 %
reference to figures	4.3,4.4	4.7	4.12,4.10	4.24,4.25

Table 4.1: Summary of the evaluation of the potential to reduce the computational effort. in terms of the number of degrees of freedom and computation time at simultaneous evaluation of the associated error of the modeling result.

mesh parameter	initial	after study
d	60 mm	15 mm
n_x	24	24
n_y	24	12
n_{mx}	24	24
n_{my}	24	12
n_{aa}	8	2
n_{ab}	8	4
n_{ag}	8	2
n_{tc}	8	2
n_{sm}	8	8

Table 4.2: Summary of the evaluation of mesh parameters.

4.8 Discussion of results for a fully coupled simulation

With the above simplifications at hand we now turn to the fully coupled simulation of the EMF process. As discussed above the energy driving the forming operation is characterized by the discharging current depicted in Figure 4.1 which was implemented as a Neumann boundary condition for χ . For the instance $t = 8 \mu\text{s}$ where I is maximal χ is depicted in the upper part of Figure 4.26. Starting from the right connection surface where $\chi = 0$ is prescribed, the potential increases to a maximum value of $\chi = 4.1 \text{ kV}$ to satisfy (4.1)₃ and the remaining Neumann boundary conditions. As could be expected, the *magnitude* of $\mathbf{j} = -\sigma_{\text{EM}} \nabla_{\text{s}} \chi$ inside the tool coil at $t = 8 \mu\text{s}$ remains relatively unchanged, only \mathbf{j} changes its direction following the centerline of the coil winding as can be seen in the center part of Figure 4.26. If eddy currents had been considered some non-uniform distribution of \mathbf{j} in the tool coil cross section could have been expected. In the lower part of Figure 4.26, \mathbf{j} is depicted for $t = 40 \mu\text{s}$. At this instance the input current has reached its second extreme value (see Figure 4.1) and flows in opposite direction. Accordingly the direction of \mathbf{j} is flipped and has a reduced magnitude.

Next we turn to the development of the magnetic flux density \mathbf{b} at the instances $t = 4 \mu\text{s}$, $t = 12 \mu\text{s}$ and $t = 28 \mu\text{s}$. Up to $t = 28 \mu\text{s}$ the largest portion of E_{EM} is transferred to the mechanical part of the model (see figures 4.24 and 4.31). In this respect this period of time is significant for the forming operation. Due to the correlation of the tool coil current with the input current, also \mathbf{b} is correlated to the input current via Ampere's law. As can be seen by comparison of Figure 4.27 (above) and Figure 4.27 (center) the increased input current at $t = 12 \mu\text{s}$ results in an increase of \mathbf{b} . At $t = 28 \mu\text{s}$ where I just flipped (see Figure 4.27 (below)) the current in the tool coil and so \mathbf{b} are small. At all instances \mathbf{b} is insignificant above the sheet metal. This can be attributed to the eddy currents induced in the sheet metal (see Figure 4.28). Here, the temporal evolution of the magnetic field becomes important. The increase of I until $t = 8 \mu\text{s}$ leads to an increase of \mathbf{b} in the air in the center of the tool coil winding. The magnetic field and its increase $\partial\mathbf{b}$ are oriented in z -direction here. According to Faraday's law of induction, $\partial\mathbf{b}$ induces an electric field which drives eddy currents which proceed along the tool coil winding and are oriented in opposition to the current in the winding (compare figures 4.26 and 4.28). Due to their orientation, these eddy currents neutralize the magnetic field above and inside the sheet metal and lead to the shielding effect. Furthermore at $t = 12 \mu\text{s}$ in contrast to $t = 4 \mu\text{s}$, \mathbf{b} begins to penetrate the sheet metal which can be seen by the vectors of \mathbf{b} at the upper surface of the sheet metal. This is discussed below together with the development of the eddy currents in the sheet metal.

In Figure 4.28 the eddy current distributions for the aforementioned instances are shown. In more detail this is depicted in Figure 4.30 where the significant components j_y of \mathbf{j} and b_x of \mathbf{b} are depicted along PZ with increasing time. Since the sheet metal deforms under the influence of the Lorentz force the current flux distributions move in vertical direction with increasing time. At the beginning of the process, where the input current exhibits a significant increase, the magnetic field increases in particular close to the lower surface of the sheet metal while an increase inside the sheet metal is relatively small. Accordingly eddy currents occur close to the lower surface as well (see instance $t = 4 \mu\text{s}$ Figure 4.30) to counter the local penetration of \mathbf{b} . Later, when the first alternation reached its peak at $t = 8 \mu\text{s}$ as discussed above, \mathbf{b} becomes

maximal and remains constant outside the sheet metal and the increase close to the surface of the sheet metal is reduced. Accordingly the eddy currents induced here are reduced in comparison to $t = 4 \mu\text{s}$. Inside the sheet metal, however, $\partial\mathbf{b}$ might be larger than at previous instances due to the fact that further penetration of \mathbf{b} in the sheet metal is facilitated. This in turn leads to an induction of eddy currents into regions which are more distant from the lower surface. As can be seen in Figure 4.30 at $t = 4 \mu\text{s}$ the eddy currents close to the upper surface are insignificant and so is the magnetic flux density. While proceeding further to $t = 8 \mu\text{s}$ inside the sheet metal, b_x has risen, consequently even close to the upper surface j_y has become significant while close to the lower surface j_y is reduced. With increasing time (see, e.g., $t = 12 \mu\text{s}$) the magnetic field in the air gap decreases, then the eddy currents close to the surface become smaller than inside the sheet metal where the penetration of the magnetic field still leads to an increase of b_x . Close to the lower surface now the effect of self induction of the sheet leads to a retention of the eddy currents although \mathbf{b} decreases in the air gap. At $t = 20 \mu\text{s}$ and later instances, the eddy current direction is even reversed close to the lower surface of the sheet metal. The flipped eddy currents at the surface of the sheet superimpose a magnetic field to that of the tool coil which leads to a further reduction of the magnetic flux density at the surface of the sheet. The maximal value for b_x is now inside the sheet (see Figure 4.30 instances $t = 20 \mu\text{s}$, $t = 24 \mu\text{s}$ and $t = 28 \mu\text{s}$) and the maximal value for j_y at its upper surface.

Referring to the Lorentz force $\mathbf{l}_r = \det(\mathbf{F}) \mathbf{j} \times \mathbf{b}$ as a coupling term to the mechanical component the above discussion underlines the fact that special care has to be taken to account for the strong variations of \mathbf{b} and \mathbf{j} in the sheet metal (see Section 4.4). Further it could be seen that \mathbf{b} and \mathbf{j} penetrate the sheet metal at instances where they are still significant in terms of their magnitude (see e.g., $t = 8 \mu\text{s}$ in Figure 4.30), in this respect the notion of a magnetic pressure (Mamalis et al., 2004) in the context of EMF is not accurate since \mathbf{b} and \mathbf{j} and so the Lorentz force act inside the sheet metal. Regarding the development of \mathbf{b} and \mathbf{j} with respect to the progression of the forming operation from figures 4.27 and 4.28 it can be seen that \mathbf{l}_r predominantly acts in positive vertical direction and evolves below the tool coil winding (see also Figure 4.18). This applies to all alternations regardless of the direction of the input current, \mathbf{b} and \mathbf{j} basically flip simultaneously. Only at some time shortly before zero-crossing of the input current \mathbf{b} and \mathbf{j} are oriented such that \mathbf{l}_r points downwards (see Figure 4.30, instances $t = 20 \mu\text{s}$ and $t = 24 \mu\text{s}$).

The temporal development of \mathbf{l}_r can be deduced from Figure 4.30. While at the very beginning of the process the largest eddy currents are induced, the magnetic flux density is still relatively small since the tool coil current is relatively small as well; moreover the sheet metal is basically at rest meaning that very little energy is transferred to the mechanical system. At some time between $t = 4 \mu\text{s}$ and $t = 20 \mu\text{s}$ where both, the velocity of the sheet metal and $\mathbf{l}_r = \det(\mathbf{F}) \mathbf{j} \times \mathbf{b}$ are relatively large, the forming operation is most effective. In fact this motivates the redesign of the electric circuit attached to the forming setup – presently basically consisting of a switch and a capacitor – such that the efficiency of the process can be increased.

The aforementioned Lorentz force distribution is also reflected by the stages of deformation depicted in Figure 4.29. At the beginning of the process, the center of the plate remains at rest, whereas just above the tool coil winding, the plate experiences high Lorenz forces and begins to accelerate (see Figure 4.29, instance $t = 30 \mu\text{s}$). The contour plots represent the development

of the accumulated inelastic deformation for this stage of deformation as a top view of the sheet metal. Due to the boundary conditions of the sheet metal for $t = 30 \mu\text{s}$ the lateral regions exhibit an increase of ϵ_p , the rear part of the structure exhibits no inelastic deformation due to the fact that the sheet metal can move freely and \mathbf{l}_r is less pronounced here (see also Figure 4.18). The lateral fixing leads to a combined bending and stretching of the sheet caused by the body force distribution nearby. In particular at the front corners of the sheet the inelastic deformation exhibits its maximal value of $\epsilon_p \approx 0.8$. The loading of the plate leads to a lateral contraction of the plate which becomes zero at the fixed edge of the plate. The strains resulting from this lateral deformation, however, are maximal here and contribute to the increase of ϵ_p . With increasing time (see Figure 4.29, $t = 60 \mu\text{s}$) the accelerated parts of the structure continue to deform and the center of the plate – initially at rest – begins to move. In addition to the front corners of the sheet metal now the rear corners exhibit an increased inelastic deformation as well and bands of increased inelastic deformation propagate from the front corners to the center of the sheet. At $t = 90 \mu\text{s}$ and $t = 120 \mu\text{s}$ the center of the plate is accelerated further, the bands of deformation evolve and close to the center of the plate a maximum for ϵ_p starts to develop. The final shape of the structure for $t = 300 \mu\text{s}$ is shown at the bottom part of Figure 4.29. During the last forming stages the initially downwards bent center of the structure is now pulled along with the lateral regions of the plate and bent upwards resulting in a roof-top shaped structure. The strong inelastic bending results in an additional increase of ϵ_p at the center of the plate. In Figure 4.31 the vertical deformation at P1 and P2 and the energy $E_{EM}(t)$ is depicted. In comparison to Figure 4.25, where a comparatively coarse mesh was utilized, the deformation is much larger. This is in accordance with the mechanical convergence study. In conclusion it is not surprising that the increased resilience of the refined mesh also leads to a higher value for E_{EM} (see Figure 4.24 right). The structure starts to deform earlier and more energy is transferred.

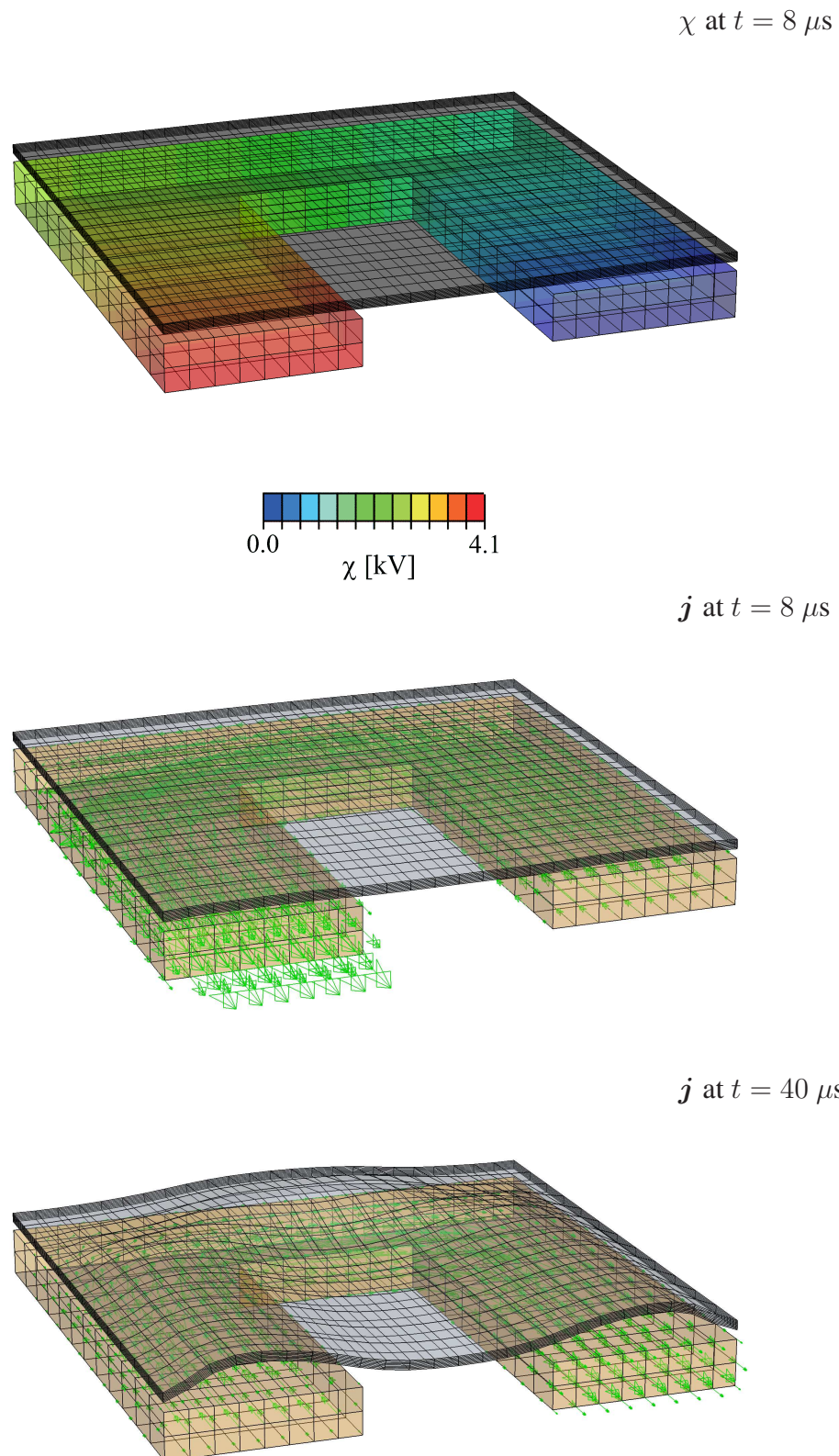


Figure 4.26: Electric potential and current distribution in tool coil. Above: scalar potential χ at maximal input current. Center: current density distribution in the tool coil at maximal input current. Below: current density distribution in the tool coil at second extreme value of I and flipped direction (see Figure 4.1).

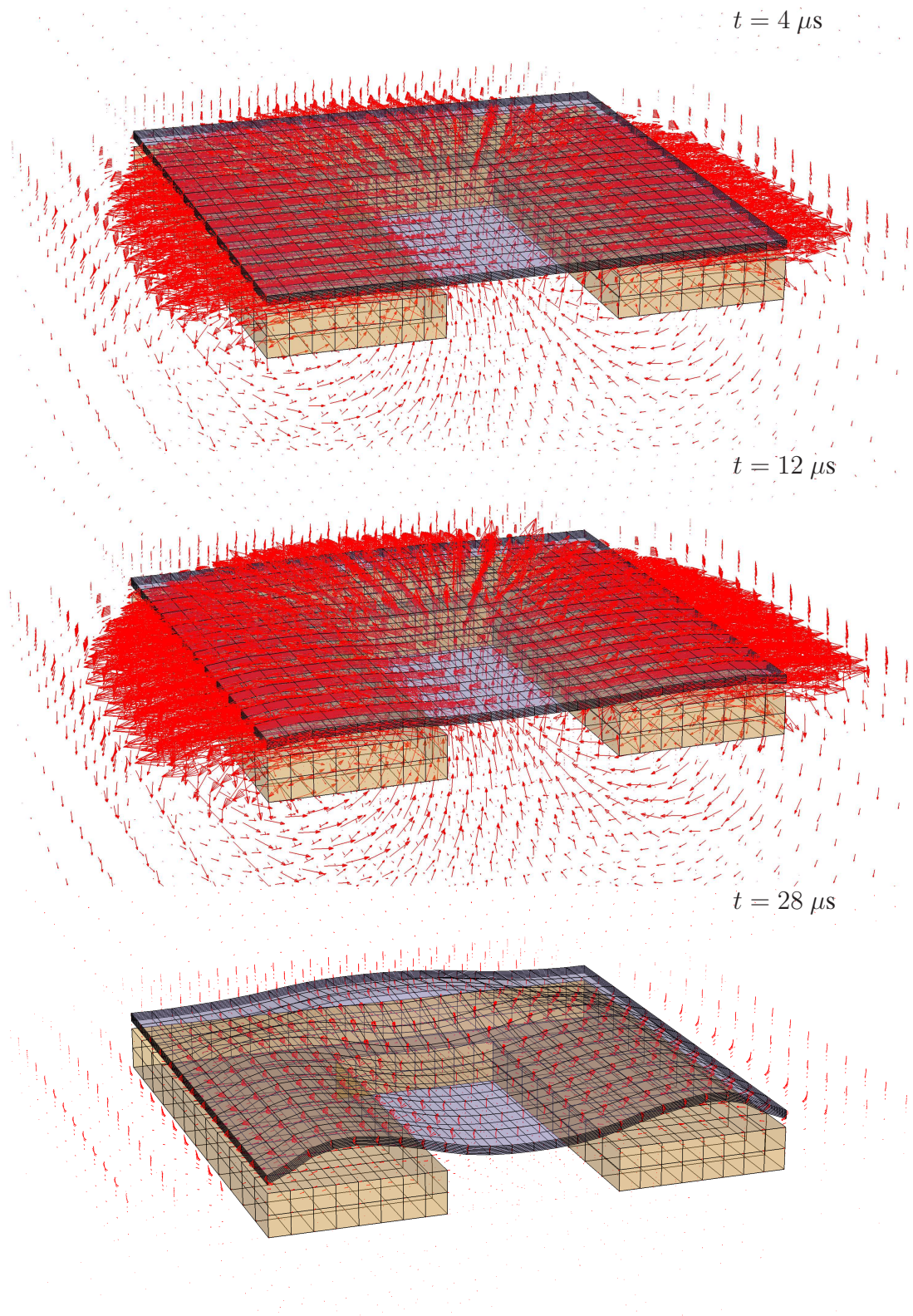


Figure 4.27: Magnetic flux density distribution for the instances $t = 4 \mu s$, $t = 12 \mu s$ and $t = 28 \mu s$. With increasing input current I the magnetic flux density b increases as well. The shielding effect of the sheet metal becomes evident.

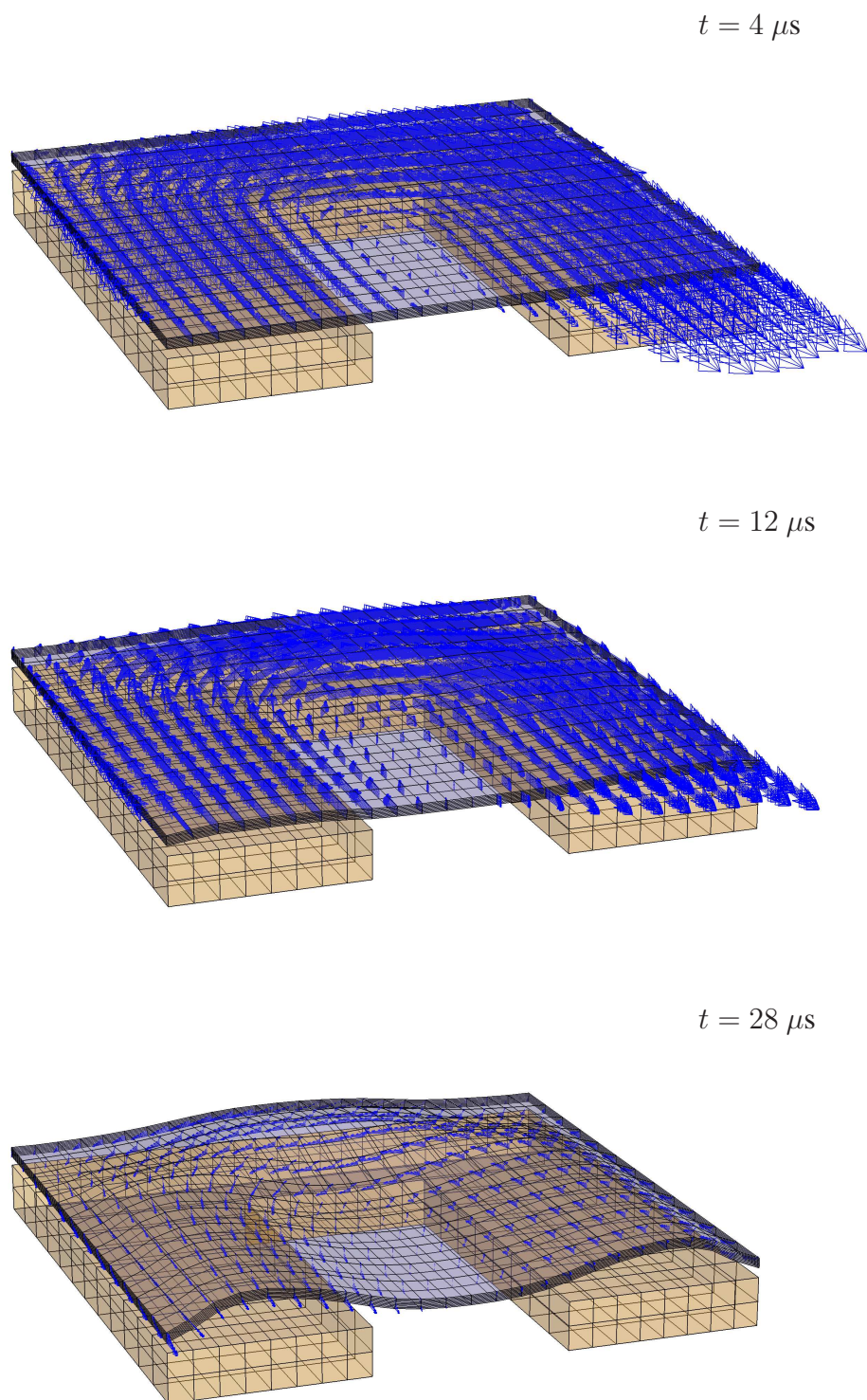


Figure 4.28: Eddy current distribution for the instances $t = 4 \mu s$, $t = 12 \mu s$ and $t = 28 \mu s$. At the beginning of the process the increase of b in the air results in high values for the induced eddy currents at the surface of the sheet metal. At later instances b increases inside the sheet and leads to a more homogenous eddy current distribution in thickness direction.

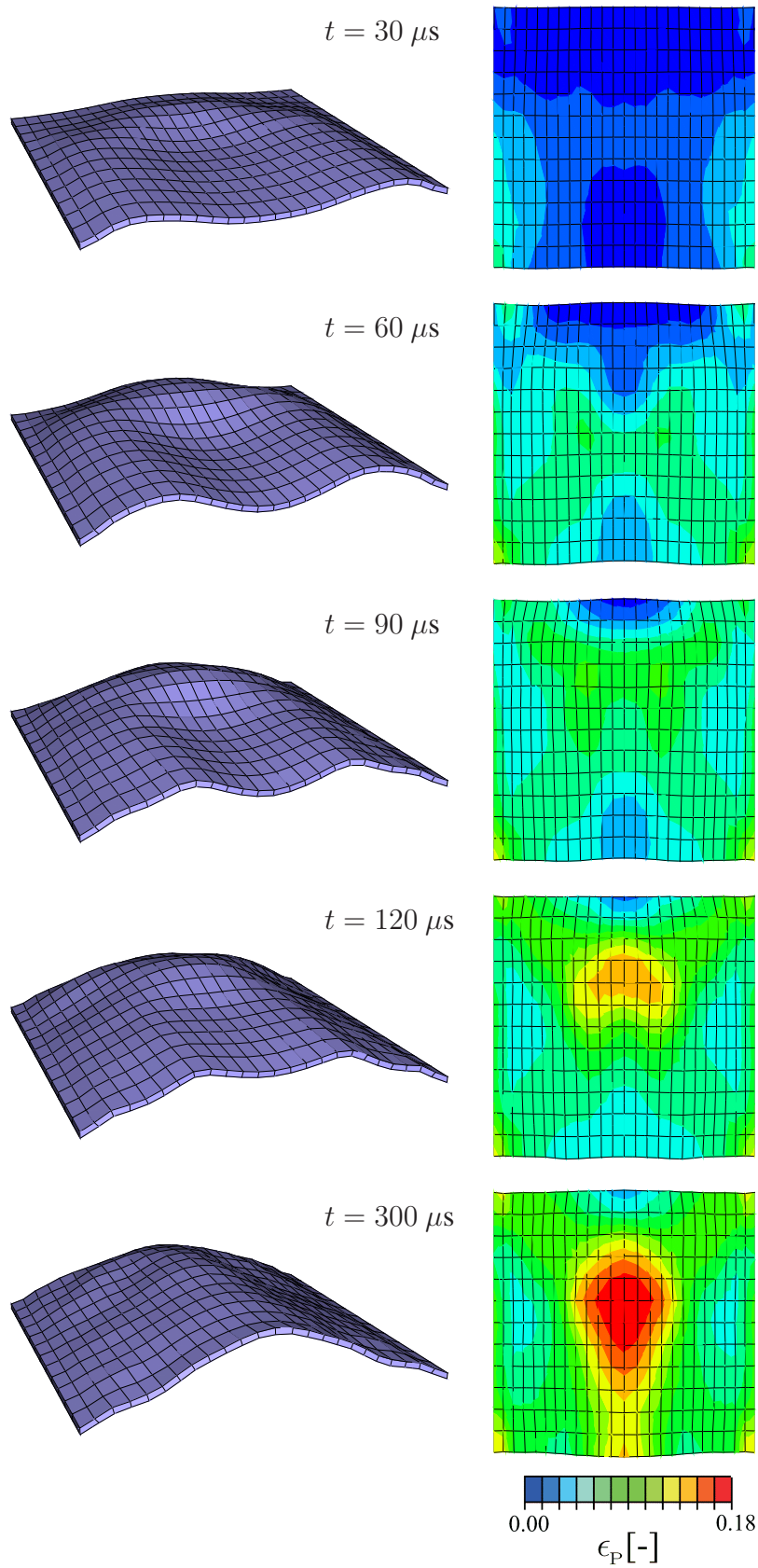


Figure 4.29: Forming stages of the sheet metal as a function of time and corresponding top view contour plots of ϵ_p . Initially, the part of the sheet metal located directly above the tool coil is subject to large induced Lorentz forces and begins to accelerate. As forming proceeds, this part pulls the center of the plate along with it.

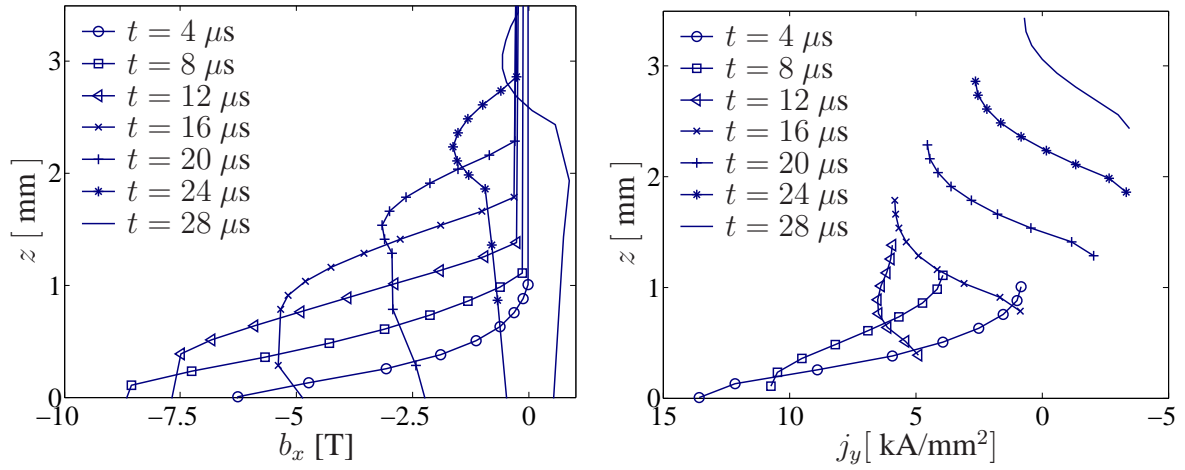


Figure 4.30: Development of b_x and j_y along PZ with evolving time and deformation. Left: The development of b_x in the sheet and surrounding air. Right: Development of eddy currents in the sheet. Curves for j_y move according to the vertical deformation of the sheet.

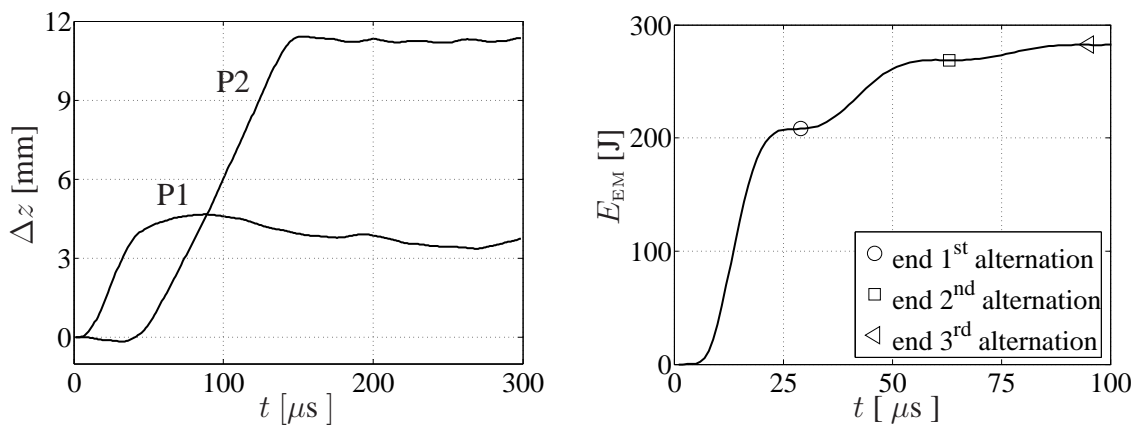


Figure 4.31: Development of vertical deformation at points P1 and P2 (left). Energy transferred to the mechanical system in terms of total energy $E_{EM}(t)$ (right). The ends of the alternations of the input current I are highlighted.

4.9 Conclusions

In contrast to 2D modeling of axisymmetric EMF processes, 3D process models exhibit large computational costs. However, in the present work it could be shown how a carefully chosen discretization of typical features of the EMF setup can lead to an improvement and simplification of the modeling of EMF. The mesh evaluation was done by selectively studying the convergence of eddy currents and magnetic flux density in the sheet metal with respect to particular discretization parameters that characterize the finite element mesh of a specific feature. The study of convergence of typical *vertical* mesh parameters indicated that a very low number of element layers can be chosen for the air gap between the sheet metal and the air above the sheet metal. Physical reasons for these findings can be attributed to the homogeneous distribution of the magnetic flux density in the air gap and the insignificantly low field strength above the sheet metal. Inside the sheet metal a large number of element layers is required to render the strong variations of the eddy currents and magnetic flux densities in thickness direction during the forming process. The study of the horizontal mesh parameters and the size of the bounding box, which determines the extent of the electromagnetic field, facilitate a further reduction of computational cost without significant loss of accuracy.

To model the mechanical deformation of the sheet metal stabilized solid shell finite elements (Reese, 2007) are applied. Evidently, here the sheet metal is discretized with *one* element layer in thickness direction. To be able to deal with the different vertical discretizations of the mechanical and the electromagnetic mesh, the Lorentz body force distribution in the solid shell element is integrated separately from its purely mechanical part. Here, a large number of electromagnetic finite elements which are contained inside the solid shell element is one condition to obtain an accurate nodal representation of the electromagnetic loads. Secondly, a sufficiently high number of Gaussian points in the solid shell element has to be provided to be able to deal with strong variations of the Lorentz force in thickness direction.

The third measure to reduce the computational cost is based on the fact that the electromagnetic part of the model becomes less significant with each diminishing amplitude of the input current. After some time the forming operation is basically driven by the conversion of kinetic energy into inelastic deformation. This motivates the development of a termination criterion for the electromagnetic part of the model. Results for the energy transferred from the electromagnetic to the mechanical system denoted by $E_{EM}(t)$ indicate that approximately 98 % of $E_{EM}(t)$ is added to the mechanical system after the first three alternations. In particular during the first alternation, where both, the velocity of the sheet metal and the Lorentz forces are maximal, most of $E_{EM}(t)$ is added to the mechanical system. The electromagnetic part of the simulation is terminated if the amount of energy added to the mechanical system during the last alternation falls below some reference value which is based on the first alternation. Together with the above discussed measures this leads to a reduction of the computation time to 6.5 %.

After evaluation and development of the model simplifications, results for a relatively simple 3D EMF setup consisting of a square shaped sheet metal and an angled tool coil were computed. For the given input current and tool coil geometry detailed insight with respect to the development of eddy currents, magnetic field and deformation of the sheet metal can be provided. A qualitative interpretation of the electromagnetic results succeeds in the context of Maxwell's

equations. At the beginning of the process both the electromagnetic and the mechanical part of the model are crucial for the forming operation. Only if eddy currents, magnetic field and the velocity of the sheet metal are significant, the electromagnetic forming operation becomes efficient in terms of the employed energy. Based on the above developed simplifications and research experiences future work is focused on more complex forming geometries and sophistication of modeling approaches (see figures A.4 and A.5). From a technological point of view the above investigations for $E_{EM}(t)$ motivate the further study of possible input current modifications with respect to an improvement of energy efficiency.

Appendix A

Technical realization of automatic pre- and postprocessing of parametric 3D models for electromagnetic forming

Abstract – Besides the theoretical and numerical issues involved with the modeling and simulation of electromagnetic forming (EMF) a more technical issue is related to the treatment of complex 3D forming setups in terms of their geometric representation and finite element meshing. To model and mesh complex 3D parts, the application of a powerful pre- and postprocessing software becomes necessary. Due to its Python based interfaces the commercial software tool ABAQUS seems to be a good choice in this regard. In particular the implementation of model scripts in ABAQUS for an automated and parametric creation of EMF model setups is demonstrated. Further, it is shown how the ABAQUS pre- and postprocessing capabilities are combined with in-house implementations of the algorithmic concepts particularly suitable to simulate EMF processes. Data transfer modules and their interrelation are discussed and documented.

A.1 Introduction

As discussed in Chapter 4, 2D FEM modeling of EMF has been applied to simulate research problems which consist of simple structures and exhibit rotational symmetry. In the industrial context, applications consist of non-symmetric more complex problems which still lack a proper 3D modeling approach. It is an objective to develop a software tool capable of 3D modeling and simulation of the aforementioned EMF processes. Here, the development and implementation of numerical methods, particularly suitable to deal with the coupled magneto mechanical problem at large inelastic deformations is one of many issues involved. This is discussed in chapters 1 and 4.

A more technical issue is related to the treatment of complex 3D structures and EMF setups in terms of their geometric representation and finite element meshing. To model and mesh complex 3D parts the application of a powerful preprocessing software becomes necessary. Moreover, to be able to deal with the large amount of data received after process simulation, an equally powerful postprocessing software is required. The commercial software tool ABAQUS seems to be a good choice in this regard. ABAQUS provides well documented Python interfaces to import and export finite element mesh data including field results and has powerful, sophisticated and reliable meshing and visualization tools. It is in particular the accessibility for importing and exporting data, which qualifies ABAQUS for the task. In the aforementioned context the objective of this work represents the following points:

*Schmaling and Unger (2007)

1. The technical realization of individual modeling modules and connection of the data flow between the modules. The modules consist of ABAQUS-, Python- and MATLAB programs.
2. The creation of several EMF models in ABAQUS and their parametric automation.

Following the natural order of the above listed tasks, in Section A.2 the data flow and all involved modeling modules are discussed and illustrated. Furthermore, related module descriptions and data names are documented. In Section A.3 the generation of four different models in ABAQUS is discussed. Those models differ with respect to their complexity starting with a simple cylindrical rod and ending with an EMF forming setup with a flat coil that involves a number of windings. Particular features and difficulties related to the generation of these models are discussed and model parameters are documented.

A.2 Python based modeling modules and dataflow

Common to other finite element simulations the modeling of a particular EMF process consists of a preprocessing step, in which the process geometry and finite element meshes are generated, a solution step, where based on the numerical scheme applied a solution is computed and a postprocessing step, in which the solution results are visualized. As mentioned above for the pre- and postprocessing of the simulation, the commercial code ABAQUS was used while the actual process solution was obtained on the basis of the in-house implementation of the algorithmic concepts discussed in chapters 4 and 1 and in (Stiemer et al., 2006b). Since model data generated with ABAQUS cannot be utilized directly for the in-house implementation, a number of intermediate data formatting steps become necessary. Conversely, results computed with the in-house code need to be formatted so that an importation into the preprocessing modules in ABAQUS becomes feasible. To this end a number of data formatting modules were programmed and are discussed in what follows. Furthermore, a detailed description of the dataflow between the modules is provided.

The organization of the dataflow for a fictitious process model labelled with the name 'Modelname' is illustrated in Figure A.1. In Table A.1 all module names are listed together with the files which are created by each module. At the start, the model geometry and its mesh is created in ABAQUS (see Section A.3 for details) and an input file named 'Modelname.inp' is generated. In particular 'Modelname.inp' contains information regarding sets of nodes or elements which play an important role for the assignment of components, interface and connection surfaces and boundary conditions for the mechanical as well as the electromagnetic mesh (see Table A.2). Next, the 'Modelname.inp' is interpreted with respect to these sets, the nodal coordinates and the connectivity matrix. This is done by the Python script 'ABAQUSinput.py' which creates files for each node or element set as well as for element and nodal data. The separation into different files facilitates the reconstruction of the sets in the postprocessing stage.

The script 'Read_mesh.m' then performs extensive computations to obtain the model data to be read by the coupled MATLAB/FEAP code. Since the solution of the electromagnetic system is done on the basis of *edge* finite elements the reformatting and importation of the element connectivity, nodal coordinates, node and element-sets into MATLAB are not the only tasks to

obtain the data necessary to run the coupled simulation. Edge based elements require a number of additional combinatory information, for instance a number-field that uniquely attributes two element vertices to an edge. Note that the term node for an element vertex in the case of edge based elements is not applicable and therefore replaced by the term vertex. Furthermore, the algorithmic treatment of edge based elements requires an extension of the connectivity matrix where element edge numbers are attributed to global element numbers and a number field where at most six edges are attributed to an element vertex. The computation of this information represents the most time consuming operation within 'Read_mesh.m'. Besides the extraction of combinatory information for edge elements from the ABAQUS input file, further data transformation tasks involve the extraction of data for the mechanical finite element problem and the body force mapping between the electromagnetic and the mechanical system discussed in Section 4.4. For the computation of this information the focus is on the nodes and elements that represent the sheet metal in the model generated in ABAQUS. For the mechanical problem solid shell elements are applied. As discussed in Section 4.4 each mechanical element contains a number of electromagnetic elements that are arranged in layers to resolve the highly nonlinear body force distribution that prevails in vertical direction (see Section 4.8 Figure 4.30). In this regard, from the layered elements in the sheet metal, which were generated in ABAQUS a mechanical finite element mesh has to be extracted with one element layer in thickness direction. This mesh is then formatted and extracted resulting in the FEAP input file 'IModelname'. Furthermore as discussed in Section 4.4 the electromagnetic loads are computed on the basis of the electromagnetic elements that are contained in the mechanical ones. Here, information is needed to be able to attribute body force data to a corresponding mechanical element.

Besides data relevant for the mapping of the body forces with respect to the shell elements, the electromagnetic mesh on the other hand has to be adopted so that it matches the deformed shape of the sheet metal. This requirement is part of the ALE algorithm discussed in Chapter 4 and (Stiemer et al., 2006b). Here, the mechanical deformation of the sheet metal represents a geometric constraint condition for the new element distribution in the surrounding air (see Figure 4.15). There exists no direct deformation data for the electromagnetic elements which are contained in the mechanical solid shell elements. However via relation (4.3) the actual vertex positions of the solid shell element are mapped on the vertices of the contained electromagnetic elements. Relation (4.3) represents a shape function mapping of the actual element positions with respect to the local coordinates attributed to the reference positions of the electromagnetic elements contained in the solid shell element. The local coordinates required for the shape function mapping correspond to the reference configuration of the solid shell element. Their computation can be done at the preprocessing stage of the simulation. After computation of all necessary arrays, finally all aforementioned data is written to a MATLAB data file named 'Modelname.mat' and a corresponding FEAP input file 'IModelname' and the solution module can be started.

At the beginning of a coupled simulation a number of modeling parameters such as e.g. total simulation time, time step, selection of experimental input current data, etc. are set. In particular the model of choice is set by specifying the data file and FEAP input file for the coupled simulation (here 'Modelname.mat' and 'IModelname').

During computation of the fully coupled model, field results for the mechanical as well as

the electromagnetic system are formatted and outputted to ASCII files which can be imported into ABAQUS. Here, field variables of choice are outputted at each simulation instance for the mechanical and the electromagnetic system, respectively. In MATLAB this is done by the function 'prepare4odb.m' and in FEAP at the element level in subroutine 'elmt08.f'. It is important to note that ABAQUS allows for the reimportation of node and element sets via specified filenames. This facilitates the illustration of field values for particular components (*e.g.*, tool coil or sheet metal) by means of the concept of display groups in ABAQUS. Additionally, both the mechanical and the electromagnetic results can be joined for a combined visualization.

Importation of the simulation results is done via the Python script 'create_odb.py'. The simulation results are converted to the files 'Modelname_mag.odb' and 'Modelname_mech.odb' for the magnetic and mechanical results, respectively. Within the visualization module of ABAQUS the results can then be visualized as well as evaluated with a number of different analysis tools. The user is able to create different types of plots, which most commonly are contour and vector plots. Other common postprocessing tasks are creating time/path plots and animated illustrations.

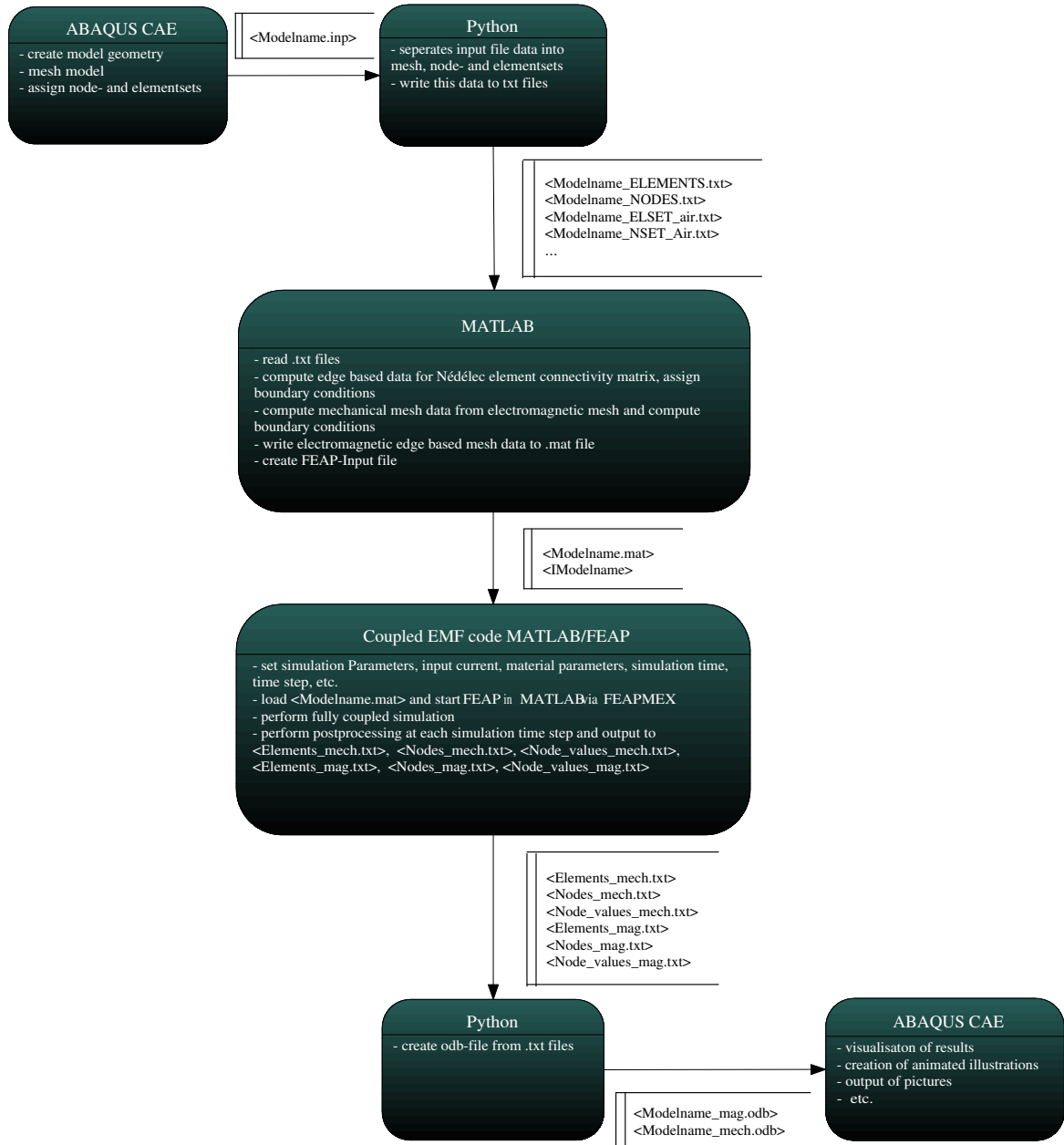


Figure A.1: Illustration of data flow between modeling modules. Each box is attributed to a modeling module, where the basic tasks are summarized. Filenames next to the arrows indicate the data file that is provided for the subsequent module (see Table A.1).

program	corresponding filenames	purpose
ABAQUSInput.py	Mn_ELEMENTS.txt Mn_NODES.txt Mn_ELSET_PART1_Air.txt Mn_ELSET_PART1_Sheet.txt Mn_ELSET_PART1_Tool_coil.txt Mn_NSET_PART1_activation.txt Mn_NSET_PART1_normalization.txt Mn_NSET_PART1_outer_boundary.txt Mn_NSET_PART1_work_piece_boundary.txt Mn_NSET_PART1_zero_Neumann_coil.txt Mn_NSET_PART1_inside_air.txt	Separate mesh data entities from ABAQUS input file.
read_mesh.m	Model_name.mat IModel_name	Compute additional mesh information for edge based elements, data transfer and mechanical model.
prepare4odb.m	Elements_mag.txt Nodes_mag.txt Nodal_field_values_mag.txt	Output of magnetic flux density results ready for importation into ABAQUS.
elmt08.f	Elements_mech.txt Nodes_mech.txt Nodal_field_values_mech.txt	Output of mechanical flux density results ready for importation into ABAQUS.
create_odb.py	Model_name.odb	Create ABAQUS .odb file.

Table A.1: Compilation of module names and corresponding output filenames. Filename extensions indicate the corresponding programming language, program or file format (.py - Python Script, .m - MATLAB Script, .f - FEAP Fortran code, .txt ASCII text file, .mat MATLAB data file, I - FEAP input file, .odb - ABAQUS Model database, Mn - Model name).

A.3 Development of automated parametric EMF models with ABAQUS

Process models that can be automated on the basis of particular geometry and mesh parameters offer many advantages. The special advantage of this approach is demonstrated in Chapter 4 where a study of convergence was performed for the angled tool coil setup depicted in Figure A.3. Here in particular the mesh parameters facilitated a precise and direct specification of the discretization of certain features of the model (see Table A.4). The only action to be taken is the specification of the geometry and mesh parameters at the beginning, subsequently the model is created automatically by ABAQUS ready for simulation. Similarly, in the field of process design a new design geometry simply needs to be specified in terms of its characteristic dimensions and the process model is created. A third important point concerns troubleshooting of the models or modified implementations. In particular the mesh parameters allow for the specification of an extremely coarse meshing of a model which can be computed quickly. As a consequence testing and debugging times are extremely short.

A.3.1 Common modeling features in ABAQUS

Before the features and difficulties of the individual models are discussed, common modeling steps for EMF setups are described. Here, the major steps during creation of the finite element model in ABAQUS CAE in general consist of the following sequence of modeling steps:

1. Creation of the parts tool coil, sheet metal and air,
2. merging of the parts in the assembly module,
3. assignment of arbitrary material parameters,
4. creation of display groups for tool coil, sheet metal and air,
5. assignment of node and element sets,
6. partitioning of the geometry and assignment of edge seeds,
7. meshing of the geometry and verification of meshes and
8. output of the input file.

During the generation of a model the ABAQUS Macro Manager records all actions that were performed. A recorded macro appears in the file 'abaqusMacros.py' where model parameters can be assigned. Common to all EMF models, the three components tool coil, sheet metal and air with their basic geometry are modeled as separate parts. Simple tool coil models and the sheet metal can be modeled by extrusion of 2D drawings. The surrounding air can be modeled arbitrarily. For setups which closely match an axisymmetric geometry a cylindrical volume is usually formed. These parts are then put together and merged in the assembly module. By choosing the option to retain intersecting boundaries, all parts can still be identified and do not form a single part. Additionally, the parts have to be dependent parts which in ABAQUS terminology basically means that meshing is carried out for the complete assembly and not for each part separately. This will result in a compatible mesh, i.e. elements on the intersecting

boundary are sharing the same nodes. Next, material parameters are defined as the python script 'ABAQUSInput.py' requires the keyword 'Material' in the ABAQUS Input file in order to be able to divide the model into the three parts and write the information to separate files (see Figure A.1 and Table A.1). Typically, tool coil, sheet metal and air are chosen to be single sections. In the section assignment manager the material properties can be applied to each section. The material parameters will not be used in the simulation and do not affect the results.

The next step is the creation of display groups. These are created not merely for the purpose of visualization, but rather they enable the user to subsequently create node and element sets. By plotting only the relevant part to the viewport it is possible to select the specific surfaces of the assembly. With the help of the display groups tool the user first assigns display groups to the parts tool coil and sheet metal. The air is produced using Boolean operations. The labeling of these display groups is chosen in accordance with the subsequent python script 'ABAQUSInput.py'.

After the creation of display groups the generation of node and element sets becomes feasible. The proper assignment of such sets is crucial for the subsequent simulation of the EMF setup. They are listed in Table A.2 and are common to all EMF models. The sets are attributed to various aspects of the modeling of the EMF process which are described below. Here, the main purpose to label elements is to distinguish between regions with different material properties. In contrast to the air where the development of the electromagnetic fields is governed by an elliptic equation, coil and sheet metal elements exhibit a large conductivity, which necessitates the consideration of the diffusive parabolic character of the describing field equation. In addition to the assignment of the conductivity, the element labels facilitate the visualization of different entities of the electromagnetic system. Node sets are created to implement boundary conditions for the scalar potential (see 'Activation', 'Normalization', 'Zero_Neumann_coil' and 'Inside_coil' in Table A.2) and the vector potential (see 'Outer_boundary' in Table A.2).

Although it is possible to create node and element sets directly in the mesh module, the mesh and as a consequence the node numbering changes if different parameters are input at the beginning of an ABAQUS script and model dimensions are changed. Thus, every node and element set is specific and mesh-related for every setup of the finite element model. It is therefore preferred to create *geometry sets*, which automatically produce a corresponding node and element set in the final input file. The creation of node and element sets via geometry sets instead of a direct creation is a major advantage, which as a result makes the automation possible.

Next, the forming setup has to be prepared for meshing by means of partitioning and application of edge based mesh seeds. Here application of edge seeds facilitates the specification of the number of elements along a particular edge and thus allows for the implementation of a parameter which characterizes a particular mesh feature. The mesh partitions basically subdivide particular geometry features which simplifies the automatic meshing and provides for a mesh with a good quality (similar element edge lengths, no mesh distortion etc.). Good partitioning creates an even and well-formed mesh. Bad partitioning likely produces a distorted and inappropriate mesh and can cause the meshing algorithm or the following solution code to fail. Due to their geometrical features with tetrahedral elements it is possible to mesh complex structures

Node and element set name	Purpose
Activation	These nodes define the Neumann conditions for the finite element problem of the scalar potential corresponding to the imposed electric current in normal direction of connection surface.
Normalization	These nodes define the Dirichlet conditions for the finite element problem of the scalar potential of the other connection surface (grounding).
Zero_Neumann_coil	These nodes define the Neumann conditions for the finite element problem of the scalar potential. There is no electric current in normal direction of coil surface.
Inside_coil	These nodes define the finite element problem for the solution of the scalar potential. They represent the free nodes.
Inside_air	These nodes are inside the air (not member of boundary or coil etc.). They are needed to define nodes that can be adopted according to the Lagrangian smoothing and ALE algorithm. Further they define edges that are not on the boundary of the system.
Inside_work_piece	These nodes are inside the sheet.
Work_piece_boundary	These nodes are on the boundary of the sheet
Outer_boundary	These nodes define edges that are at the boundary. For the corresponding degrees of freedom (integral means of edges) homogeneous Dirichlet conditions are applied.
Tool_coil	These elements represent the tool coil.
Sheet	These elements represent the sheet metal.
Air	These elements represent the air.

Table A.2: Node and element sets which represent surfaces or element groups which correspond to certain material properties and boundary conditions.

without extensive partitioning. However, these have not been implemented in the solution algorithm. Rather hexahedral edge based finite elements are utilized. Using this element type complex structures have to be thoroughly partitioned. The meshing algorithm frequently produces irregular and unusable meshes and must therefore be analyzed for a number of possible errors. It is checked for gaps and intersections since this is a very common error. In addition, meshing sometimes produces impracticable elements, which can be examined in the mesh verification dialog specifying different criteria, e.g. element distortion and element length ratios. If the mesh fulfills all criteria a job is created and an input file is written.

As mentioned above all models listed below are fully automated and parameterized. Parameter values can be changed via various input dialogs at the beginning of a macro. Meaning

of particular parameters and their illustration can be found below (see tables A.3, A.4, A.5 and A.6).

A.3.2 Cylindrical rod for test and verification purposes

This model allows for testing and verification of the numerical implementation of the 3D model by means of simple analytical solutions (see Appendix B). Wire and air are modeled forming two cylinders which are merged in the assembly module. The easy modeling of the cylindrical wire does not require complex partitions and edge seeds. The partitions of this model are created merely to provide the necessary edges to which the seeds can be applied. Display groups, node and element sets are created as explained before. Edge seeds are applied in radial direction for specifying the number of elements and radial bias in coil and air. In vertical direction the seeds determine the number of elements along the length of the rod. In Figure A.2 and Table A.3 the setup is depicted and geometry and mesh parameters of the automated design are listed.

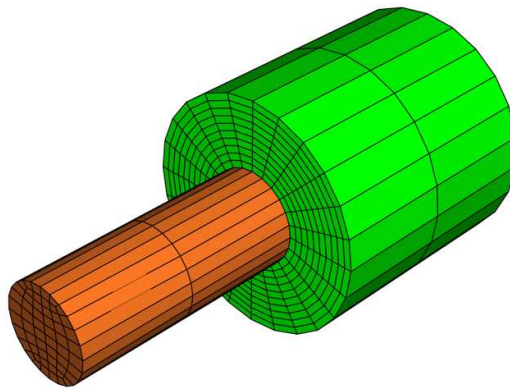


Figure A.2: Illustration of the cylindrical rod to test and verify the numerical implementation of the 3D model by means of analytic solutions. The left half of the air was removed for illustration purposes.

Parameter	Python variable
Radius of wire	wire_radius
Radius of outer boundary	boundary_radius
Length (z-direction)	length
Number of elements in wire (r-direction)	wire_elements
Number of elements in outer boundary (r-direction)	boundary_elements
Number of elements (z-direction)	length_elements
Global elements size	global_element_size

Table A.3: Geometry and mesh parameters in ABAQUS graphical user interface and the Python macro 'wire'.

A.3.3 Forming setup with angled tool coil and square shaped sheet metal

The angled tool coil is particularly suitable to perform a study of convergence for various characteristic features of the forming setup and to gain an understanding of the convergence behavior with respect to a particular feature. Because of its cubic structure it is possible to exactly control the number of elements and modify them. Mesh parameters introduced in Section 4.3 can directly be attributed to the parameters listed in Table A.4. This forming setup is best created by a cube that is partitioned in a way that the resulting partitions form the components of the tool coil and sheet. Further, additional partitions have to be included to ensure that no distorted elements appear. In Figure A.3 an engineering drawing and an illustration of the meshed setup is provided. The dimensions depicted correspond to those of the model simulated in Chapter 4.

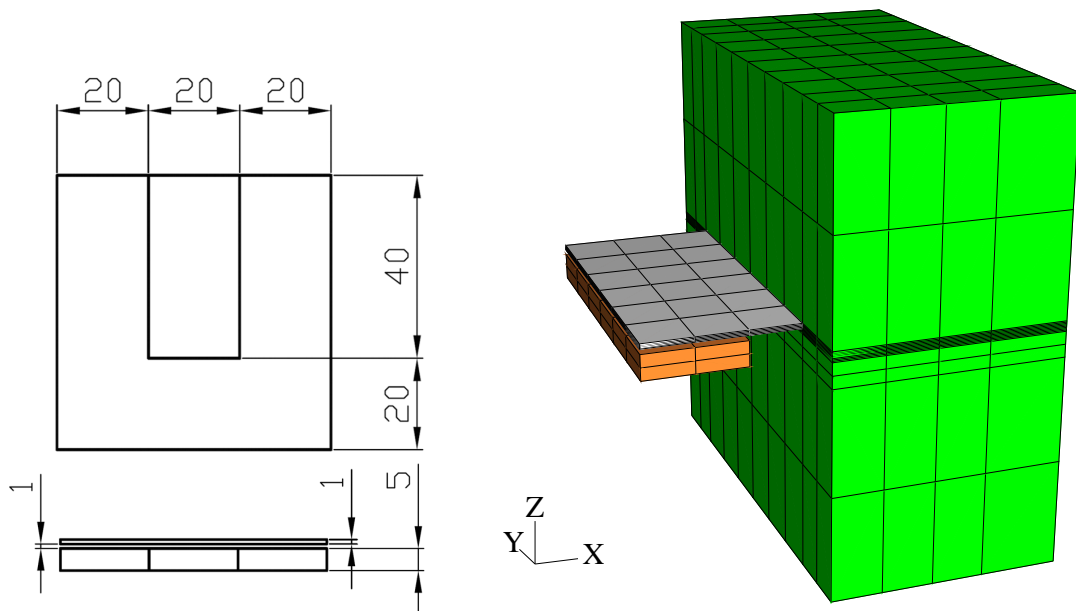


Figure A.3: Left: Engineering drawing of the angled tool coil and upper work piece. Right: Discretized forming model with illustration of tool coil, sheet metal and surrounding air (only right half of air is displayed).

Parameter	Python variable
Width of the Tool Coil (x-direction)	tool_coil_x
Height of the Tool Coil (z-direction)	tool_coil_z
Sheet Width (x-direction)	sheet_x
Sheet Depth (y-direction)	sheet_y
Sheet Thickness (z-direction)	sheet_z
Width of Outer-Boundary (x-direction)	boundary_x
Depth of Outer-Boundary (y-direction)	boundary_y
Height of Outer-Boundary (z-direction)	boundary_z
Air Gap (z-direction)	airgap
Boundary elements (x-direction)	bound_elem_x
Tool Coil Elements (x-direction)	tool_coil_elem_x
Mid Part Elements (x-direction)	mid_part_elem_x
Lower Air Elements (z-direction)	lower_elem_z
Tool Coil Elements (z-direction)	tool_coil_elem_z
Air Gap Elements (z-direction)	air_gap_elem_z
Sheet Elements (z-direction)	sheet_elem_z
Upper Air Elements (z-direction)	upper_elem_z
Global Element Size	global_element_size

Table A.4: Geometry and mesh parameters in ABAQUS graphical user interface and the Python macro 'Quadratic_Coil'.

A.3.4 Forming setup with elliptical coil consisting of one winding

The model with an elliptical tool coil is a further example of a relatively simple forming setup. The elliptical coil is specified by its major and minor axis and thickness (see Figure A.4). To be able to implement the input current at the connection surfaces (see 'Activation' and 'Normalization' in Table A.2 and Figure 4.1), an opening of the tool coil has to be provided. The special case of a *circular* tool coil is obtained by equating the model parameter 'Semi-major axis of ellipse (r)' with 'Semi-minor axis (r)' (see Table A.5). This model quite closely resembles the axisymmetric case. In this regard it facilitates a direct comparison of the successfully applied axisymmetric model (Stiemer et al., 2006a). At the same time this model geometry is relatively simple and can be meshed with a reasonable amount of elements (about five to twenty thousand).

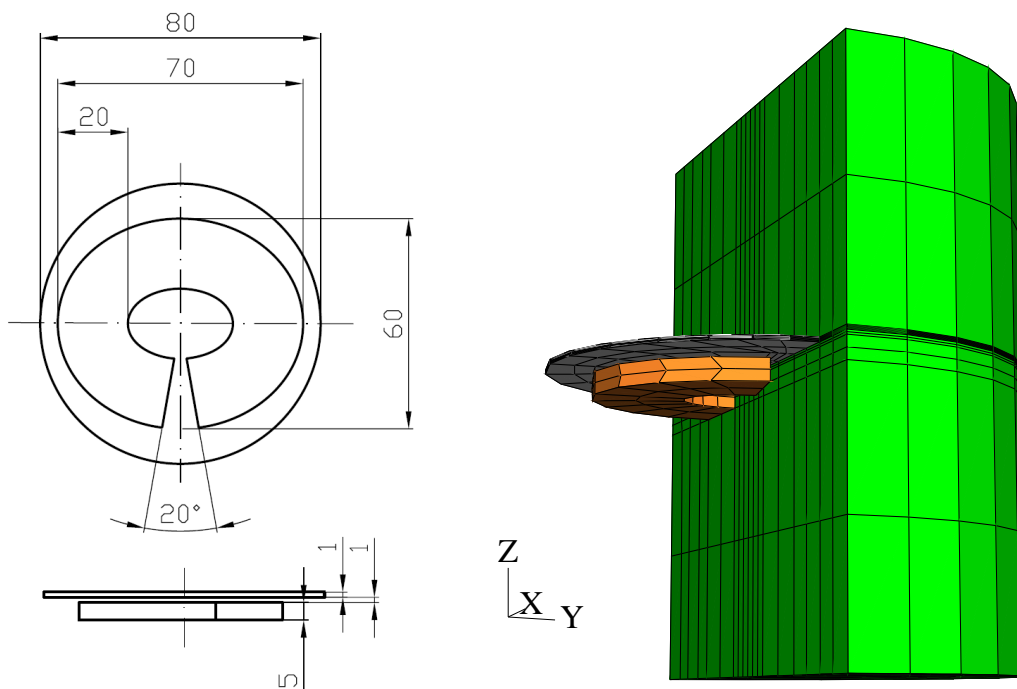


Figure A.4: Left: Engineering drawing of the elliptical tool coil and sheet metal. Right: Discretized forming model with illustration of tool coil, sheet metal and surrounding air (only right half of air is displayed).

Dimension (direction)	Variable name
Semi-major axis of ellipse (r)	Major
Semi-minor axis (r)	Minor
Total opening of ellipse (phi)	Opening
Sheet Thickness (z)	Thickness
Height of Tool Coil (z)	height_tool_coil
Sheet Radius (r)	Radius
Sheet Thickness (z)	sheet_thickness
Air Gap (z)	airgap
Outer Air radius (r)	Outer
Upper Air (z)	Upper
Lower Air (z)	Lower
Sheet Mesh radial Bias (r)	sheet_bias
Sheet Elements (r)	sheet_elements
Outer Mesh Bias (r)	outer_air_bias
Outer Mesh Elements (r)	outer_air_elements
Tool Coil Elements (r)	tool_coil_elements_radial
Tool Coil Elements (z)	tool_coil_elements_height
Upper Air Elements (z)	upper_air_elements
Lower Air Elements (z)	lower_air_elements
Air Gap Elements (z)	air_gap_elements
Sheet Mesh Bias (z)	sheet_bias_height
Sheet Elements (z)	sheet_elements_height
Global Seed (z)	global_seed

Table A.5: Geometry and mesh parameters in ABAQUS graphical user interface and the Python macro 'Elliptical_Coil'.

A.3.5 Forming setup with coil consisting of n windings

This forming setup can be attributed to common experimental forming setups (see, *e.g.*, Beerwald (2004); Mamalis et al. (2004)). Here, the experimental results could successfully be modeled by means of axisymmetric models with the help of a torus approximation of the spiral coil (Stiemer et al., 2006a). To fully evaluate the deviations induced by this approximation the 3D model depicted in Figure A.5 was created. In contrast to the above discussed models the geometrical complexity of the setup leads to a significantly higher number of elements. Here, coils that exhibit more than six windings quickly require more than 50 000 elements which corresponds to about 150 000 degrees of freedom. Further, partitioning of this model is a relatively complex and time-consuming operation. Depending especially on the number of windings, the partitioning for the tool coil may take up to two hours on a modern PC.

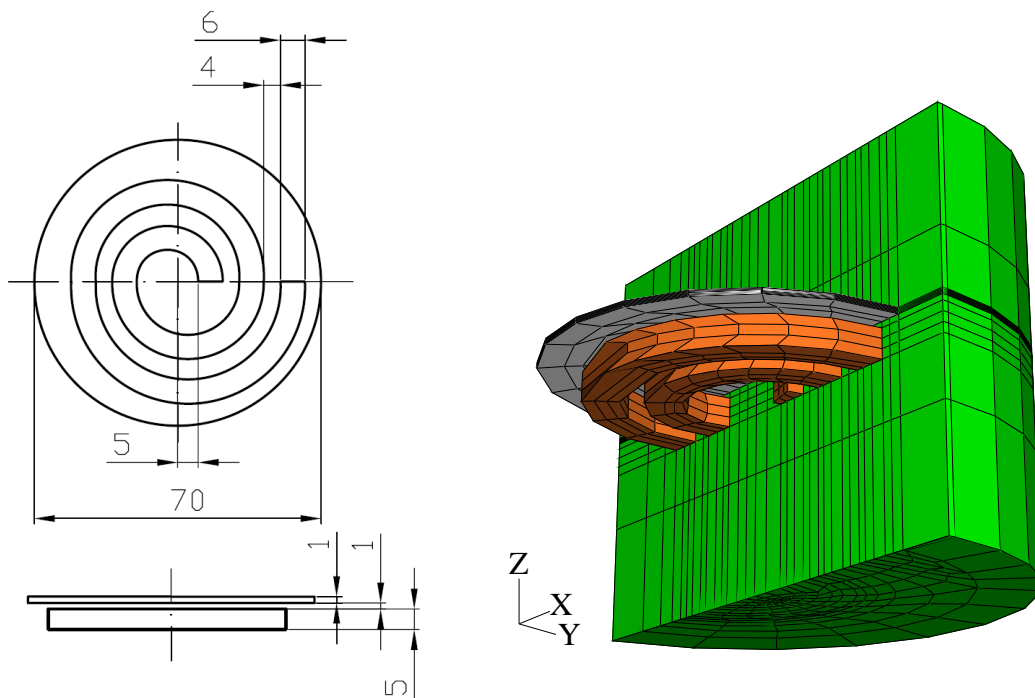


Figure A.5: Left: Engineering drawing of the spiral tool coil and sheet metal. Right: Discretized forming model with illustration of tool coil, sheet metal and surrounding air (only right half of air is displayed).

Parameter	Python variable
Inner radius of the coil	start_radius
Pitch of a single winding	pitch
Thickness of tool coil (r-direction)	rdim
Height of tool coil (z-direction)	zdim
Increment for modeling of sweep profile	delta_phi
Number of windings	windings
Radius of sheet metal	radius
Thickness of sheet metal	sheet_thickness
Thickness of air gap	airgap
Outer air radius	outer
Upper air (z-direction)	upper
Lower air (z-direction)	lower
Sheet mesh bias (z-direction)	sheet_bias_height
Sheet elements (z-direction)	sheet_elements_height
Tool coil elements (z-direction)	tool_coil_elements_height
Upper air bias (z-direction)	upper_air_bias
Upper air elements (z-direction)	upper_air_elements
Lower air bias (z-direction)	lower_air_bias
Lower air elements (z-direction)	lower_air_elements
Air gap elements (z-direction)	air_gap_elements
Outer mesh bias (r-direction)	outer_air_bias
Outer mesh elements (r-direction)	outer_air_elements
Tool coil elements (r-direction)	tool_coil_elements_radial
Global elements size	global_element_size

Table A.6: Geometry and mesh parameters in ABAQUS graphical user interface and the Python macro 'Spiral_Coil'.

Appendix B

Two test examples to verify the implementation of the 2D and 3D electromagnetic models

Abstract – To test and verify the electromagnetic part of the coupled model, results for current flux density and magnetic flux density were computed for two simple axisymmetric setups. For both analytic solutions exist which serve as benchmarks for the results obtained with the numerical models.

B.1 Magnetic flux density distribution for a cylindrical rod with constant current flux density

Consider an axisymmetric cylindrical rod composed of isotropic and homogeneous copper as depicted in the left part of Figure B.1. The rod has a radius of $r_0 = 0.25$ mm. The length l of the rod is chosen so that $l/r_0 \gg 1$ holds. Just as in the case of the electromagnetic forming setup the air surrounding the rod is assumed to exhibit the properties of vacuum. At the boundary ∂R of the system at radius $r = 1$ mm again homogeneous Dirichlet boundary conditions for \mathbf{a} are imposed. Inside the cylinder a constant electric current flux density of $\mathbf{j} = (0, 0, 5.1)$ kA mm⁻² is applied corresponding to an input current of $I = 1$ kA.

Evaluation of Maxwell's equations of the above discussed setup in cylindrical coordinates (r, φ, z) yields

$$\begin{aligned} b_r &= 0, \\ b_\varphi &= \begin{cases} \frac{Ir}{2\pi r_0^2} & , r \leq r_0 \\ \frac{I}{2\pi r} & , r > r_0 \end{cases}, \\ b_z &= 0, \end{aligned} \tag{B.1}$$

for the magnetic flux density \mathbf{b} (see *e.g.* Jackson (1975)). In the right part of Figure B.1 the results for this setup are summarized. Analytic, 2D and 3D model indicate good agreement. Also at ∂R where homogeneous boundary conditions for \mathbf{a} were imposed the results coincide well. It seems that although $\mathbf{a} = \mathbf{0}$, here the spatial derivatives of \mathbf{a} still lead to relatively accurate values for the magnetic flux density via $\mathbf{b} = \text{curl } \mathbf{a}$. At r_0 the 3D model yields slightly smaller values for b_φ than the 2D and the analytic model. This is due to the method by which field quantities for edge based elements are evaluated. From integral means of the vector potential along the element edges (representing the degrees of freedom here) all field values following from \mathbf{a} are computed for the barycenter of the element based on *all* of its edge values. As a result the extreme values of b_φ are slightly reduced.

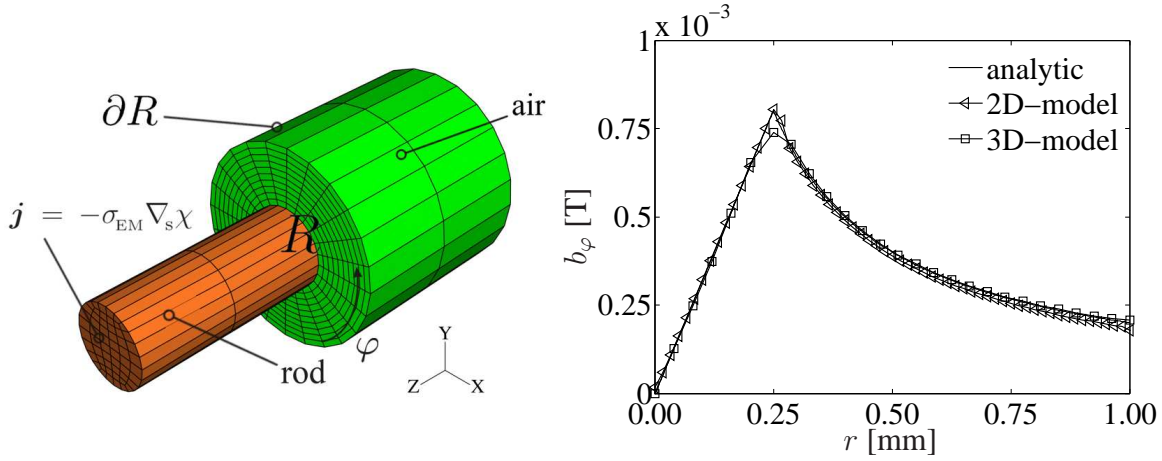


Figure B.1: Left: Illustration of the electromagnetic boundary value problem for a rod with prescribed static current flux density in the rod. Right: Magnetic flux density distribution in circumferential direction for the analytic, 2D and 3D model.

B.2 Transient current flux density in a cylindrical rod

For the same cylindrical rod now transient field distributions persist and the surrounding air is not considered. Here, at $t = 0$ for the entire rod $\mathbf{j} = \mathbf{0}$. And for $t > 0$ at the surface of the rod $\mathbf{j} = (0, 0, 5.0)$ kA mm $^{-2}$ (see left part of Figure B.2). These initial boundary conditions correspond to a suddenly imposed vertical eddy current distribution which is prescribed at $r = r_0$. The solution procedure is analogous to a standard diffusion problem in heat transfer (e.g., (Myers, 1971)) and does not need to be discussed here. The solution can be written as

$$\begin{aligned}
 j_r &= 0, \\
 j_\varphi &= 0, \\
 j_z &= \begin{cases} 0 & , t = 0 \\ \sum_{i=1}^{\infty} \sigma_{EM} \exp(-\kappa_{EM} \lambda_i^2 t) \frac{2J_0(\lambda_i r)}{\lambda_i r_0 J_1(\lambda_i r_0)} & , t > 0 \end{cases}, \quad (B.2)
 \end{aligned}$$

where J_ν represents the Bessel function with order ν and σ_{EM} the electromagnetic diffusivity. Further, λ_i results for the i th root of J_0 with $J_0(\lambda_i r_0) = 0$. The analytical as well as the numerically predicted current flux distributions for the instances $t_1 = 4.5 \times 10^{-9}$ s, $t_2 = 4.5 \times 10^{-8}$ s, $t_3 = 2.0 \times 10^{-7}$ s, $t_4 = 1.0 \times 10^{-6}$ s and $t_5 = 4.5 \times 10^{-6}$ s are depicted in the right part of Figure B.2. For the numerical model the results for each particular instance was obtained by five single simulations namely from $t = 0$ and ending at $t = t_i$. A time step of $t_{n+1,n} = t_i/20\mu$ s was chosen for each simulation. As expected, with increasing time, the fixed eddy current distribution at the surface of the rod diffuses into the rod until saturation. 3D as well as 2D results coincide well with the analytical solution (see also Bilyk et al. (2005)).

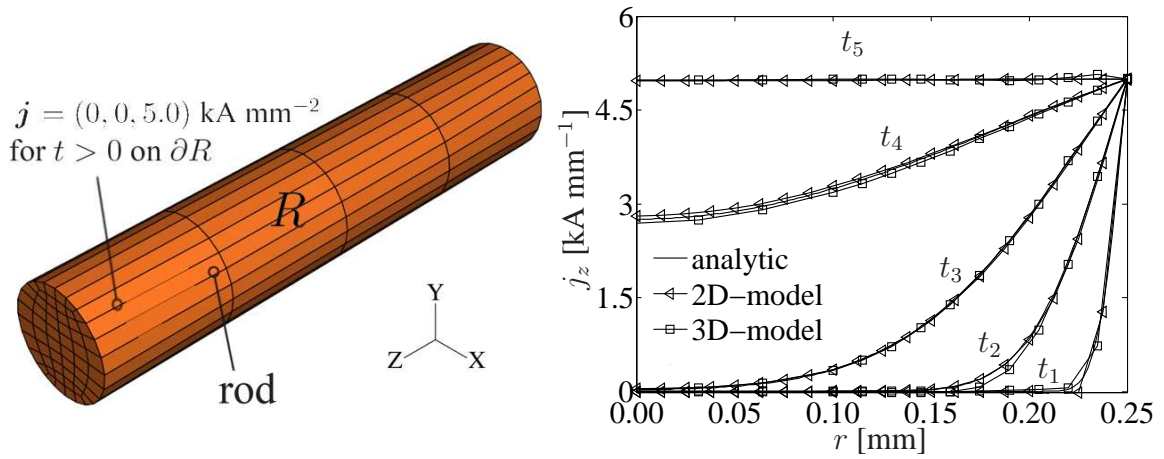


Figure B.2: Left: Illustration of the electromagnetic boundary value problem for a rod with constant current flux density at the surface of the rod which penetrates the rod with increasing time. Right: Current flux density distribution for the instances $t_1 = 4.5 \times 10^{-9}\text{s}$, $t_2 = 4.5 \times 10^{-8}\text{s}$, $t_3 = 2.0 \times 10^{-7}\text{s}$, $t_4 = 1.0 \times 10^{-6}\text{s}$ and $t_5 = 4.5 \times 10^{-6}\text{s}$.

References

- Anca, D., Turek, S., Wan, D., Fictitious boundary and moving mesh methods for the numerical simulation of particulate flow, in Proceedings of ECCOMAS CFD European Conference on Computational Fluid Dynamics, pp. 228–250, Egmond aan Zee, The Netherlands, 2006.
- Badelt, M., Beerwald, C., Brosius, A., Kleiner, M., Process analysis of electromagnetic sheet metal forming by online-measurement and finite element simulation, in Proceedings of 6th International ESAFORM Conference on Material Forming, pp. 123–126, Salerno, Italy, 2003.
- Beerwald, C., Grundlagen der Prozessauslegung und gestaltung bei der elektromagnetischen Umformung, Dr.-Ing. Dissertation, University of Dortmund, Germany, Institute of Forming Technology and Lightweight Construction, 2004.
- Beerwald, C., Brosius, A., Homberg, W., Kleiner, M., Wellendorf, A., New aspects of electromagnetic forming, in Proceedings of 6th International Conference on the Technology of Plasticity, pp. 2471–2476, Erlangen, Germany, 1999.
- Bevington, P. R., Data Reduction and Error Analysis for the Physical Sciences, McGraw-Hill Book Company, 1969.
- Bil, H., Kılıç, S. E., Tekkaya, A. E., A comparison of orthogonal cutting data form experiments with three different finite element models, International Journal of Machine Tools and Manufacture, Volume 44, pp. 933 – 944, 2004.
- Bilyk, S., Ramesh, K., Wright, T., Finite deformations of metal cylinders subjected to electromagnetic fields and mechanical forces, Journal of the Mechanics and Physics of Solids, Volume 53, pp. 525–544, 2005.
- Bolzon, G., Maier, G., Panico, M., Material model calibration by indentation, imprint mapping and inverse analysis, International Journal of Solids and Structures, Volume 41, pp. 2957–2975, 2004.
- Brosius, A., Verfahren zur Ermittlung dehnratenabhängiger Fließkurven mittels elektromagnetischer Rohrumformung und interaktiver Finite-Elemente-Analysen, Dr.-Ing. Dissertation, Universtiy of Dortmund, Germany, Institute of Forming Technology and Lightweight Construction, 2005.
- Bruhns, O. T., Anding, D. K., On the simultaneous estimation of model parameters used in constitutive laws for inelastic material behaviour, Int. J. Plasticity, Volume 15, pp. 1311–1350, 1999.
- Cai, X.-X., Fleitas, B., Jiang, B., Liao, G., Adaptive grid generation based on least-squares finite-element method, Computers and Mathematics with Applications, Volume 48, pp. 1077–1086, 2004.
- Chen, X., Chen, X., Sensitivity Analysis and Determination of Streambed Leakance and Aquifer Hydraulic Properties, Journal of Hydrology, Volume 284, pp. 270–284, 2003.
- Conrad, H., Sprecher, A. F., The electroplastic effect in metals, in Dislocations in solids, pp. 499–541, Elsevier Science Publishers, 1989.

- El-Azab, A., Garnich, M., Kapoor, A., Modeling of the electromagnetic forming of sheet metals: state-of-the-art and future needs, *J. Mat. Process. Tech.*, Volume 142, pp. 744–754, 2003.
- El-Magd, E., Abouridouane, M., Characterization, modelling and simulation of deformation and fracture behaviour of the light-weight wrought alloys under high strain rate loading, *International Journal of Impact Engineering*, Volume 32, pp. 741–758, 2005.
- Fenton, G., Daehn, G. S., Modeling of electromagnetically formed sheet metal, *Journal for Materials Processing Technology*, Volume 75, pp. 6–16, 1998.
- Field, D., Laplacian smoothing and Delaunay triangulations, *Communications in applied numerical methods*, Volume 4, pp. 709–712, 1988.
- Field, J., Walley, S., Bourne, N., Huntley, J., Experimental Methods at High Rates of Strain, *Journal de Physique IV France*, Volume C 8, pp. 3–22, 1994.
- Frost, H. J., Ashby, M. F., Deformation mechanism maps, Pergamon Press, 1982.
- Gelin, J. C., Ghouati, O., An inverse method for determining viscoplastic properties of aluminium alloys, *J. Mater. Process. Technol.*, Volume 45, pp. 435–440, 1994.
- Gilat, A., Clifton, R. J., Pressure-shear waves in 6061-T6 aluminum and alpha-titanium, *Journal of the Mechanics and Physics of Solids*, Volume 33, pp. 263–284, 1985.
- Goldman, P. D., Motowidlo, L. R., Galligan, J. M., The Absence of an Electroplastic Effect in Lead at 4.2 K, *Scripta Metallurgica*, Volume 15, pp. 353–356, 1980.
- Gourdin, W. H., Analysis and assessment of electromagnetic ring expansion as a high-strain rate test, *Journal of Applied Physics*, Volume 65, pp. 411–422, 1989.
- Gourdin, W. H., Weinland, S. L., Boling, R. M., Development of the electromagnetically-launched expanding ring as a high strain-rate test, *Review of Scientific Instruments*, Volume 60, pp. 427–432, 1989.
- Gray, G., Classical Split-Hopkinson Pressure Bar Testing, in *Mechanical Testing and Evaluation Handbook*, American Society of Metals, 2000.
- Harth, T., Schwan, S., Lehn, J., Kollmann, F. G., Identification of material parameters for inelastic constitutive models: statistical analysis and design of experiments, *International Journal of Plasticity*, Volume 20, pp. 1403–1440, 2004.
- Hauser, F. E., Techniques for measuring stress-strain. relations at high strain rates, *Exp. Mech.*, Volume 6, pp. 365–402, 1966.
- Hughes, T. J. R., *The Finite Element Method*, Prentice-Hall, 1987.
- Imbert, J., Winkler, S., Worswick, M., Oliveira, D., Golovashchenko, S., Numerical Modeling of an Electromagnetic Corner Fill Operation, in *Proceedings of NUMIFORM 2004*, pp. 1833–1839, Ohio State University, USA, 2004.
- Jackson, J. D., *Classical Electrodynamics*, John Wiley and Sons, 1975.
- Jiang, B., Wu, J., Povinelli, L. A., The origin of spurious solutions in computational electromagnetics, *Journal of computational physics*, Volume 125, pp. 104–123, 1996.

- Jones, N., *Structural Impact*, Cambridge University Press, 1997.
- Kajberg, J., Sundin, K. G., Melin, L. G., Stahle, P., High strain-rate tensile testing and viscoplastic parameter identification using microscopic high-speed photography, *Int. J. Plasticity*, Volume 20, pp. 561–575, 2004.
- Kleiber, M., *Parameter Sensitivity in Nonlinear Mechanics*, John Wiley & Sons, 1997.
- Kleiner, M., Brosius, A., Blum, H., Suttmeier, F. T., Stiemer, M., Svendsen, B., Unger, J., Reese, S., Benchmark problems for coupled electromagnetic-mechanical metal forming processes, *Annals of the German Society for Production Engineering (WGP)*, Volume 9, pp. 1–16, 2004.
- Kleinermann, J. P., Ponthot, J. P., Parameter identification and shape/process optimization in metal forming simulation, *J. Mat. Process. Tech.*, Volume 139, pp. 521–526, 2003.
- Klepaczko, J., Malinowski, Z., Dynamic frictional effects as measured from the split Hopkinson pressure bar, in *High Velocity Deformation of Solids*, pp. 403–416, 1978.
- Kocks, U. F., Mecking, F., The physics and phenomenology of strain hardening: the FCC case, *Progress in Material Science*, Volume 98, pp. 171–273, 2003.
- Kolsky, H., An investigation of the mechanical properties of materials at very high rates of loading, *Proc. Phys. Soc.*, Volume B 62, pp. 676–700, 1949.
- Kompalka, A., Reese, S., Bruhns, O. T., Experimental investigation of damage evolution by data-driven stochastic subspace identification and iterative finite element model updating, *Archive of Applied Mechanics*, published online, 2007.
- Lemaitre, J., Chaboche, J.-L., *Mechanics of Solid Materials*, Cambridge University Press, 1990.
- Lindholm, U. S., Yeakley, L. M., Dynamic deformation of single and polycrystalline Aluminium, *J. Mech. Phys. Solids*, Volume 13, pp. 41–53, 1964.
- Mahnken, R., A comprehensive study of multiplicative elastoplasticity coupled model coupled to damage including parameter identification, *Computers & Structures*, Volume 74, pp. 179–200, 2000.
- Mamalis, A., Manolakos, D., Kladas, A., Koumoutsos, A., Electromagnetic forming and powder processing: Trends and developments, *Appl. Mech. Rev.*, Volume 57, pp. 299–324, 2004.
- Meister, A., *Numerik linearer Gleichungssysteme*, Vieweg, 1999.
- Meyers, M. A., *Dynamic Behavior of Materials*, John Wiley & Sons, 1994.
- Molotskii, M., Theoretical basis for electro- and magnetoplasticity, *Materials Science & Engineering*, Volume 287, pp. 248–258, 2000.
- Moon, F., *Magnetic interactions in solids*, Springer-Verlag, 1980.
- Myers, G. E., *Analytical Methods in Conduction Heat Transfer*, McGraw-Hill Book Company, New York, 1971.
- Nédélec, J. C., Mixed Finite Elements in \mathbb{R}^3 , *Numerische Mathematik*, Volume 35, pp. 315–341, 1980.

- Nédélec, J. C., A New Family of Mixed Finite Elements in \mathbb{R}^3 , *Numerische Mathematik*, Volume 50, pp. 57–81, 1986.
- Okazaki, K., Kagawa, M., Conrad, H., Effects of strain rate, temperature and interstitial content on the electroplastic effect in titanium, *Scripta Metallurgica*, Volume 13, pp. 473–477, 1979.
- Oliveira, D., Worswick, M., Finn, M., Finite Element Modelling of the Electromagnetic Forming of Aluminum Alloy Sheet, in *Proceedings of 4th International ESAFORM Conference on Material Forming*, pp. 773–776, Liège, Belgium, 2001.
- Poljak, D., Doric, V., Vucicic, D., Brebbia, C., Boundary element modeling of radio base station antennas, *Engineering Analysis with Boundary Elements*, Volume 30, pp. 419–425, 2006.
- Press, W. H., Teukolsky, S. A., Vetterling, W. T., Flannery, B. P., *Numerical Recipes in C++*, Cambridge University Press, 2002.
- Reese, S., A large deformation solid-shell concept based on reduced integration with hourglass stabilization, *International Journal for Numerical Methods in Engineering*, Volume 69, pp. 1671–1716, 2007.
- Reese, S., Svendsen, B., On the modeling of internal variables as structure tensors in anisotropic, finite-deformation inelasticity, *J. de Physique IV*, Volume 14, pp. 31–37, 2003.
- Reese, S., Svendsen, B., Stiemer, M., Unger, J., Schwarze, M., Blum, H., On a new finite element technology for electromagnetic metal forming processes, *Archive of Applied Mechanics (Ingenieur Archiv)*, Volume 74, pp. 834–845, 2005.
- Rosakis, P., Rosakis, A. J., Ravichandran, G., Hodowany, J., A thermodynamic internal variable model for the partition of plastic work into heat and stored energy in metals, *Journal of the Mechanics and Physics of Solids*, Volume 48, pp. 581–607, 2000.
- Scales, J. A., Smith, M. L., Treitel, S., *Introductory Geophysical Inverse Theory*, Samizdat Press, 2001.
- Scheday, G., *Theorie und Numerik der Parameteridentifikation von Materialmodellen der finiten Elastizität und Inelastizität auf der Grundlage optischer Feldmethoden*, Dr.-Ing. Dissertation, University of Stuttgart, Germany, Institute of Applied Mechanics, 2003.
- Schinnerl, M., Schöberl, J., Kaltenbacher, M., Lerch, R., Multigrid methods for the 3D simulation of nonlinear magneto-mechanical systems, *IEEE Transactions on Magnetics*, Volume 38, pp. 1497–1511, 2002.
- Schmalzing, B., Unger, J., Technical realization of automatic pre- and postprocessing of parametric 3D models for electromagnetic forming, technical report, 2007.
- Simo, J. C., Hughes, T. J. R., *Computational Inelasticity*, Springer, 1998.
- Snieder, R., Trampert, J., *Inverse problems in geophysics*, Dept. of Geophysics Utrecht University, 1991.
- Springmann, M., Kuna, M., Identification of material parameters of the Gurson-Tvergaard-Needleman model by combined experimental and numerical techniques, *Computational Materials Science*, Volume 33, pp. 501–509, 2005.

- Stierner, M., Unger, J., Blum, H., Svendsen, B., Algorithmic formulation and numerical implementation of coupled electromagnetic-inelastic continuum models for electromagnetic metal forming, *Int. J. Numer. Methods Engrg.*, Volume 68, pp. 1301–1328, 2006a.
- Stierner, M., Unger, J., Blum, H., Svendsen, B., Algorithmic formulation and numerical implementation of coupled electromagnetic-inelastic continuum models for electromagnetic metal forming, in *Proceedings of ECCOMAS CFD European Conference on Computational Fluid Dynamics*, pp. 362–382, Egmond aan Zee, The Netherlands, 2006b.
- Svendsen, B., On the modeling of anisotropic elastic and inelastic material behaviour at large deformation, *International Journal of Solids and Structures*, Volume 38, pp. 9579–9599, 2001.
- Svendsen, B., Chanda, T., Continuum thermodynamic modeling and simulation of electromagnetic forming, *Technische Mechanik*, Volume 23, pp. 103–112, 2003.
- Svendsen, B., Chanda, T., Continuum thermodynamic formulation of models for electromagnetic thermoinelastic materials with application to electromagnetic metal forming, *Cont. Mech. Thermodyn.*, Volume 17, pp. 1–16, 2005.
- Takatsu, N., Kato, M., Sato, K., Tobe, T., High-speed forming of metal sheets by electromagnetic forces, *International Journal of the Japanese Society for Mechanical Engineering*, Volume 31, pp. 142–148, 1988.
- Tanaka, M., Dulikravich, G., *Inverse Problems in Engineering Mechanics*, Elsevier Science & Technology Bookstore, 2001.
- Tekkaya, A. E., State-of-the-art of simulation of sheet metal forming, *Journal of Materials Processing Technology*, Volume 103, pp. 14 – 22, 2000.
- Teodosiu, C., Dislocation modeling of crystalline plasticity, in *Large plastic deformation of crystalline aggregates*, pp. 21–80, Springer, 1997.
- Tortorelli, D. A., Michaleris, P., *Design Sensitivity Analysis: Overview and Review*, *Inverse Problems in Engineering*, Volume 1, pp. 71–105, 1994.
- Triantafyllidis, N., Waldenmyer, J. R., Onset of necking in electro-magnetically formed rings, *Journal of the Mechanics and Physics of Solids*, Volume 52, p. 21272148, 2004.
- Troitskii, O. A., Electromechanical effect in metals, *Zh. Eksp. Teor. Fiz.*, Volume 10, pp. 18–22, 1969.
- Unger, J., Stierner, M., Brosius, A., Svendsen, B., Blum, H., Kleiner, M., Inverse error propagation and model identification for coupled dynamic problems with application to electromagnetic metal forming, submitted to *International Journal of Solids and Structures*, 2007a.
- Unger, J., Stierner, M., Schwarze, M., Svendsen, B., Blum, H., Reese, S., Strategies for 3D simulation of electromagnetic forming processes, to be submitted to *Journal of Materials Processing Technology*, 2007b.
- Unger, J., Stierner, M., Svendsen, B., Blum, H., Multifield modeling of electromagnetic metal forming processes, *Journal of Materials Processing Technology*, Volume 177, pp. 270 – 273, 2006a.

- Unger, J., Stiemer, M., Walden, L., Svendsen, B., Blum, H., Bach, F., On the effect of current pulses on the material behaviour during electromagnetic metal forming, in Proceedings of the 2nd International Conference on High Speed Forming, pp. 23–32, Dortmund, Germany, 2006b.
- Varma, S., Cornwell, L. R., The Electroplastic Effect in Aluminum, Scripta Metallurgica, Volume 13, pp. 733–738, 1979.
- Šilhavý, M., The Mechanics and Thermodynamics of Continuous Media, Springer-Verlag, 1997.
- Zabaras, N., Ganapathysubramanian, S., Li, Q., A continuum sensitivity method for the design of multi-stage metal forming processes, International Journal of Mechanical Sciences, Volume 45, pp. 325–358, 2003.

Acknowledgements

The work presented in this thesis was carried out between 2003 and 2007 during my time as a Ph.D. student at the Chair of Mechanics, University of Dortmund. Having come to an end, I would like to express my gratitude to all the people who have given me great support and help in the last four years.

First of all, I would like to thank my academic advisor Professor Bob Svendsen for his dedicated support. His scientific background, ideas and way of thinking made for a great and valuable learning experience. Further, I would like to thank Professor Stefanie Reese, Professor A. Erman Tekkaya and Professor Klaus Thermann for their interest in my work and willingness to act as examiners for this thesis. I wish to thank the German National Science Foundation (DFG) for financial support.

I would like to thank Dr. Marcus Stiemer for an excellent and committed project cooperation and numerous fruitful and interdisciplinary scientific discussions. I would like to thank my colleagues, Andreas Kompalka for friendship and interesting and instructive discussions, Christian Hortig for sharing his straightforward humor with me and for good scientific discussions, Kerstin Walter and Christine Wu for language assistance, help with formal issues and good companionship, Dr. Vladi Levkovitch for his jokes, Dr. Fred Reusch for his helpfulness, Tobias Kayser for his continuous help with software issues, Serkan Ertürk for his friendship and for showing Turkey to me and Benjamin Schmaling and Richard Ostwald for good teamwork and all the other members of the chair for the friendly atmosphere. Also, I would like to express my thanks to the members of the Lehrstuhl für Maschinendynamik, Professor Klaus Thermann, Vadim Palnau and Dr. Andrea Schütze for interesting and entertaining lunchtime discussions.

I would like to thank the members of the research group FOR 443 for good project cooperation, in particular Dr. Alexander Brosius and Désirée Risch for their support regarding experimental and project issues, Marco Schwarze for his support regarding various programming issues and Dr. Meinolf Klocke for helpful discussions concerning the interpretation of electromagnetic simulations.

My special thanks go to my parents, my sister, my grandmothers and my disputatious grandfather for being with me all the time and for their sense of responsibility.

I am also deeply indebted to my wonderful girlfriend for her love, sense of good things and spontaneous emotionality.

Dortmund, February 2007

Jaan Unger

Curriculum Vitae

Personal

Name: Jaan Alexander Unger
Date of Birth: 18 November 1975
Place of Birth: Stuttgart, Germany
Nationality: German

Education and Experience

1982-1986 Primary school, Stuttgart, Germany
1986-1987 Secondary school, Böblingen, Germany
1987-1996 Secondary school, Bochum, Germany
1996-2002 Mechanical Engineering, University of Bochum, Germany
1999-2000 Mechanical Engineering, University of Sheffield, UK
2002-2003 Research fellow at the Research Centre Jülich, Germany
since 2003 Ph.D. researcher, Chair of Mechanics, University of Dortmund, Germany